UNIVERSITY OF SOUTHAMPTON

# PERTURBATIONS OF ROTATING COMPACT OBJECTS

By
Rhiannon Lowri Williams

A thesis submitted for the degree of
Doctor of Philosophy

School of Mathematics,
University of Southampton,
Southampton, SO17 1BJ
United Kingdom.

August 2004

UNIVERSITY OF SOUTHAMPTON

## ABSTRACT

FACULTY OF ENGINEERING, SCIENCE AND MATHEMATICS

MATHEMATICS

Doctor of Philosophy

# PERTURBATIONS OF ROTATING COMPACT OBJECTS

by Rhiannon Lowri Williams

I present numerical studies of perturbed black holes and neutron stars. The behaviour of such compact objects is of particular interest now because the gravitational wave signals which they emit may be the first to be detected by the new generation of interferometric detectors.

A single perturbed black hole is well approximated using the linearized Einstein equations and the problem is reduced to solving a simple wave equation with a potential. I show how such a wave equation may be evolved numerically on Cauchy or characteristic hypersurfaces. I present a new numerical code for evolving scalar wave perturbations in Kerr spacetime as a characteristic (null-timelike) initial value problem. This code suffers from an instability but this problem can be pushed to very late times by increasing the grid resolution. The code shows second order convergence up until the time that the instability takes over. Previous numerical studies of perturbations in Kerr spacetime [2] were carried out using a Cauchy evolution code. I use this code to contribute to a recent discussion over the late-time behaviour of perturbations with initial form $m = 0, l = 4$, finding the expected fall-off of $t^{-3}$. I also use this code to lend support to the superradiance resonance cavity interpretation of Glampedakis and Andersson [52] to explain the long-lived quasinormal modes of Kerr spacetime. I have adapted the Cauchy code to use co-ordinates $(r_*, \theta_*)$ more suitable for a characteristic evolution and this code gives the expected results, comparable with the original version. I have also developed a code to evolve scalar field perturbations in Kerr spacetime in double-null coordinates but this is not stable. The cosmological constant plays an important role in cosmology and particle physics and will also effect the asymptotic geometry of black hole spacetimes. I investigate the effect of a cosmological constant on the late-time behaviour of a perturbed scalar field in Kerr-de Sitter spacetime and present some new results which reveal apparently undamped oscillations in some cases. I also investigate superradiance in the presence of a cosmological constant. The results show superradiance in the expected frequency range but the superradiance seems to extend

beyond the lower frequency limit predicted by Khanal [70] at large $\Lambda$. Evolutions of neutron star spacetimes are more complicated than the corresponding problem for black holes due to the presence of matter. Not only must we consider the response of the exterior spacetime but also the behaviour of the material that makes up the star. There are many more factors which need to be taken into account. I present work done in collaboration with Watts and Andersson [3] to study the effect of differential rotation on a simple system, a rotating spherical shell. For this I have developed a numerical time evolution code which confirms the predictions of Watts *et al.* [4] for a new class of oscillations and a new instability.

# Certificate of Originality

I hereby declare that this submission is my own work and that, to the best of my knowledge and belief, it contains no material previously published or written by another person nor material which to a substantial extent has been accepted for the award of any other degree or diploma of a university or other institute of higher learning, except where due acknowledgement is made in the text.

I also declare that the intellectual content of this thesis is the product of my own work, even though I may have received assistance from others on style, presentation and language expression.

Rhiannon Lowri Williams

# Acknowledgements

Thank you to the Faculty of Mathematical Studies, University of Southampton for financial support. Thank you to Nils Andersson for guiding my research and helping me out when I got stuck and to Ray d'Inverno. Thank you to Uli Sperhake for teaching me the necessary numerical and computational skills. Thanks to all the GR group, especially to Paul and Ian for computer support and to Anna and Kirsty for giving me a place to stay during the final stages. Thanks to Philipos Papadopoulos for pointing me in the right direction to find suitable characteristic coordinates for Kerr spacetime. Thanks to James Vickers for mathematical help. Thank you to my father for financial and moral support. Thanks to my fiancée for encouraging me to finish. Thanks to all my friends for tolerating my reclusive stages while finishing.

# Contents

# List of Figures

# Chapter 1

# Introduction.

A scientific theory must provide some explanation for our sensory experiences. It gains further credibility by making predictions which can be verified by experience either directly through our senses or via some reliable instrument. In these respects general relativity has been a very successful theory. It successfully agrees with the predictions of classical Newtonian physics in what has come to be known as the Newtonian limit, where speeds are small compared to the speed of light, and gravity is weak. It gives the correct description for the perihelion shift of Mercury, which could not be explained by classical mechanics and was called 'peculiar'. In 1916 Einstein proposed an experiment to test his theory's new prediction of the bending of light around the Sun, and in 1919 such an experiment was carried out during a total Solar eclipse verifying this prediction. One prediction of general relativity yet to be verified, however, is the existence of gravitational radiation. Not only are scientists interested in detecting gravitational waves as a test of general relativity, but gravitational radiation could also become a very useful tool in its own right, allowing us to probe parts of the universe which are inaccessible via the electromagnetic spectrum.

An order of magnitude calculation shows that the amplitude of gravitational waves arriving at earth from even the most powerful known sources will be extremely small. In fact it will probably be smaller than the experimental noise, making it very difficult to detect. In order to find such a small signal, the form of the signal must be known in advance, and a technique called *matched filtering* used to search the output for this signal. Coalescing compact binaries possess a characteristic gravitational wave signal which depends on the binary object's masses and their separation. A recent review concludes that inspiralling binary black holes are likely to be detected first by the initial ground based interferometers [1], yet the prediction of the full gravitational wave signal is proving to be a great challenge.

In general relativity, information on the structure of spacetime and it's interaction with matter is encoded within differential equations which must be solved in order to get a clear understanding of the physical situation. Unfortunately, Einstein's equations have, to date, only been solved analytically in a limited number of special highly idealized cases. The problem is that these equations are nonlinear and there is much yet to be understood in the realm of nonlinearity. In the case of binary black holes, during the early stages of inspiral it is possible to use post-Newtonian approximation techniques whereby Einstein's equations become reduced and simplified. During merger however, these approximations are no longer valid and the full set of Einstein's equations must be solved by numerical methods (numerical relativity). At later times, the system can be modelled by a single slightly distorted black hole and we can use a linearized approximation to Einstein's equations and perturbation methods. This last stage is the focus of this thesis.

Using perturbation methods, the equations governing the behaviour of the final black hole are relatively simple and can be analysed in the frequency domain, or evolved numerically to discover how the signal varies with time. Numerical evolutions for nonrotating black holes carried out over the past 30 years have provided a great deal of insight. Similar evolutions of perturbed rotating black holes, on the other hand, have only recently been carried out [2]. An approach which has proved to be extremely convenient and beneficial for numerical study of radiation problems in general is characteristic evolution, in which the equations are evolved on characteristic hypersurfaces. In the case of a single perturbed black hole, this approach enables the evolution of the entire exterior spacetime through compactification and avoids the boundary problems which plague time evolutions. In this thesis I therefore seek to apply this method to the study of rotating black holes.

Recent advances in cosmology indicate that the universe in which we live possesses a positive cosmological constant. This will have a dramatic effect on the asymptotic structure of a black hole spacetime. Numerical evolutions for nonrotating black holes in the presence of a cosmological constant have shown that some interesting new features arise for some types of initial data. In this thesis I investigate the effect of a cosmological constant on the late-time behaviour of perturbed rotating black holes.

Another promising source of detectable gravitational wave signals is neutron stars. The simulation of a perturbed neutron star is more complicated than the corresponding case for black holes due to the presence of matter in the equations. Whereas a general black hole can be completely described using only three parameters, many more features are required to fully describe a neutron star, and the full structure is still unknown. A well known phenomenon observed in many stars, including the Sun, is differential rotation. To model a realistic neutron star with differential rotation would be an enormous and difficult task. In this thesis I present work carried out in collaboration with A.L. Watts and N. Andersson [3] to investigate the effect of differential rotation on a perturbed spherical shell in Newtonian gravity. We expect that some of the features we observe in this toy problem will carry over to the case of a real neutron star.

This thesis begins in Chapter 2 with an introduction to gravitational waves, black holes and neutron stars. There I present the motivation for the thesis. It is not intended to be a comprehensive review, rather I give an overview of the major developments in these fields which relate to the problems I consider in the later chapters.

In Chapter 3 I present the mathematical background to this thesis. I show how the initial value problem can be formulated in three different ways, the Cauchy, double-null, and null-time like formulations. To demonstrate this I use the simple example of the one-dimensional wave equation in flat space.

Chapter 4 introduces the numerical techniques I use in this thesis for numerical integration and evolution.

In the next three chapters I use the mathematical and numerical background of the previous chapters in some toy problems which serve as progressive examples which will be extended further in later chapters. In Chapter 5 I evolve the one-dimensional wave equation in flat space. In Chapter 6, I extend the problem to evolve the Regge-Wheeler equation which governs perturbations on a Schwarzschild background. This is a one-dimensional wave equation with a potential. In Chapter 7 I extend the problem further by working in two-dimensions to evolve the axisymmetric wave equation in flat space. In all these toy problems, the numerical evolutions are carried out using both Cauchy and characteristic formulations and the results are tested by comparison with known analytic solutions.

The final three chapters are the main work of this thesis. In Chapter 8 I apply my experience from the toy problems to study rotating black holes. I write the scalar wave equation in Kerr spacetime in null-timelike coordinates and develop a numerical code to evolve this equation. I also use an older time evolution code to contribute to the recent debate over the late-time behaviour of a scalar field with an initial perturbation of the form $m = 0$, $l = 4$. I present some results which lend support to the recent interpretation of the late-time long-lived quasinormal modes in extreme and near extreme Kerr black holes as products of a superradiant resonance cavity directly outside the black hole.

In Chapter 9 I evolve the scalar wave equation for a rotating black hole in the presence of a positive cosmological constant and show some interesting new features which emerge at late-times. I also give evidence to support some previous superradiance calculations.

In Chapter 10 I evolve perturbations in a thin spherical shell with differential rotation. The results confirm the semi-analytic predictions by A.L. Watts et al [4], including a new kind of instability.

Finally, in Chapter 11 I discuss the main results of this thesis and describe some possibilities for future research that have been generated by this work.

# Chapter 2

# Gravitational Waves, Black Holes and Neutron Stars

## 2.1 Gravitational Waves

According to standard Newtonian gravitation theory, the gravitational interaction between two separated objects is instantaneous, i.e. there is *action at a distance*. According to the principles of special relativity however, the speed of light is the limiting speed for all interactions. General relativity incorporates this limiting speed for gravitational interaction so that changes in the shape of a particular object will produce changes in the gravitational field which propagate outward at the speed of light. In this way the gravitational effect on a second object located at some distance from the first will not be felt instantaneously. Distortions in the gravitational field which travel at the speed of light are called gravitational waves.

Einstein showed in 1916 that the equations of general relativity admit gravitational waves as solutions but in the late 1940's doubts arose as to whether or not such waves are *real*, i.e. whether or not they carry energy. That gravitational waves carry energy was finally established by Bondi in 1957 using a clever thought experiment first presented by Richard Feynman [5]. Feynman described beads moving up and down against a stick under the influence of gravitational radiation and heating the system by friction. The heating shows a transfer of energy which must be carried by the gravitational waves. In 1960 Joseph Weber began the search for these waves.

Since the 1960s there have been many technological and theoretical developments. The experimental apparatus has become much more sensitive and accurate and we have much more information about what sources to look for, and we have also gained indirect evidence for the existence of gravitational waves. As yet (2004) however, the quest to detect gravitational waves has not been successful, although with many new detectors now coming on line there is a good chance that a detection event will occur in the next few years.

### 2.1.1 *Weak Gravitational Fields in Flat Spacetime*

The absence of gravity leaves spacetime flat, so we could consider a weak gravitational field to be one in which spacetime is nearly flat, i.e. we consider nearly Lorenzian coordinates in which the metric has components

$$g_{\mu\nu} = \eta_{\mu\nu} + h_{\mu\nu} \; , \; |h_{\mu\nu}| \ll 1 \tag{2.1}$$

where $\eta_{\mu\nu}$ is the flat space metric and $h_{\mu\nu}$ is a small perturbation. Under a background Lorenz transformation, $h_{\mu\nu}$ transforms as a tensor, so we can imagine our weak gravitational field as a tensor $h_{\mu\nu}$ on a flat background. The *Lorenz* (de Donder) gauge is given by

$$\bar{h}^{\mu\nu}_{\;\;,\nu} = 0 \tag{2.2}$$

$$\bar{h}^{\mu\nu} = h^{\mu\nu} - \frac{1}{2}\eta^{\mu\nu} h \tag{2.3}$$

and $h$ is the trace, $h^{\mu}_{\mu}$. In this gauge the Einstein equations reduce, to linear order in $h$, to

$$\Box \bar{h}^{\mu\nu} = -16\pi T^{\mu\nu} \tag{2.4}$$

where $T^{\mu\nu}$ is the stress-energy tensor, describing any matter present, and $\Box = \eta^{\mu\nu}\partial_\mu\partial_\nu$ is the D'Alembertian operator. These are called the linearized Einstein equations. In vacuum we have

$$\Box \bar{h}^{\mu\nu} = 0 \tag{2.5}$$

which is the familiar four dimensional wave equation. Any solution to this equation is a superposition of plane wave solutions. One consequence of this is that gravitational effects propagate at the speed of light.

### 2.1.2 *Detection*

Electromagnetic waves can be detected by their effect on a single test particle - when the wave hits the particle it causes an acceleration transverse to the waves propagation direction and proportional to $e/m$ (charge to mass ratio of particle). When a gravitational wave hits a free particle it also imparts transverse acceleration, but the "gravitational charge" (its response to gravitational force) is equal to it's inertial mass, $m$. This is the equivalence principle which means that all particles

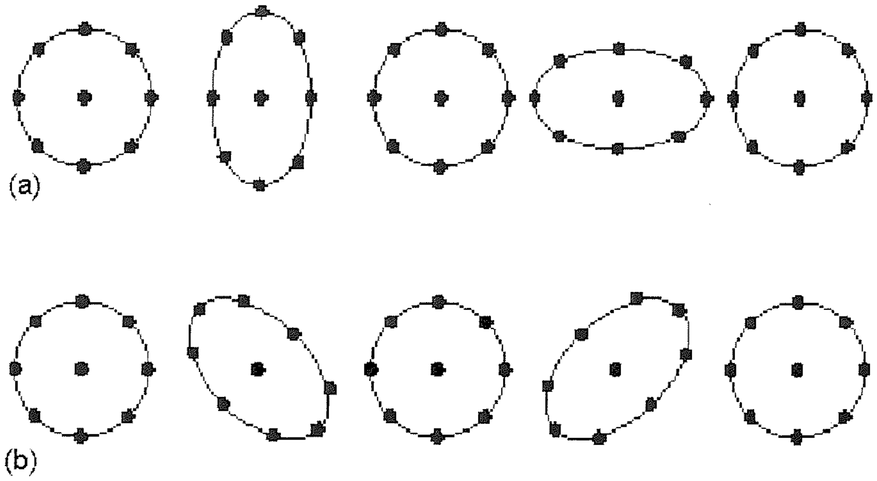

Figure 2.1: A ring of particles being stretched and squeezed by a gravitational wave passing perpendicular to the plane of the page. (a). The "+" polarization. (b). The"×" polarization.

have the same gravitational "$e/m$", i.e. all particles at the same location experience the same transverse acceleration, so all local reference frames also undergo the same acceleration and hence the acceleration is locally undetectable. However, the acceleration is different at different locations and so we can use two particles separated by a distance $L$ and measure the acceleration and hence the change in separation, $\delta L$. A measure of the amplitude of the gravitational waves is given by the dimensionless strain, $h = \delta L/L$. The stretching and squeezing effect of gravitational waves is usually illustrated by considering a ring of particles. Gravitational waves possess two polarization states, i.e. the gravitational field has two radiation degrees of freedom. The corresponding modes produced in the ring of particles are shown in Fig. 2.1.

There are two types of detectors currently being used in the search for gravitational waves.

- In bar detectors the gravitational forces stress the material of a solid bar and cause it to oscillate. The oscillations can be detected if the frequency is near the resonant frequency of the bar, typically about 1kHz.
- Laser interferometric detectors are giant L-shaped instruments. Laser beams are bounced along the two arms, being reflected at the ends by mirrors which are suspended by wires. The reflected beams are recombined and their interference pattern is monitored by a photodetector. A passing gravitational wave displaces the mirrors thus causing a detectable shift in the interference pattern. These detectors operate over a broad frequency range.

Detectors currently under construction are expected to measure strains down to $h \sim 10^{-21}$, but this is still much bigger than any known Earth-based mechanism can generate. We must look further afield to violent astrophysical events such as supernova explosions, coalescing compact binaries (neutron stars or black holes), individual black holes or neutron stars, or the early universe.

## 2.2 Black Holes

In 1783 a British natural philosopher named John Mitchell reasoned that if a star is dense enough, the initial speed required for a particle launched from the surface to escape (the escape velocity) could reach or exceed the speed of light. He further reasoned that since, according to the corpuscular theory of light which was prevalent at that time, light was also a particle, it too may be affected by gravity in the same way. There was nothing in the physics of the day which prevented the existence of such a dense star and Mitchell therefore concluded that there may exist *dark stars* from which no light could escape. Later however, with the demise of corpuscular theory and the rise of the wave theory of light, the reasoning of the above argument lost it's basis.

Over a century later, in 1915, when Einstein presented his theory of general relativity [6], a new version of dark stars appeared. Almost immediately after the publication of Einstein's original paper, Karl Schwarzschild used Einstein's field equations to calculate the curvature of spacetime outside any spherical, nonspinning star, now known as Schwarzschild geometry [7]. One of the consequences of his calculations was that, for a star of fixed mass, there is a critical size at and below which no light can escape beyond the critical radius, the *Schwarzschild singularity.*

The physical relevance of this conclusion was debated for the next 50 years. In the mean-time however several developments suggested that these unusual objects could exist in the universe. In 1931 Chandrasekhar showed that white dwarfs, dense stars held up by degeneracy pressure, had an upper mass limit of $1.4M_\odot$ [8]. The discovery of the neutron in 1932 led to the idea of Baade and Zwicky [9] that there could be stars made entirely of these particles, which Oppenheimer and Volkoff [10] showed in 1938 would also have an upper mass limit. In 1939 Oppenheimer and Snyder [11] showed that, in the reference frame of the stellar surface, the gravitational collapse of a highly idealized spherical, pressureless, nonspinning, nonradiating star continues past the Schwarzschild singularity. The high level of idealization left plenty of room for doubt, but by the late fifties physicists had learned many new tools during their war-time hydrogen bomb research and by the early sixties Colgate, White and May [12] were able to relax some of the idealizations in their computer simulations. These simulations retained only two idealizations, the star must be spherical and nonrotating. In 1958 Finkelstein [13] discovered a new reference frame in which to describe Schwarzschild geometry and which reconciled some of the main difficulties in understanding the results of gravitational collapse, showing the Schwarzschild singularity not to be a real singularity at all but merely a coordinate singularity which could be removed by a transformation of coordinates. The Schwarzschild singularity became known as the *horizon* and the central object created by the stellar implosion was given the name *black hole*.

The decade between the mid-sixties and mid-seventies has become famed as the golden age of black hole research [14]. During this time great advancements were made by many researchers in understanding the nature and properties of black holes. Much of this advancement was based on perturbation methods outlined in a landmark paper published in 1957 by Regge and Wheeler [15] in which they derive their equation describing a slightly perturbed Schwarzschild black hole. Using this equation they showed that Schwarzschild spacetime is stable, as confirmed by Vishveshwara [16]. Black holes could now also have electric charge, as described by the Reissner Nordstrom solution of 1918 [17] (the physical meaning of the solution was uncovered in 1960 by Graves and Brill [18]). Kerr [19] calculated a solution to Einstein's equations which describes the spacetime curvature outside any spinning black hole. Carter [20] calculated the properties of the Kerr black hole and showed how the spinning motion can twist spacetime itself. In 1972 Teukolsky [21] presented his equation describing perturbed Kerr black holes. More exotic processes were theorized, such as black hole accretion disks [22] and the jets produced by the Blandford-Znajek process [23], and black holes were used to explain observations of quasars and radio galaxies. In 1970 Hawking and Penrose [24] redefined the black hole horizon. Zel'dovich [25] used quantum theory to argue that a spinning black hole radiates gravitational energy and Hawking showed that in this way black holes evaporate [26].

The observational search for these invisible objects began in the early sixties. Zel'dovich and Novikov [27] proposed that stellar matter falling onto a black hole could be heated to such a high temperature that it emits X-rays. If a binary with one optically bright source and one X-ray bright source could be detected, and the X-ray source was sufficiently massive, then this would be a good black hole candidate. Since X-rays cannot penetrate the Earth's atmosphere, detection was difficult at first but the first X-ray satellite UHURU, launched in 1970, detected a good candidate - Cygnus X1 [28]. Since then many more candidates have been detected by this method and others. There is now strong observational evidence that most galaxies have a super-massive black hole at their center [29].

## 2.3 Neutron Stars

Baade and Zwicky proposed the idea of neutron stars in 1934 [9], and they also suggested that such stars could be formed in supernovae. In 1939 Oppenheimer and Volkov developed the first neutron star model. They assumed that it was made of a high density ideal gas of neutrons. Then, for over 20 years, little attention was given to neutron stars until the discovery of a cosmic, non-solar X-ray source by Giacconi et al in 1962 [30]. Some researchers suggested that the source of the X-rays could be a young, warm neutron star.

The discovery of quasi stellar objects in 1963 [31] also brought more attention to neutron stars as it was thought that the high redshifts may be due to gravitational redshift at the surface of such a dense object. By 1965 the quasar redshifts were shown to be too high to be accounted for by gravitational effects from a neutron star [32], but by then the neutron star concept had caught on and some theoretical physicists had begun to calculate their properties, although it still remained an abstract concept and was not taken too seriously by much of the scientific community [33]. After the discovery of pulsars [34] in 1967 however, Gold [35] proposed that they were rotating neutron stars and neutron stars became firmly established in the world of astronomy. The Crab and Vela pulsars were discovered situated in supernova remnants [36] and this gave evidence for the earlier suggestion that neutron stars may be formed in supernova explosions. In 1971 the UHURU satellite discovered X-ray pulsars [37] which are believed to be neutron stars accreting matter from a normal binary companion star.

The usual approach to modelling neutron stars is to consider an ideal fluid with some particular equation of state. The true equation of state for the interior of compact stars is unknown but many different possible equations of state have been proposed which satisfy the current observational constraints. These various equations of state can lead to substantial differences in the bulk properties such as maximum mass, radius and rotation rate, so there is still a lot that is unknown about the structure and evolution of neutron stars. Some of these issues may be resolved through gravitational wave astronomy.

## 2.4 Coalescing Compact Binaries

Coalescing compact binaries are among the most promising sources of gravitational radiation for future detection. This coalescence is not only one of the most violent events in the universe, giving off vast amounts of energy in the form of gravitational waves, but the spectrum of those gravitational waves is also expected to have a specific characteristic form. Such sources are extremely far away and therefore the gravitational radiation we receive from them is expected to be of very low amplitude, and therefore buried in detector noise. The chances for detection could be significantly increased, however, if we can predict the signals spectrum in advance. We can then use a technique called matched filtering, whereby templates of predicted signals are matched against the detector output.

A typical signal from coalescing compact binaries consists of three main parts. The first part represents the inspiral phase in which the two objects are well separated. The frequency and amplitude of this oscillating signal, called a *chirp* signal, increase with time as the two objects spiral inwards. The second part represents the merger. It is here that non-linear relativistic effects play an important role and the form of the signal is expected to be more complex. In the later stages of the coalescence, following merger, we are left with a single perturbed black hole or neutron star. This stage is called the ring down. For a black hole the ring down consists of damped oscillations of fixed frequency, called *quasi-normal modes*, and a late time fall off, called the *tail*. If the final object is a neutron star, the third stage will be more complicated due to various types of possible oscillations in the matter itself.

In the inspiral phase, relativistic effects are expected to be less important as the two black holes are well separated and do not become distorted due to interaction. Here, an analytic approximation technique called *post-Newtonian approximation* is used to predict the form of the gravitational radiation emitted. There is already indirect evidence for the emission of gravitational radiation in the discovery by Hulse and Taylor [39] of the binary pulsar PSR 1913+16. Observations show that the orbital period of this system is steadily decreasing, i.e the system is losing energy, and this decrease is in excellent agreement [40] with the value predicted using Einsein's quadrupole formula. The quadrupole formula shows how the total power emitted in gravitational waves by an isolated Newtonian source depends quadratically on the variations of the quadrupole moment of the source. The energy loss of a binary with circular orbit of radius $a$ and total mass $M$ is given by the formula [41]:

$$\frac{dE}{dt} = -\frac{32}{5}\frac{\mu^2 M^3}{a^5} \tag{2.6}$$

where $\mu = m_1 m_2 / M$ is the reduced mass and $m_1$ and $m_2$ are the individual masses of the binary components. The rate at which gravitational radiation is emitted increases as the binaries inspiral, i.e. as $a$ decreases, the frequency and amplitude of the gravitational waves increase, producing the characteristic *chirp* waveform.

In the merger phase, when the two objects become too close for post-Newtonian techniques to realistically describe the evolution, the full Einstein equations must be solved. It is not possible to do this analytically, therefore numerical approximation techniques are used to simulate the merger. This has proved to be a very difficult task. See [42] for a review of numerical relativity.

During the last stage when we have a single perturbed black hole, the nonlinear effects of full general relativity are expected to be quite small and a perturbation approach can be used. In this approach the evolution of a perturbing field is calculated against a fixed background spacetime using a linearized version of Einstein's equations. This approach can also be used during the late part of the merger phase when the two objects are close enough to be approximated as one object in the *close limit* approximation [43]. The LAZARUS [44] project aims to follow coalescing black holes through all three phases by combining post-Newtonian approximation, numerical relativity and perturbation techniques in one code.

The form of the signal during ring down, obtained via a pertubation approach, is the main focus of this thesis. I therefore devote the rest of this section to a review of the major developments in this field and set the context for this current work.

## 2.5 Black Hole Perturbations

When Regge and Wheeler derived their equation governing black hole perturbations in 1957, their motivation was to discover whether or not black holes are stable to small perturbations. They found that the reaction of the black hole was governed by a fairly simple equation - a wave equation with a potential. Some time later, Vishveshwara used numerical methods to investigate scattering of radiation in Schwarzschild spacetime. He sent Gaussian wave packets moving towards the black hole and studied the scattered waves. He discovered that when the initial Gaussian was wide there was nothing particularly interesting to be seen in the scattered pulse but for narrower initial data he discovered damped oscillations. Throughout the seventies, others found similar results in studying this problem and also in studying infalling test particles [45] and slightly nonspherical gravitational collapse [46]. They observed

- an initial waveburst
- exponentially damped ringing
- a power law fall off at late times [47]

Whereas the initial waveburst depended upon the form of perturbing field, it was observed that the frequency and damping of the ringing and the late time power law behaviour were characteristics of the black hole itself. The black hole oscillations are now known as *quasinormal modes* and the late time fall off is called the *tail*.

Today we are able to calculate quasinormal mode frequencies by working in the frequency domain (see e.g. [48], [49]) and it can be shown in this way that the quasinormal modes correspond to poles in the complex frequency plane and that the late time tail corresponds to a branch cut along the negative imaginary axis. In physical terms, the quasinormal modes are analogous to the resonances found in quantum scattering, and the tail has been shown to arise from back-scattering off the long-range gravitational field. This field has been well researched, yet recent surprising results [51], [52] and questions [50] concerning the late time behaviour of spinning black holes show that there is still work to be done.

## 2.6 Neutron Star Perturbations

Modelling perturbations in a neutron star spacetime is more complicated than the corresponding problem for black holes because we must consider oscillations in the neutron star matter itself as well as the reaction of the exterior spacetime. We must therefore include the equations of hydrodynamics. A more realistic model will also include the effects of magnetic fields, superfluidity, Ekman layers (i.e. the presence of a crust), and exotic particles, but there is much work still to be done before we have a good understanding of these effects.

Most stars are expected to undergo some kind of oscillation during their lifetime and these oscillations are accompanied by the emission of gravitational waves. Neutron star oscillations could generate detectable gravitational radiation which could reveal information about the interior of the neutron star by comparison with numerical models.

There are several types of oscillation modes which can be classified according to the physical mechanism or the characteristics of oscillation. A description of the various modes may be found in a review by Kokkotas and Schmidt [53] and at the SISSA website [54].

Achieving a fully relativistic 3D numerical hydrodynamic model of neutron star oscillations has proved to be a very difficult task. This is a non-linear problem and requires highly advanced computational techniques to handle shocks. In general however, the oscillations are expected to be much smaller than the radius of the neutron star itself and can therefore be approximated by linear perturbations. Even this task is not straightforward, especially in the case of rotating neutron stars. One simplification is the Cowling approximation [55] in which perturbations in the gravitational field are neglected and the oscillations are described only by perturbations in the fluid variables. The calculations of stellar perturbations presented in this thesis are in the Newtonian limit and our model is highly simplified but we do include the effects of differential rotation. We expect that many of the results will carry over into the relativistic regime.

## 2.7 Rotating Black Holes

Kerr black holes are the universal limit in the gravitational collapse of any rotating body and, since most stars rotate, Kerr black holes are expected to be more physically relevant than Schwarzschild black holes. An equation analogous to the Regge-Wheeler equation was obtained by Teukolsky [21] using the Newman-Penrose formalism [56]. The Teukolsky equation describes the evolution of scalar, electromagnetic and gravitational perturbations in Kerr spacetime. It is also possible, by studying this equation in the frequency domain and using analytic approximations, to calculate the quasinormal mode frequencies, damping, and tail. Predictions based on such analysis show that there should be some difference between the late time tails of Schwarzschild and Kerr black holes, in particular that there should exist long lived quasinormal modes for Kerr spacetime [57].

### *2.7.1 Superradiance*

When waves of frequency $\omega$ impinge on a black hole with rotational frequency $\Omega$ and these waves satisfy the condition

$$\omega - m\Omega < 0 \tag{2.7}$$

where $m$ is the azimuthal order (or quantum number) and the azimuthal dependence is $e^{im\phi}$, then the scattered waves will be amplified. A distant observer will see waves coming out of the horizon, even though a local observer sees them going into the black hole. This effect, called superradiance, was first predicted by Zel'dovich in 1971 [25] and Misner [58] independently made a similar prediction shortly thereafter which he supported with analytic calculations. Superradiance is the wave analogue of the Penrose process and the energy coming out of the black hole is compensated for by a corresponding decrease in the hole's angular momentum. The amplification factor for scattered scalar waves was calculated in 1972 by Press and Teukolsky [59] to be 0.3% and the amplification of electromagnetic and gravitational waves were given in a later paper [60] by the same authors as 4.4% and 138% respectively. The scalar wave superradiance was confirmed numerically by Andersson et al. [61] using a Cauchy time evolution of the scalar wave equation in Kerr spacetime.

Andersson and Glampedakis [51] have argued that whereas the individual long lived quasi-normal modes of Kerr spacetime will not be significantly excited, a large number of them can combine at late times to completely dominate the late time behaviour. They support their analytic calculations, which involve many simplifying approximations, with results from the Cauchy evolution code of [2] but they warn that the results of the numerical code may also not be trustworthy. They offer an interpretation of their results based on a *superradiant resonance cavity* just outside the horizon whereby, for frequencies close to the upper limit of the superradiant regime, there will be a peak in the effective potential (frequency dependent) just outside the black hole. Waves which "emerge from the horizon" according to a distant observer can become trapped near the horizon by the potential peak and experience a kind of parametric amplification until they can leak out through the horizon to infinity.

### *2.7.2 A Characteristic Approach*

The numerical work of Glampedakis and Andersson was carried out using a time evolution of the Teukolsky equation [2], but there are some late time convergence problems with this code. We therefore seek to improve the numerical results via a characteristic approach in which the solution is evolved on null hypersurfaces as opposed to space-like hypersurfaces. Using such an approach, it is possible to compactify the radial coordinate and thus include both the horizon and future null infinity in the numerical simulation. This is an advantage because it avoids the problems associated with artificial boundary conditions and also allows us to more accurately compare results with analytic calculations which are obtained using asymptotic approximations.

The characteristic approach has been successful for evolving Schwarzschild perturbations [62] where it has become in many ways the preferred method. It has also shown it's usefulness in fully relativistic simulations, using the Bondi-Sachs formulation. See [63] for examples of this. In numerical relativity a combination of both Cauchy and characteristic evolutions has also proved to be appropriate for some problems [64]. The combination of Cauchy and perturbative evolution has also been succesfully applied [65]. In Chapter 8 of this thesis I describe the development of a numerical code to evolve scalar perturbations in Kerr spacetime as a characteristic initial value problem.

### *2.7.3 Cosmological Black Holes*

When Einstein noticed that his equations predicted a non-static universe he was dissatisfied with this conclusion and introduced the cosmological constant [66]. An initially static universe would tend to collapse under the force of gravity but the cosmological constant balanced this force in order to make the universe static. This trick does not really work however because such a static universe is unstable and therefore would tend to contract or expand. Later, Edwin Hubble's observations indicated that the universe is actually expanding [67], therefore Einstein rejected the cosmological constant as his "biggest blunder". Today however, the cosmological constant continues to play an important role, not only in cosmology but also in particle physics where it is interpreted as a measure of the vacuum energy density. Inflation theory predicts the presence of a cosmological constant and many of the Grand Unified Theories predict an extremely large value for it. Observations suggest that the real value is very small. The big problem of the difference between the value predicted by particle physics and the observational data is yet to be resolved. The present theories can give the observed small value for the cosmological constant only with extremely precise fine tuning, which presents another problem in itself.

Recent observational results from supernova studies suggest that the expansion of the universe is accelerating [68] and this has helped to re-instate the cosmological constant as an important consideration in the current cosmological picture. The most general metric satisfying the cosmological principles of isotropy and homogeneity is the Robertson-Walker metric. In a flat universe with positive cosmological constant this metric reduces to the de-Sitter metric. Although the magnitude of the cosmological constant is observed to be very small in today's universe, it will influence black hole geometries which must then be taken as asymptotically de-Sitter.

Rotating black holes in asymptotically de Sitter spacetime are described by the Kerr-de Sitter metric. Khanal [69] has presented a master equation, similar to that of Teukolsky, for gravitational, electromagnetic and Dirac field perturbations in Kerr-de Sitter spacetime. He has shown that this equation reduces to the Teukolsky equation in the limit $\Lambda \rightarrow 0$ and the Schwarzschild-de Sitter perturbation equations in the limit $a \rightarrow 0$. He has also shown that superradiance can occur in Kerr-de Sitter spacetime [70].

Numerical studies of scalar field perturbations in Schwarzschild-de Sitter spacetime have uncovered interesting and surprising late-time behaviour [71]. Since the late time behaviour of the field is generally considered to be dependent upon the asymptotic structure of the spacetime only we should expect similar behaviour in for Kerr-de Sitter black holes. In Chapter 9 I present a new numerical code for the time evolution of scalar field perturbations in Kerr-de Sitter spacetime. As far as I am aware, this is the first time that such an evolution has been carried out in Kerr-de Sitter spacetime. I present interesting new features in the late-time behaviour and obtain results in the Schwarzschild-de Sitter limit similar to those found in previous studies. I test the conditions for superradiance derived by Khanal [69].

## 2.8 Rotating Neutron Stars

The effect of rotation on a star is to increase its equatorial radius and also to increase the mass that can be sustained for a given central energy density. According to Stergioulas [73], the mass of the maximum mass rotational model is about $15-20\%$ higher than in the maximum mass nonrotational model for typical realistic equations of state. The corresponding increase in radius is $30-40\%$.

In nonrotating stars the spacetime outside the star itself is described by the Schwarzschild metric and the perturbations of that spacetime can be described by the Regge-Wheeler equation for odd perturbations or the Zerilli equation for even perturbations. For rotating stars, however, no decoupled equation corresponding to the one discovered by Teukolsky has be found because the metric of a rotating neutron star and a Kerr black hole are of different Petrov types (see section 8.2.3) and therefore the analysis leading to the Teukolsky equation cannot be applied in the case of a neutron star.

Some oscillations may become unstable in rotating stars due to the emission of gravitational waves. This CFS instability (named after Chandrasekhar, Friedman and Schutz [74] who discovered it) causes the stellar oscillations to increase, which leads to greater emission of gravitational waves and even greater oscillations etc. Such an instability could be a strong source of gravitational waves.

In rotating stars a new type of mode appears which is degenerate at zero-frequency in the nonrotating case. These modes, called *inertial* modes in the Newtonian limit, have received a lot of attention in the past few years due to the fact that they are generically unstable to the emission of gravitational waves by the CFS instability, as demonstrated by Andersson [75].

Even in the Newtonian limit there are effects due to rotation which still require further investigation. One of these is the effect of differential rotation on the various oscillation modes. In Chapter 10 I present some new results in this regard from work carried out in collaboration with A.L Watts for a simplified model of a differentially rotating, axisymmetric spherical shell.

# Chapter 3

# The Initial Value Problem

If a theory permits a physically reasonable specification of initial data, and this initial data uniquely determines the future evolution of the system, then the theory possesses an initial value formulation. For the initial value formulation to be well posed the solution must depend continuously on the initial data without violating causality.

Spacetime may be foliated by a set of hypersurfaces and the properties of those hypersurfaces determine the nature of the initial value formulation. The most popular formulation is the Cauchy initial value problem in which spacetime is foliated by space-like hypersurfaces. The initial data consists of the solution and its first time derivative on the first hypersurface.

An alternative formulation is given by the characteristic initial value problem in which spacetime is foliated by lightlike hypersurfaces. In the double-null initial value problem, the initial data consists of the solution alone on initial advanced and retarded lightlike hypersurfaces. In the null-timelike initial value problem, the initial data consists of the solution on an initial null hypersurface and an initial timelike hypersurface.

## 3.1 Example: The One-Dimensional Wave Equation

The one-dimensional wave equation in $(t, x)$ coordinates is

$$\partial_{tt}\Psi - \partial_{xx}\Psi = 0 \tag{3.1}$$

where we work in relativistic units, $c = 1$, and $\Psi = \Psi(t, x)$. A general solution is given by the D'Alembert solution

$$\Psi = f(u) + g(v) \tag{3.2}$$

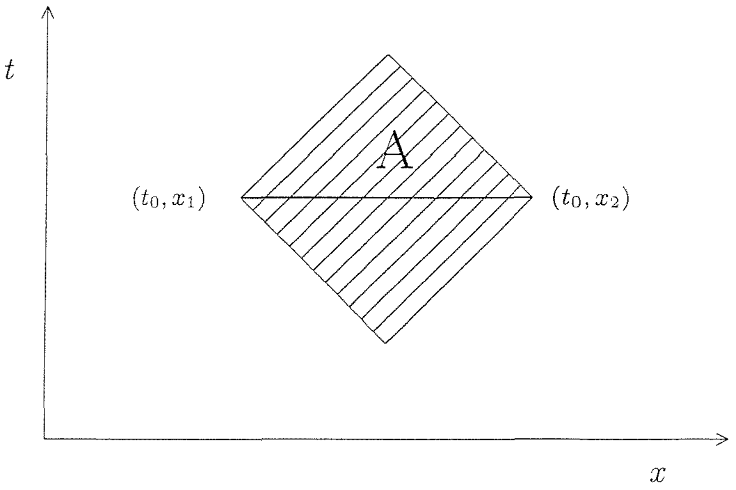

Figure 3.1: The Cauchy initial value problem. Initial data, consisting of $\Psi$ and its time derivative, is given on $t_0$, a surface of constant $t$. For initial data between $x_1$ and $x_2$, the solution may be calculated according to eq. (3.10) in the shaded area $A$.

where $u$ and $v$ are the null coordinates

$$u = t - x \tag{3.3}$$

$$v = t + x \tag{3.4}$$

and $f$ and $g$ are arbitrary functions.

As a simple illustrative exercise we will formulate the 1-d wave equation as three distinct initial value problems [76].

### *3.1.1 The Cauchy Initial Value Problem*

Using the wave eq. (3.1) we specify initial data on $t = 0$ between $x = x_1$ and $x = x_2$.

$$\Psi(x, 0) = F(x) = f(-x) + g(x) \tag{3.5}$$

$$\partial_t \Psi = G(x) = -\partial_x f(-x) + \partial_x g(x) \tag{3.6}$$

Integrating eq.(3.6) with respect to $x$ gives

$$-f(x) + g(x) = \int_{t-x}^{t+x} G(\bar{x}) d\bar{x} \tag{3.7}$$

adding/subtracting this equation to/from eq. (3.5) gives us equations for the functions $f$ and $g$ in terms of our initial data

$$2g(x) = F(x) + \int_{t-x}^{t+x} G(\bar{x}) d\bar{x} \tag{3.8}$$

$$2f(-x) = F(x) - \int_{t-x}^{t+x} G(\bar{x}) d\bar{x} \tag{3.9}$$

and we can then write the solution in terms of the initial data as

$$\Psi(x,t) = \frac{1}{2}[F(x-t) + F(x+t)] + \frac{1}{2} \int_{x-t}^{x+t} G(\bar{x}) d\bar{x} \tag{3.10}$$

which is valid in the region A of fig.(3.1). This solution is valid for an infinite string provided we have initial data for all $x$.

For a string which is tied at the origin, we can no longer use the above solution for points at $x < t$. This is due to a lack of initial data at $x < 0$. However we can calculate the solution by using the boundary condition, $\Psi(0,t) = 0$. We would like to know the solution at point $(x_p, t_p)$ on Fig. 3.2. According to d'Alembert's solution, eq.(3.2)

$$\Psi = f(-x_p + t_p) + g(x_p + t_p) \tag{3.11}$$

Initial data exists for $g(x_p + t_p)$ but not for $f(-x_p + t_p)$. We use the fact that the value of $f(-x+t)$ is constant along the line from $A$ at $(0, T)$ to our point at $(x_p, t_p)$, and at A we have

$$\Psi = f(T) + g(T) = 0 \tag{3.12}$$

as our boundary condition. The value of $g(x+t)$ is constant along the line connecting $A$ to the point $B$ at $(X, 0)$ and therefore $f(A) = -g(B)$. The coordinate $T$ is given by $T - 0 = t_p - x_p$ and the coordinate $X$ is thus given by $0 + X = T + 0 = t_p - x_p$. We can now write the solution as

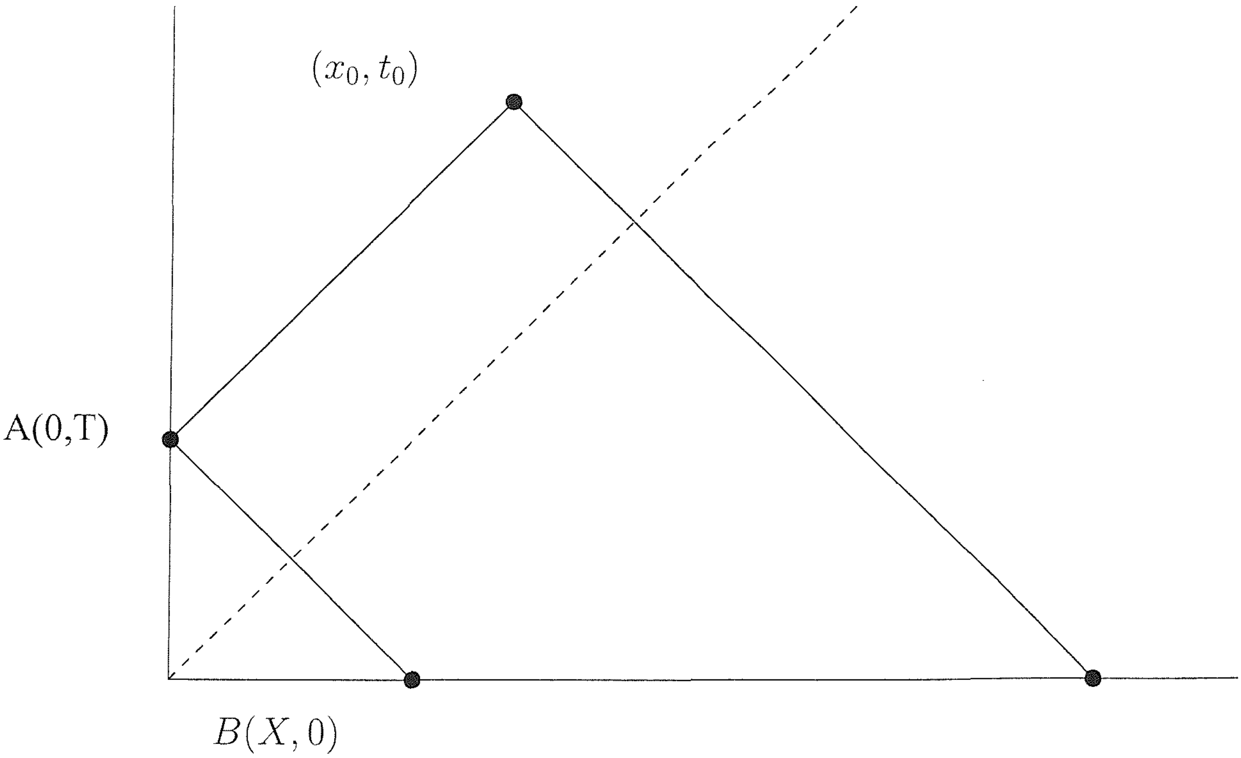

Figure 3.2: Cauchy initial value problem for semi-infinite initial data. Initial data exists for positive $x$ only. The solution at the point $(x_0, t_0)$ will depend on the boundary condition at $x = 0$. If there is some reflection at the boundary then the solution at $(x_0, t_0)$ will depend on the initial data at the point $B$. The solution according to eq. (3.13) is valid for all positive $x$ and $t$.

$$\begin{aligned}
\Psi(x,t) &= -g(t_p - x_p) + g(x_p + t_p) \\
&= \frac{1}{2}[F(x+t) - F(t-x)] + \frac{1}{2}\int\limits_0^{x+t} G(\bar{x})d\bar{x} - \frac{1}{2}\int\limits_0^{t-x} G(\bar{x})d\bar{x} \\
&= \frac{1}{2}[F(x+t) - F(t-x)] + \frac{1}{2}\int\limits_{t-x}^{t+x} G(\bar{x})d\bar{x} \qquad (3.13)
\end{aligned}$$

This solution is valid for all $t > 0$ and $x > 0$, provided we have initial data for all $x > 0$.

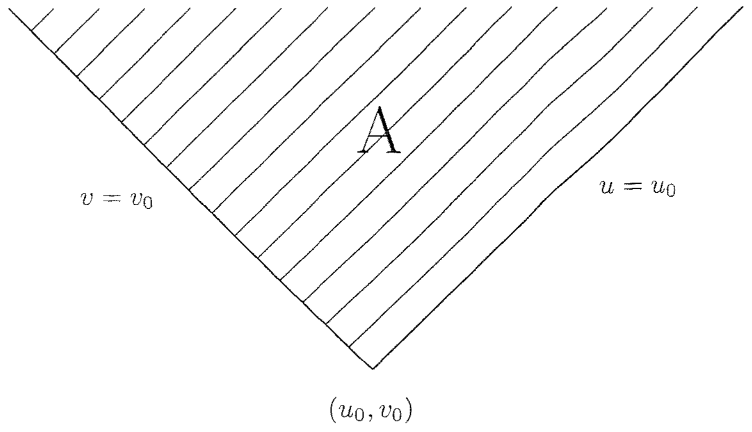

Figure 3.3: The double-null initial value problem. Initial data is prescribed on $u = u_0$ and $v = v_0$ and the solution, calculated using eq. (3.21) is valid in the shaded area A.

### 3.1.2 The Double-Null Initial Value Problem

Equation (3.1) can be re-written in terms of the characteristic coordinates $u$ and $v$ using the transformations

$$\partial_t\Psi \to \partial_u\Psi\partial_t u + \partial_v\Psi\partial_t v = \partial_u\Psi + \partial_x\Psi \tag{3.14}$$

$$\partial_x\Psi \to \partial_u\Psi\partial_x u + \partial_v\Psi\partial_x v = -\partial_u\Psi + \partial_x\Psi \tag{3.15}$$

$$\partial_t t\Psi \to \partial_{uu}\Psi + 2\partial_{uv}\Psi + \partial_{vv}\Psi \tag{3.16}$$

$$\partial_x x\Psi \to \partial_{uu}\Psi - 2\partial_{uv}\Psi + \partial_{vv}\Psi \tag{3.17}$$

The wave equation becomes

$$\partial_{uv}\Psi = 0 \tag{3.18}$$

The initial data is

$$\Psi = \varphi(u) \text{ on } v = v_0 \tag{3.19}$$

$$\Psi = \chi(v) \text{ on } u = u_0 \tag{3.20}$$

The solution in the area A of Fig. 3.3 is [76]

$$\Psi(u, v) = \varphi(u) + \chi(v) - \varphi(u_0) \tag{3.21}$$

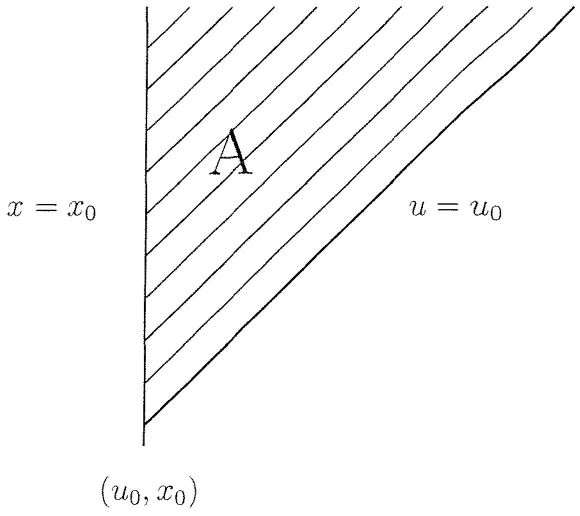

Figure 3.4: The null-timelike initial value problem. Initial data is prescribed on $u = u_0$ and $x = x_0$. The solution is given by eq. (3.29) in the shaded area $A$.

### *3.1.3 The Null-Timelike Initial Value Problem*

The one-dimensional wave equation can be written in the null-timelike coordinates, $(u, x)$ using the transformations

$$\partial_t \Psi \to \partial_u \Psi \partial_t u + \partial_x \Psi \partial_t x = \partial_u \Psi \tag{3.22}$$

$$\partial_{tt} \Psi \to \partial_{uu} \Psi \tag{3.23}$$

$$\partial_x \Psi \to \partial_u \Psi \partial_x u + \partial_x \Psi \partial_x x = -\partial_u \Psi + \partial_x \Psi \tag{3.24}$$

$$\partial_{xx} \Psi \to \partial_{uu} \Psi - 2\partial_{ux} \Psi + \partial_{xx} \Psi \tag{3.25}$$

The wave equation becomes

$$2\partial_{ux} \Psi - \partial_{xx} \Psi = 0 \tag{3.26}$$

Our initial data is

$$\Psi = \varphi(u) \text{ on } x = x_0 \tag{3.27}$$

$$\Psi = \chi(x) \text{ on } u = u_0 \tag{3.28}$$

The general solution in the area A of Figure 3.4 is [76]

$$\Psi(u, x) = \varphi(u) + \chi\left[x + \frac{1}{2}(u - u_0)\right] - \chi\left[x_0 + \frac{1}{2}(u - u_0)\right] \tag{3.29}$$

### *3.1.4 Transforming Initial Data*

We can use the above solutions to transform initial Cauchy data into characteristic initial data. For example, with initial Cauchy data as in (3.5) and (3.6) we find the general solution from (3.10), and written in terms of $u$ and $v$ this gives

$$\Psi(u,v) = \frac{1}{2}[F(v) + F(-u)] + \frac{1}{2}\int\limits_{-u}^{v} G(\bar{x})d\bar{x} \tag{3.30}$$

which gives us our initial data on $u = u_0$

$$\Psi(u_0,v) = \frac{1}{2}[F(v) + F(-u_0)] + \frac{1}{2}\int\limits_{-u_0}^{v} G(\bar{x})d\bar{x} = \chi(v) \tag{3.31}$$

and on $v = v_0$

$$\Psi(u,v_0) = \frac{1}{2}[F(v_0) + F(-u)] + \frac{1}{2}\int\limits_{-u}^{v_0} G(\bar{x})d\bar{x} = \varphi(u) \tag{3.32}$$

To show that this is indeed the same problem, we can substitute these initial data into eq. (3.21), the double-null solution and we recover the original Cauchy solution.

$$\Psi = \frac{1}{2}[F(v) + F(-u)] + \frac{1}{2}\int\limits_{-u}^{v} G(\bar{x})d\bar{x} = \varphi(u) \tag{3.33}$$

so the two initial value formulations are equivalent except that the areas in which the solutions are valid are different.

An analogous calculation shows that the null-timelike formulation is also equivalent.

In this way we can transform our initial data from one formulation to another when the analytic solution is known. If such a solution is known, however, we would not require a numerical evolution, therefore we need to consider how the initial data can be transformed for more complicated evolutions where there is no known analytic solution. I return to this problem in section (5.4).

# Chapter 4

# Numerical Techniques

The wave equation is very simple to solve analytically, however this is not the case for all partial differential equations (PDEs), especially if they are non-linear. When we cannot find an analytic solution, numerical techniques may be employed to find an approximate solution. This section introduces the basic numerical techniques for solving PDEs. These techniques will be applied throughout the later sections. I have relied heavily on one book, *Numerical Recipies* [77] for much of this chapter.

## 4.1 Finite Differencing

Given a particular set of initial data we can evolve our equations numerically on a *numerical grid*, Fig. 4.1, consisting of discrete points $(x_k, t^n)$ at which we find approximated solutions $p_k^n$. Using a *finite differencing* approach, derivatives are

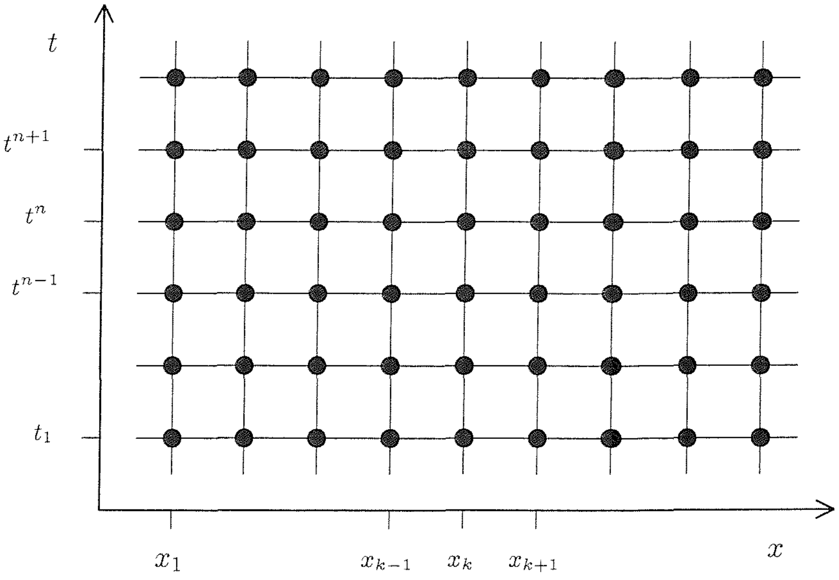

Figure 4.1: A numerical grid. Spacetime approximated by regularly spaced discrete points. The timestep is labelled using the superscript $n$ and the spatial position of each gridpoint is labelled using the subscript $k$.

approximated, in terms of the solutions, $p_k$, and the grid spacing, $\Delta x$, by Taylor expansion. In order to approximate the spatial derivative of some function $f$ at grid point $x_k$ we expand $f$ in a Taylor series about $x_k$.

$$\begin{aligned}\frac{df_k}{dx} &= \frac{f_{k+1}-f_{k-1}}{2\Delta x} + O(\Delta x^2) &\qquad (4.1)\\ \frac{d^2 f_k}{dx^2} &= \frac{f_{k+1}-2f_k+f_{k-1}^n}{\Delta x^2} + O(\Delta x^2) &\qquad (4.2)\end{aligned}$$

Time derivatives may similarly be approximated by

$$\begin{aligned}\frac{df^n}{dt} &= \frac{f^{n+1}-f^{n-1}}{2\Delta t} + O(\Delta t^2) &\qquad (4.3)\\ \frac{d^2 f^n}{dt^2} &= \frac{f^{n+1}-2f^n+f^{n-1}}{\Delta t^2} + O(\Delta t^2) &\qquad (4.4)\end{aligned}$$

We can approximate a derivative as a linear combination of the function at any number of its nearby points but the further these points are from the point at which we want to calculate the derivative, the less accurate our approximation will be. The finite difference approximations in eqs. (4.1)–(4.4) are said to be of *second-order* because the corrections to the derivatives are of order $\Delta x^2$ or $\Delta t^2$, i.e. the solution itself is correct to second order, with corrections of order $\Delta x^3$ or $\Delta t^3$.

## 4.2 Numerical Integration.

The general problem of numerical integration is to approximate the solution to a differential equation

$$\frac{dy(x)}{dx} = f(x,y) \tag{4.5}$$

where the function $f$ is known.

### *4.2.1 The Shooting Method*

Given the value of $y$ at one point, $x_0$, we know the gradient of $y$ at this point from the differential equation, and we want to know the value of $y$ at another point $x_f$. The simplest approach is to use linear interpolation.

$$\begin{aligned}y(x_f) &= y(x_0) + \int_{x_0}^{x_f} f(\bar{x}, y(\bar{x}))d\bar{x}\\ &\approx y_0 + (x_f - x_0) f(x_0, y_0) &\qquad (4.6)\end{aligned}$$

For increased accuracy the interval $x_f - x_0$ can be divided using a sequence of points, $x_0$, $x_1 = x_0 + h$, $x_2 = x_0 + 2h$,..., where $h$ is the spacing between consecutive points, and the recursive scheme

$$y_{n+1} = y_n + hf(x_n, y_n) \tag{4.7}$$

which is known as Euler's method can be employed. This method is the cornerstone of the numerical analysis of differential equations. Although Euler's method is only first order (the order of the truncation error), it serves as the basis for higher order methods. Euler's method advances the solution through the interval, $h$, but uses derivative information from the beginning of the interval only. It clearly is more sensible to use the value of the derivative at the center of the interval, which is approximated as the average of the derivative at the two points. This gives us the trapezoidal rule

$$y_{n+1} = y_n + \frac{1}{2}h[f(x_n, y_n) + f(x_{n+1}, y(x_{n+1}))] \tag{4.8}$$

which is a second order method. Unfortunately this scheme is *implicit* due to the fact that we require information at the point which we are trying to calculate and this makes it a lot more complicated to use. The Euler and trapezoidal methods can be combined in the Heun predictor-corrector scheme. Equation 4.8 is the corrector to the predictor of equation 4.7 and this is a semi-implicit scheme which is second order accurate.

Another option is to use Euler's method to take a preliminary step to the midpoint, $0.5h$, of the interval and to use the values of $x$ and $y$ at that midpoint to integrate across the whole interval,$h$.

$$k_1 = hf(x_n, y_n) \tag{4.9}$$

$$k_2 = hf(x_n + \frac{1}{2}h, y_n + \frac{1}{2}k_1) \tag{4.10}$$

$$y_{n+1} = y_n + k_2 + O(h^3) \tag{4.11}$$

This is called the second-order Runge-Kutta or midpoint method. We can further develop the Runge-Kutta method up to any order by introducing more auxiliary variables. The most popular method is the classical fourth-order Runge-Kutta method which I will use in later sections.

$$k_1 = hf(x_n, y_n) \tag{4.12}$$

$$k_2 = hf(x_n + \frac{h}{2}, y_n + \frac{k_1}{2}) \tag{4.13}$$

$$k_3 = hf(x_n + \frac{h}{2}, y_n + \frac{k_2}{2}) \tag{4.14}$$

$$k_4 = hf(x_n + h, y_n + k_3) \tag{4.15}$$

$$y_{n+1} = y_n + \frac{k_1}{6} + \frac{k_2}{3} + \frac{k_3}{3} + \frac{k_4}{6} + O(h^5) \tag{4.16}$$

### *4.2.2 Relaxation*

Another type of integration problem in one dimension is the *two point boundary problem* in which the solution to a particular ordinary differential equation (ODE) is known at two different positions, i.e. at the boundaries. In this case, using the method of *relaxation*, the solution at all other points on the one-dimensional grid can be found simultaneously. The relaxation method begins with an initial guess for the solution and iteratively improves this guess until the corrections are below a specified tolerance.

Any ODE may be written as a system of first order equations, so here we may consider, without loss of generality, a system of $N$ first order equations on $M$ gridpoints. The solution consists of $M \times N$ values, requiring us to solve a matrix of size $(MN) \times (MN)$. Ordinarily this would require a great amount of time and storage space, but fortunately it is possible to write the matrix in a special *block diagonal* form that allows it to be inverted in a more economical way.

Let $\mathbf{y}_k$ be the set of dependent variables at point $x_k$ where $x$ is the independent variable and $k$ labels the gridpoints, $k = 0, 1, 2, .., M$. Each ODE may be written in a finite difference form which couples two neighbouring points,

$$\mathbf{S} = \mathbf{y}_k - \mathbf{y}_{k-1} - (x_k - x_{k-1})\mathbf{F}(x_k, x_{k-1}, \mathbf{y}_k, \mathbf{y}_{k-1}) = 0 \tag{4.17}$$

where

$$\mathbf{F} = \frac{d\mathbf{y}}{dx} \tag{4.18}$$

There are $N$ equations for $2N$ variables at each pair of neighbouring points, $k$ and $k-1$, therefore eq. (4.17) provides a total of $(M-1)N$ equations for $MN$ unknowns. The boundary conditions provide the remaining N equations.

By expanding the equations for $\mathbf{S}$ in first-order Taylor series with respect to small $\Delta\mathbf{y}_k$ we get

$$\mathbf{S}_k(\mathbf{y}_k + \Delta\mathbf{y}_k, \mathbf{y}_{k-1} + \Delta\mathbf{y}_{k-1}) \approx \mathbf{S}_k(\mathbf{y}_k, \mathbf{y}_{k-1}) + \sum_{n=1}^{N} \frac{\partial \mathbf{S}_k}{\partial y_{n,k-1}} \Delta y_{n,k-1} + \sum_{n=1}^{N} \frac{\partial \mathbf{S}_k}{\partial y_{n,k}} \Delta y_{n,k} \tag{4.19}$$

where $\mathbf{S}_k(\mathbf{y}_k, \mathbf{y}_{k-1})$ represents a close guess to the solution and $\mathbf{S}_k(\mathbf{y}_k + \Delta\mathbf{y}_k, \mathbf{y}_{k-1} + \Delta\mathbf{y}_{k-1})$ represents the actual solution. We solve eq. (4.19) for $\Delta\mathbf{y}$ such that $\mathbf{S}(\mathbf{y} + \Delta\mathbf{y}) = 0$.

The quantity $\partial\mathbf{S}_k/\partial_{n,k}$ can be written as a $N \times 2N$ matrix at each point $k$, representing the $N$ equations coupling $2N$ corrections to the variables at points $k$ and $k-1$. When the equations over all neighbouring pairs are considered along with the boundary conditions, the total matrix size is $(MN) \times (MN)$ but it can be written in a particular block diagonal form so that it can be solved more easily by Gaussian elimination. Some element of each block may be reduced to zero, leaving a square block of elements which can be further reduced by row operations to diagonal form with diagonal elements of unity and off-diagonal elements of zero. The solution is then obtained by backsubstitution.

The entire procedure may seem quite complicated, but fortunately there are standard subroutines available (see e.g. [77] for subroutines and more detailed explanation of methods) for which we need only supply the differential equations themselves and the $N \times 2N$ Jacobian matrix.

## 4.3 Numerical Evolution

For the problems I consider in this thesis I will need to integrate forward not only in space but also in time. In the Cauchy initial value formulation we know the solution at all points on one time slice and must advance the solution to the next timeslice using our finite differenced derivatives. In this way the solution is *evolved* on a numerical grid. In the characteristic initial value problem, the solution is evolved from one characteristic slice to the next.

### *4.3.1 Explicit and Implicit Evolution*

Numerical evolution by the finite difference approach can be carried out using either an *explicit* or *implicit* numerical scheme.

In an explicit evolution the solution is advanced one gridpoint at a time by using information from only a few nearby points on previous timeslices. A common example of such a scheme is the leapfrog scheme which will be used in later chapters. A stencil for the leapfrog scheme is shown in Fig. 4.2. The $x$ derivatives are calculated as in eqs. (4.1)-(4.4), and similarly for the $t$ derivatives. In this way the difference scheme is centered at the point $x_k^n$.

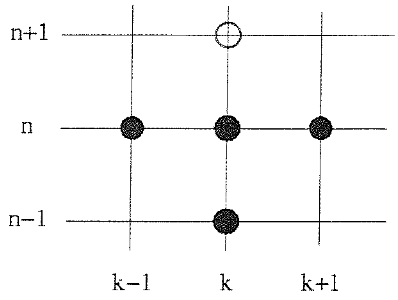

Figure 4.2: The leapfrog finite difference scheme. Information from the black gridpoints is required to find the solution at the gridpoint marked with an unfilled circle.

Information from points $x_{k-1}^n, x_k^n$ and $x_{k+1}^n$ as well as $x_k^{n-1}$ is required in order to approximate the solution at $x_k^{n+1}$. A more detailed explanation of this and other explicit evolution schemes may be found in Chapter 5 which describes how to apply these schemes for evolving the one-dimensional wave equation.

An implicit evolution is based upon the relaxation method described in section 4.2.2. The solution is calculated simultaneously for all gridpoints on an entire timeslice using information from the previous timeslice and the boundary conditions. In Chapter 10 I use a two-level evolution scheme, requiring information from the previous timeslice, to investigate the evolution of oscillations in an incompressible thin spherical shell. Fig. 4.3 shows the stencil for such a scheme.

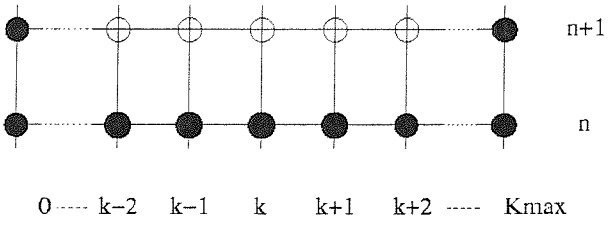

Figure 4.3: An implicit finite difference scheme. Information from all points on the current timeslice (the black gridpoints) is required, along with the boundary conditions, to calculate the solution for all points on the next timeslice (the unfilled gridpoints).

Although implicit methods demand greater computational expense at each timestep, this is usually compensated for by being able to take larger steps. Some caution must be taken however not to take steps which are too large as that may decrease the accuracy of the solution. The timesteps must be small enough to resolve the dynamics of the physical system, e.g. the oscillations.

### *4.3.2 Boundary Conditions*

A numerical grid is by necessity finite in extent and therefore has boundaries. It is important to know how the solution behaves at the boundary. Boundary conditions are implemented in order to evolve the innermost and outermost gridpoints. In the case of the flat space wave equation, analytic boundary conditions are known at any point, depending on the physical situation under consideration. However, in the evolution of more complicated equations, where no analytic solution is known, implementing the appropriate boundary conditions can be a difficult problem. This problem is one of the main obstacles in numerical relativity, and it is precisely to overcome this problem that the characteristic initial value formulation has been taken up here. The advantage of a characteristic formulation in radiation problems is that we can compactify along the characteristic hypersurface in order to include future null infinity on the numerical grid. For asymptotically flat spacetimes we can then apply an exact boundary condition.

### *4.3.3 Stability*

An important factor to consider in the design of an evolution code is stability. Growing numerical errors can lead to disasterous results and a useless code.

One factor determining the stability of a given finite differencing scheme is called the Courant factor. Every PDE has a domain of dependency and every point will depend on information from its domain. A finite differencing scheme similarly has its own domain of dependency determined by the choice of points on one timeslice whose values are used to determine the solution at the new point. For Courant stability, the differencing domain of dependence must include that of the PDEs, otherwise there will be a lack of information at the new point and this will lead to instability. See Fig. 4.4 for an explanation.

Another way to analyse the stability of a particular scheme is the Von Neumann stability analysis. This analysis is local in the sense that the coefficients of the finite difference equations are considered to be constant in space and time. Then the eigenmodes of the difference equations are of the form

$$\Psi_k^n = \xi^n e^{i\lambda k \Delta x} \tag{4.20}$$

where $\lambda$ is a real spatial wave number and $\xi = \xi(\lambda)$ is a complex number. This is substituted into the finite difference equation and the resulting equation can be

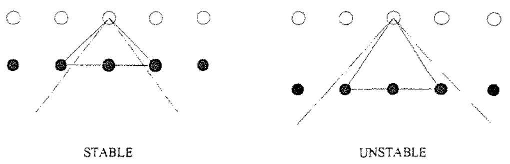

Figure 4.4: Courant stability. The lighter lines indicate the PDE domain of dependence, darker lines indicate the differencing domain of dependence. The finite difference domain of dependence marks the boundaries of the space that is allowed to communicate with the new, unknown point. If the all the PDE domain is within it then all the information can flow freely to the new point but if any of the PDE domain is outside then information will be restricted from reaching the new point and the evolution will be unstable.

solved for $\xi$. Stability requires that there are no growing modes present, therefore the Von Neumann stability condition is $|\xi(\lambda)| < 1$.

The Von Neumann analysis is not a rigorous test of stability, it ignores non-local effects and does not take boundary conditions into account, but despite this it is generally a good test and usually gives dependable conditions for stability.

Specific examples demonstrating the application of this method can been seen in Chapter 5 for the one-dimensional wave equation.

### *4.3.4 Convergence*

Once we have a stable scheme and our code is producing reasonable results, we may like to check the accuracy of the results. One way to do this is through convergence testing. As the grid resolution is increased (i.e. the grid spacing is decreased) we expect the accuracy of the results to increase in proportion to the order of the finite difference scheme used and to tend towards the actual solution at a corresponding rate.

To test convergence towards a known analytic solution we output two sets of data, $\Psi_1$ and $\Psi_2$, from our evolution code - using $M$ gridpoints and using $2M$ gridpoints respectively. We calculate the L2 norm on each timeslice by taking the difference between the data and the analytic solution, $\Psi_a$, at each gridpoint, squaring it, summing over the whole timeslice, and dividing by the number of gridpoints. The convergence factor is given by the L2 norm for the lower resolution data, divided by the L2 norm of the higher resolution data.

$$C = \frac{[\sum(\Psi_a^2 - \Psi_1^2)]^{1/2}}{[\sum(\Psi_a^2 - \Psi_2^2)]^{1/2}} \tag{4.21}$$

The error in $\Psi$ should be of the order $(\Delta x)^n$ where $n$ is the order of the differencing scheme. The converegence should therefore be given by

$$C = \frac{(\Delta x)^n}{\left(\frac{\Delta x}{2}\right)^n} = 2^n \tag{4.22}$$

This convergence factor can be plotted as a function of time. For a second order accurate finite difference scheme, the convergence factor is expected to have a value of about four.

When there is no analytic solution, this is replaced by data from a yet higher resolution run of $4M$ gridpoints. In this case, the convergence factor should be given by

$$C = \frac{(\Delta x)^n - \left(\frac{\Delta x}{4}\right)^n}{\left(\frac{\Delta x}{2}\right)^n - \left(\frac{\Delta x}{4}\right)^n} = \frac{1 - (\frac{1}{4})^n}{(\frac{1}{2})^n - (\frac{1}{4})^n} \tag{4.23}$$

For this method, a second order finite difference scheme should give a convergence factor of about five.

# Chapter 5

# The One Dimensional Wave Equation in Flat Space.

Again, we consider the simple one-dimensional wave equation. Fortunately, the equations we would like to solve later, i.e. those governing black hole perturbations, turn out to be fairly simple - wave equations with potentials, therefore many of the techniques learned here will be useful in later, more complicated evolutions. In this chapter I evolve the one dimensional wave equation numerically for the three different initial value problems introduced in Chapter 3

## 5.1 Cauchy Evolution

We set up a numerical grid of spacial length $L$ and grid spacing $\Delta x$ and $\Delta t$. As our initial data we consider a small Gaussian pulse travelling in the direction of decreasing $x$.

Instead of using the usual Cauchy initial data, $\Psi$ and $\partial_t \Psi$, we can use, equivalently, $\Psi_0$ on the first timeslice and $\Psi_1$ on the second timeslices.

The wave equation is written in finite difference form as

$$p_k^{n+1} = 2p_k^n - p_k^{n-1} + (p_{k+1}^n - 2p_k^n + p_{k-1}^n)\mu^2 \tag{5.1}$$

This is an example of the leapfrog scheme described in section 4.3.1 where $\mu = \Delta t/\Delta x$ is the Courant factor which determines the stability of the evolution scheme. In eq. (5.1), the solution at $x_k^{n+1}$ is computed using information from $x_{k-1}^n$ and $x_{k+1}^n$, but the information cannot propagate faster than the speed of light and lack of information leads to instability. If $\Delta t$ is made too large then necessary information cannot reach $x_k^{n+1}$. $\Delta t/\Delta x$ must be smaller than 1 (speed of light, $c = 1$) and therefore the wave equation requires a Courant factor of between 0 and 1 for stability.

We can check for Von Neumann stability by substituting eq. (4.20) into eq. (5.1)

$$\xi = 2 - \xi^{-1} + (e^{i\lambda x} - 2 + e^{-i\lambda x})\mu^2 \tag{5.2}$$

This can be re-arranged to give

$$\xi^2 - [2 - 4\sin^2\left(\frac{\lambda x}{2}\right)\mu^2]\xi + 1 = 0 \tag{5.3}$$

where we have substituted

$$e^{i\lambda x} - 2 + e^{-i\lambda x} = -4\sin^2\left(\frac{\lambda x}{2}\right) \tag{5.4}$$

The solution for $\xi$ is

$$\xi = 1 - \alpha \pm \sqrt{(1-\alpha)^2 - 1} \tag{5.5}$$

where

$$\alpha = 2\sin^2\left(\frac{\lambda x}{2}\right)\mu^2 \tag{5.6}$$

The condition for stability is

$$|\xi| \leq 1 \tag{5.7}$$

If the quantity under the square root in eq. (5.5) is negative, i.e. $(1-\alpha)^2 < 1$ then we have

$$|\xi| = \sqrt{2(1-\alpha)^2 - 1} \tag{5.8}$$

which is always less than 1 in this case. The quantity under the square root in eq. (5.5) can never be positive because $\alpha$ is always positive, i.e. $1 - \alpha$ can never be greater than unity. If the quantity under the square root in eq. (5.5) is zero, i.e. $1 - \alpha = 1$ then we have

$$|\xi| = 1 \tag{5.9}$$

So we require, from eq. (5.8), $|1 - \alpha| \leq 1$ i.e. $|\alpha| \leq 2$

$$\sin^2\left(\frac{\lambda x}{2}\right)\mu^2 \leq 1 \rightarrow \mu \leq 1 \tag{5.10}$$

where the last part follows from the fact that the inequality must hold for all $x$. This gives us the Courant condition again, $\Delta t \leq \Delta x$.

I have prescribed Gaussian initial data, travelling to the left. This is represented on the first two timeslices as

$$\Psi_k^0 = Ae^{-b((k\Delta x)-\Delta t-x_c)^2} \tag{5.11}$$

$$\Psi_k^1 = Ae^{-b((k\Delta x)-x_c)^2} \tag{5.12}$$

where $A$ determines the amplitude and $b$ determines the width of the pulse which is centered at $x_c$.

I have evolved the wave equation using this scheme for two different cases. One represents a pulse travelling on an infinite string and in the other, the string is tied at the origin. In the first case, we must formulate boundary conditions which allow the pulse to travel off the numerical grid. These *radiation boundary conditions* can be found by an analysis of the d'Alembert solution for the one-dimensional wave equation, eq. (3.2). At the inner boundary, $x_0$, we must have no right travelling waves, i.e. $f(u) = const$. At the outer boundary, $x_K$, there must be no left travelling waves, i.e. $g(v) = const$. This gives us the following boundary conditions

$$\partial_t\Psi - \partial_x\Psi = 0 \qquad \text{at } x = x_0 \tag{5.13}$$

$$\partial_t\Psi + \partial_x\Psi = 0 \qquad \text{at } x = x_K \tag{5.14}$$

In 1st order finite difference form we have

$$p_0^{n+1} = p_0^n + \frac{\Delta t}{\Delta x}(p_1^n - p_0^n) \qquad \text{at } x = x_0 \tag{5.15}$$

$$p_K^{n+1} = p_K^n - \frac{\Delta t}{\Delta x}(p_K^n - p_{K-1}^n) \qquad \text{at } x = x_K \tag{5.16}$$

In the second case, a zero boundary condition is implemented at the inner boundary

$$p_0^{n+1} = 0 \tag{5.17}$$

We can calculate the analytic solution in both these cases. For an infinite string the solution is given by eq. (3.2). Substituting our initial data of a pulse moving in the negative $x$ direction into this equation we find (as expected)

$$\Psi(x,t) = Ae^{-b(x-x_c+t)^2} \tag{5.18}$$

For a semi infinite string we have from eq. (3.13)

$$\Psi(x,t) = Ae^{-b(x-x_c+t)^2} - Ae^{-b(-x-x_c+t)^2} \tag{5.19}$$

The results of the numerical evolution in both these cases are shown in Figs. 5.1 and 5.2

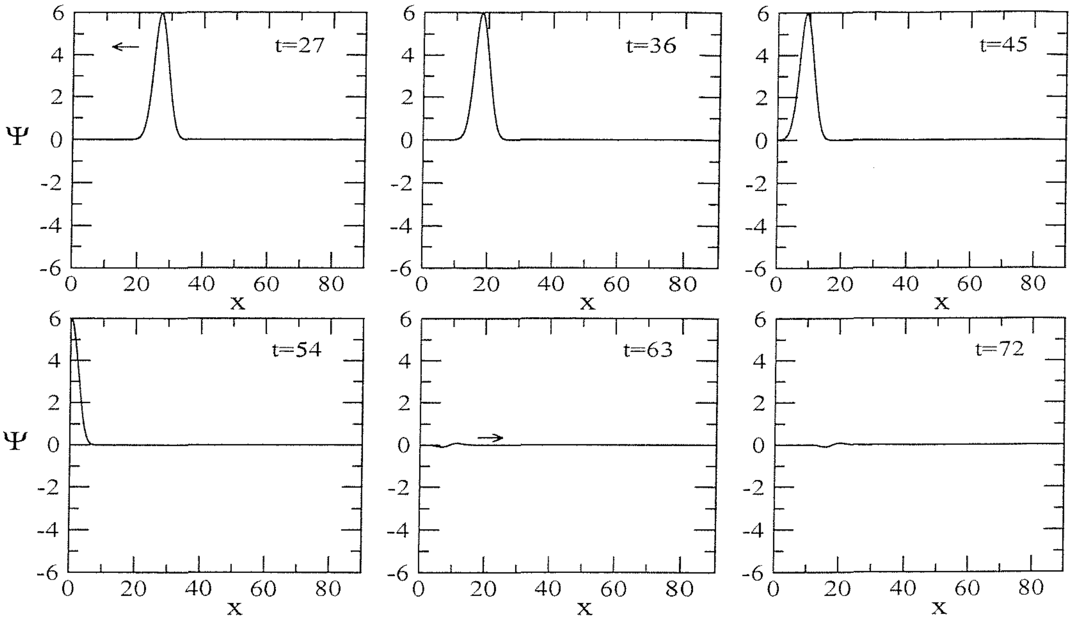

Figure 5.1: Cauchy evolution for the one-dimensional wave equation with a 1st order radiation inner boundary condition. Most of the pulse travels off the grid, but a small numerical reflection can be seen in the last two time slices.

We see that zero boundary conditions cause inversion and reflection at the boundary, whereas radiation boundary conditions allow the pulse to pass through. There is some small reflection at the boundary even with radiation boundary conditions. This is due to numerical error and can be reduced by increasing the grid resolution. The amplitude of this numerical reflection is reduced by a change to second order radiation boundary conditions.

The second order finite difference scheme for the ingoing radiation boundary condition is

$$p_0^{n+1} = \frac{2}{3(\Delta t + \Delta x)} \left[ \Delta t \left( 2p_1^{n+1} - \frac{1}{2} p_2^{n+1} \right) + \Delta x \left( 2p_0^n - \frac{1}{2} p_0^{n-1} \right) \right] \tag{5.20}$$

$$p_K^{n+1} = \frac{2}{3(\Delta t + \Delta x)} \left[ \Delta t \left( 2p_{K-1}^{n+1} - \frac{1}{2} p_{K-2}^{n+1} \right) + \Delta x \left( 2p_K^n - \frac{1}{2} p_K^{n-1} \right) \right] \tag{5.21}$$

The results have been tested for convergence to the analytic solution. Convergence plots are shown in Fig. 5.3, Fig. 5.4 and Fig. 5.5. From these plots we can see that the first order boundary conditions cause the entire evolution to fall to 1st

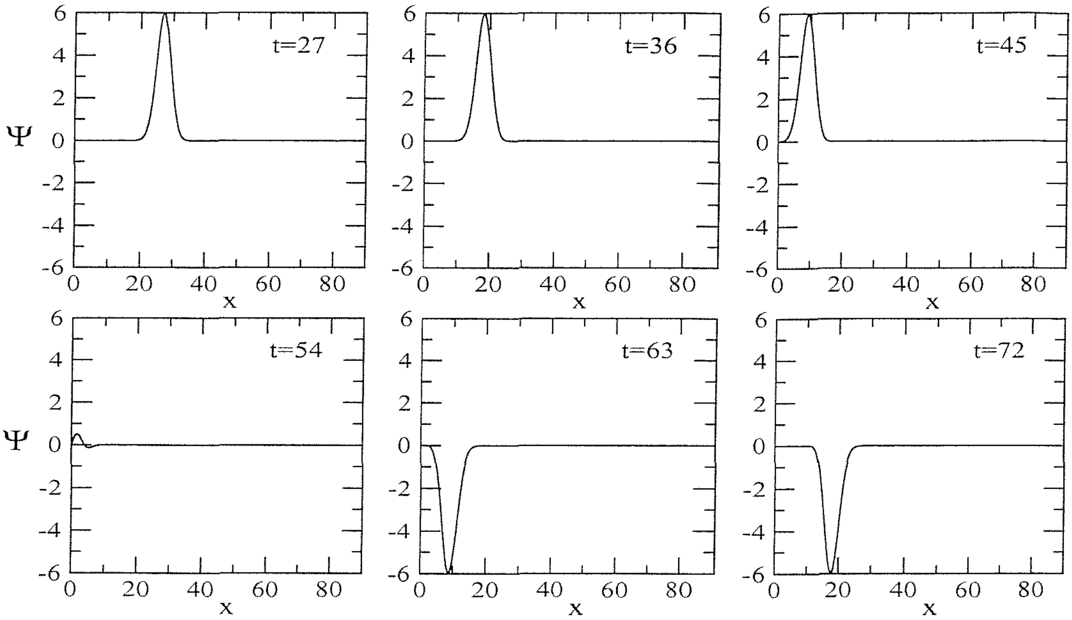

Figure 5.2: Cauchy evolution for the one-dimensional wave equation with zero boundary condition. The wave is reflected and inverted at the inner boundary $x = 0$.

order accuracy following the pulse's contact with the boundary whereas convergence remains more constant with a second order boundary condition. There is still some noise at $t \approx 50 - 60$ in the Figs. 5.4 and 5.5, due to the pulse hitting the inner boundary at this time.

## 5.2 Double-Null Evolution

The one-dimensional wave equation can also be evolved on characteristic surfaces. We use double-null coordinates, $u$ and $v$, as described in section 3.1.2. The numerical grid is set up as in Fig. 4.1 with the $x$ and $t$ axes replaced by $v$ and $u$ axes respectively.

The initial Gaussian pulse is easily transformed into initial data on $u$ and $v$. We have (see eqs. (3.5) and (3.6))

$$F(x) = Ae^{-b(x-x_c)^2} \tag{5.22}$$

$$G(x) = -2b(x - x_c)Ae^{-b(x-x_c)^2} \tag{5.23}$$

$$\int G(\bar{x})d\bar{x} = Ae^{-b(x-x_c)^2} = F(x) \tag{5.24}$$

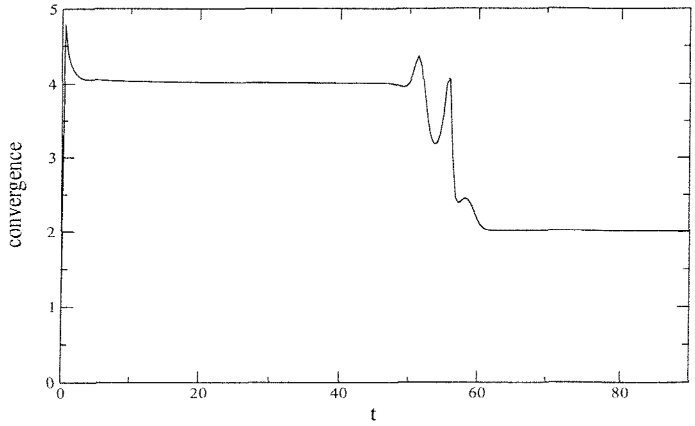

Figure 5.3: Convergence test of the Cauchy evolution of the one-dimensional wave equation with first order boundary condition. The convergence clearly drops to 1st order after the pulse hits the boundary.

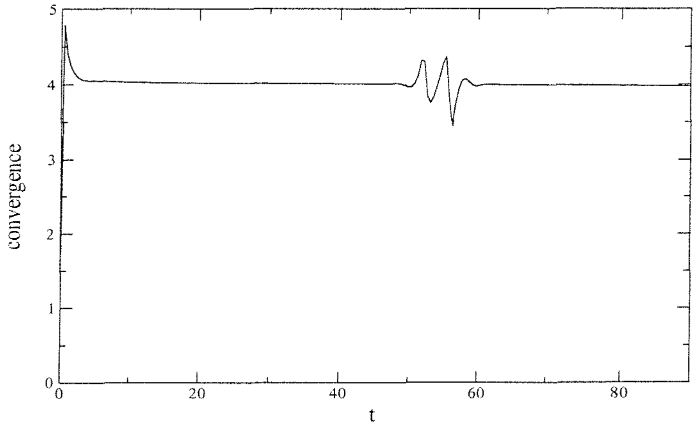

Figure 5.4: Convergence test of Cauchy evolution of one-dimensional wave equation with zero boundary condition, showing second order convergence.

So our initial data on $u = u_0$ is, using eq.( 3.31),

$$\Psi = Ae^{-b(v-x_c)^2} = \chi(v) \tag{5.25}$$

and on $v = v_0$ we find from eq. (3.32),

$$\Psi = Ae^{-b(v_0-x_c)^2} = \varphi = const. \tag{5.26}$$

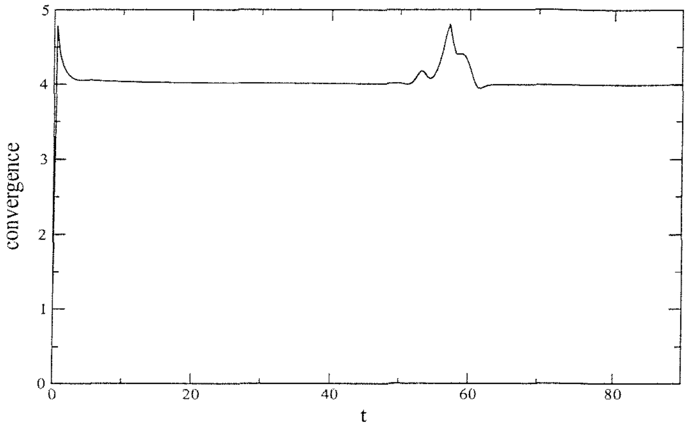

Figure 5.5: Convergence test of Cauchy evolution of one-dimensional wave equation with second order boundary condition, showing second order convergence.

i.e. $\Psi$ is a function of $v$ only. This is what we would expect because we have chosen our pulse to be moving inward only and this was achieved by setting

$$\Psi = g(v), \text{ i.e. } f(u) = 0 \tag{5.27}$$

So our initial Gaussian on a timeslice is transformed to a Gaussian on $u_0$ and a constant on $v_0$.

The finite difference approximation to the wave equation in double-null coordinates is

$$p_{k+1}^{n+1} = -p_k^n + p_{k+1}^n + p_k^{n+1} \tag{5.28}$$

The stencil is shown in Fig. 5.6.

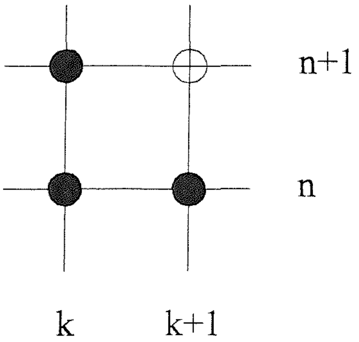

Figure 5.6: Stencil for the double-null evolution of the one-dimensional wave equation. Filled circles represent points at which the solution is already known, the unfilled circle represents the next point at which the solution is to be determined.

The Von Neumann stability analysis shows that this scheme is unconditionally stable:

$$\xi e^{i\lambda x} = -1 + e^{i\lambda x} + \xi \tag{5.29}$$

i.e. $|\xi| = 1$.

Some results from the double-null evolution code are shown in Fig. 5.7 on constant $u$ slices and Fig. 5.8 on constant $v$ slices. As expected, there is no change on the $u$ slices because we have set up our initial pulse moving at the speed of light in the negative $x$-direction. On $v$ slices the solution is a constant which increases from zero as the pulse passes, reaching a maximum at the peak of the pulse, then decreasing back down to zero.

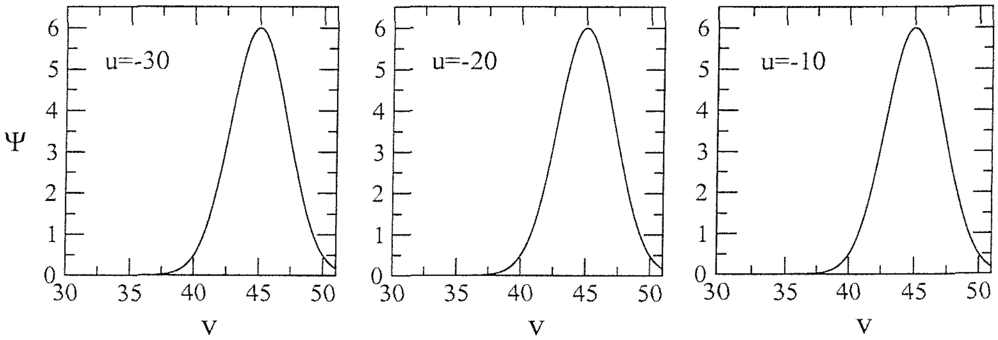

Figure 5.7: Results of double-null evolution of one-dimensional wave equation, displayed on surfaces of constant $u$. The initial pulse stays constant with increasing $u$ because it is moving in the negative $x$-direction at characteristic speed, i.e. the speed of light.

In this evolution, the initial data on $u = u_0$ does not evolve, therefore it is not possible to test convergence as the L2-norm is always zero.

## 5.3 Null-Timelike Evolution

In order to evolve the one-dimensional wave equation as a null-timelike initial value problem we set up our numerical grid as in Fig. 4.1 with the $t$ axis replaced by a $u$ axis. We can finite difference the wave equation using the following second order

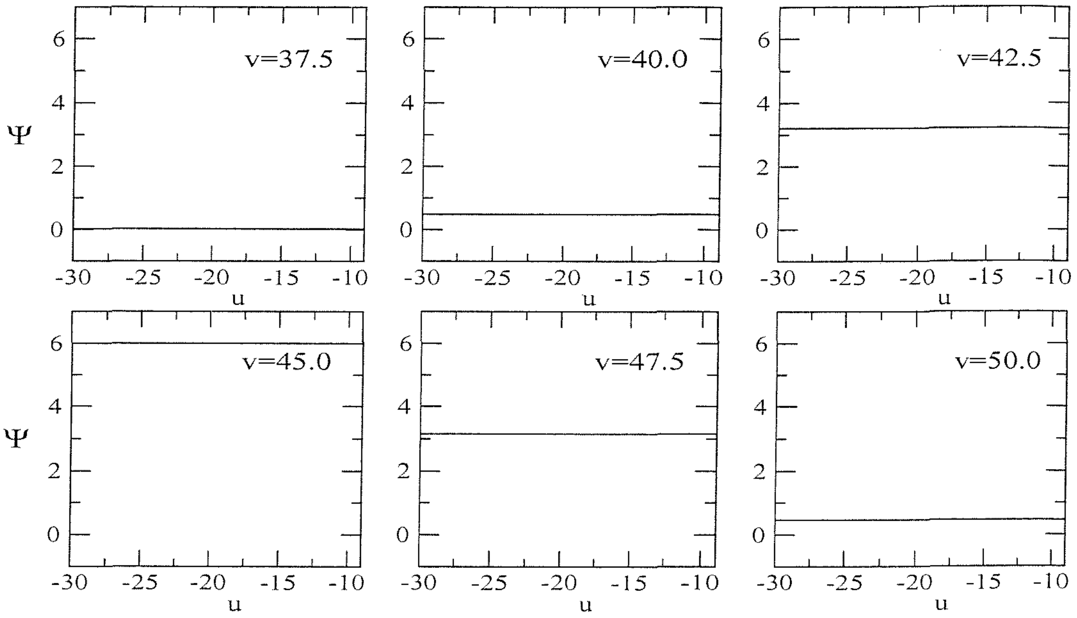

Figure 5.8: Results of double-null evolution of one-dimensional wave equation, displayed on surfaces of constant $u$. As the pulse, travelling in the $u$-direction crosses these surfaces, we see an increase in amplitude up to the peak of the pulse followed by a decrease, returning to zero amplitude when the pulse has passed.

scheme:

$$\partial_{ux}\Psi = \frac{1}{\Delta u \Delta x}\left(p_k^{n+1} - p_{k-1}^{n+1} - p_k^n + p_{k-1}^n\right) \tag{5.30}$$

$$\partial_{xx}\Psi = \frac{1}{2\Delta x^2}\left(p_k^{n+1} - 2p_{k-1}^{n+1} + p_{k-2}^{n+1} + p_{k+1}^n - 2p_k^n + p_{k-1}^n\right) \tag{5.31}$$

where derivatives are centered at position $(k-1/2, n+1/2)$. See Fig. 5.9 for the stencil. This scheme is equivalent to the *marching algorithm* used in numerical relativity [78], and it is described in [79]. The wave equation becomes

$$p_k^{n+1} = \frac{1-2D}{1-D}[p_{k-1}^{n+1} + p_k^n] + \frac{D}{1-D}[p_{k-2}^{n+1} + p_{k+1}^n] - p_{k-1}^n \tag{5.32}$$

where $D = \dfrac{\Delta u}{4\Delta x}$.

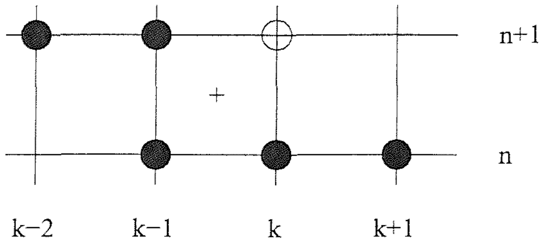

Figure 5.9: Stencil for the null-timelike evolution of the one-dimensional wave equation. Filled circles represent points at which the solution is already known, the unfilled circle represents the next point at which the solution is to be determined. The finite difference equation (5.32) is obtained by approximating the derivatives at the point marked by a plus sign.

We can check for Von Neumann stability by substituting eq. (4.20) into eqs. (5.30) and (5.31)

$$\Delta u \Delta x \partial_{ux} \Psi = (\xi - \xi^{-1})(1 - e^{-i\lambda x})\Psi_l^n \tag{5.33}$$

$$2\Delta x^2 \partial_{xx} \Psi = (1 + e^{-i\lambda x})(e^{i\lambda x} - 2 + e^{-i\lambda x})\Psi_l^n \tag{5.34}$$

Substituting these into the wave equation, and multiplying through by $\xi$ we find

$$\xi^2 + \frac{i \sin \lambda x}{1 - \cos \lambda x} 4 \sin^2\left(\frac{\lambda x}{2}\right)\left(\frac{\Delta u}{2\Delta x}\right)\xi - 1 = 0 \tag{5.35}$$

Using the relation

$$\sin^2\left(\frac{x}{2}\right) = \frac{1}{2}(\cos x - 1) \tag{5.36}$$

we can solve for $\xi$ to find

$$\xi = i\frac{\Delta u}{2\Delta x}\sin \lambda x \pm \sqrt{-\left(\frac{\Delta u}{2\Delta x}\right)^2 \sin^2 \lambda x + 1} \tag{5.37}$$

when $\Delta u < 2\Delta x$ then the term under the square root is real so we find that the magnitude of $\xi$ is

$$\xi\bar{\xi} = 1 \tag{5.38}$$

i.e. this scheme is unconditionally stable.

As can be seen from eq. (5.32), we can only begin to apply this scheme for calculating the solution at the third gridpoint. The boundary point is given as initial data for the null-timelike initial value problem, or can be calculated using some boundary condition. For the first spatial gridpoint from the inner boundary we are forced to slightly modify our scheme, and finite difference as

$$p_1^{n+1} = p_0^{n+1} + p_1^n - p_0^n + \frac{D}{2}(3p_0^n - 7p_1^n + 5p_2^n - p_3^n) \tag{5.39}$$

where we calculate the double $x$ derivative to first order only. As will be seen in the results of convergence testing, this does not seem to affect the overall second order convergence. Our finite difference scheme must also be slightly adjusted at the outer boundary. Applying a second order one-sided derivative for $\partial_{xx}\Psi$ leads to the finite difference equation

$$p_K^{n+1} = \frac{1-2D}{1-D}p_{K-1}^{n+1} + \frac{1+2D}{1-D}p_K^n - \frac{1+5D}{1-D}p_{K-1}^n + \frac{D}{1-D}(p_{K-2}^{n+1} + 4p_{K-2}^n - p_{K-3}^n) \tag{5.40}$$

We again consider both the infinite and semi-infinite cases. The initial data on $u = u_0$ is given by

$$\Psi = Ae^{-b(u_0+2x-x_c)^2} \tag{5.41}$$

The initial data at $x = x_0$ is given by $\Psi = 0$ for the semi-infinite case and

$$\Psi = Ae^{-b(u+2x_0-x_c)^2} \tag{5.42}$$

for the infinite case. Later, in more general cases, we may not have an analytic expression for the initial data at $x = x_0$ so here we impose an ingoing radiation boundary condition in preparation for evolving more complicated equations. In null-timelike coordinates the ingoing radiation boundary condition is

$$2\partial_u\Psi = \partial_x\Psi \tag{5.43}$$

which can be written in second order finite difference form as

$$p_0^{n+1} = 2p_0^n - p_0^{n-1} + \left(\frac{\Delta u}{2\Delta x}\right)^2 (2p_0^n - 5p_1^n + 4p_2^n - p_3^n) \tag{5.44}$$

Results for the null-timelike evolution are shown in Fig. 5.10 for the radiation boundary condition and Fig. 5.11 for the zero boundary condition.

I have tested the convergence for zero and radiation boundary conditions and the results can be seen in Fig. 5.12 and Fig. 5.13. It is apparent from Fig. 5.13 that the implementation of radiation boundary conditions has some problems when the pulse hits the boundary. This will not be a problem in future evolutions however as

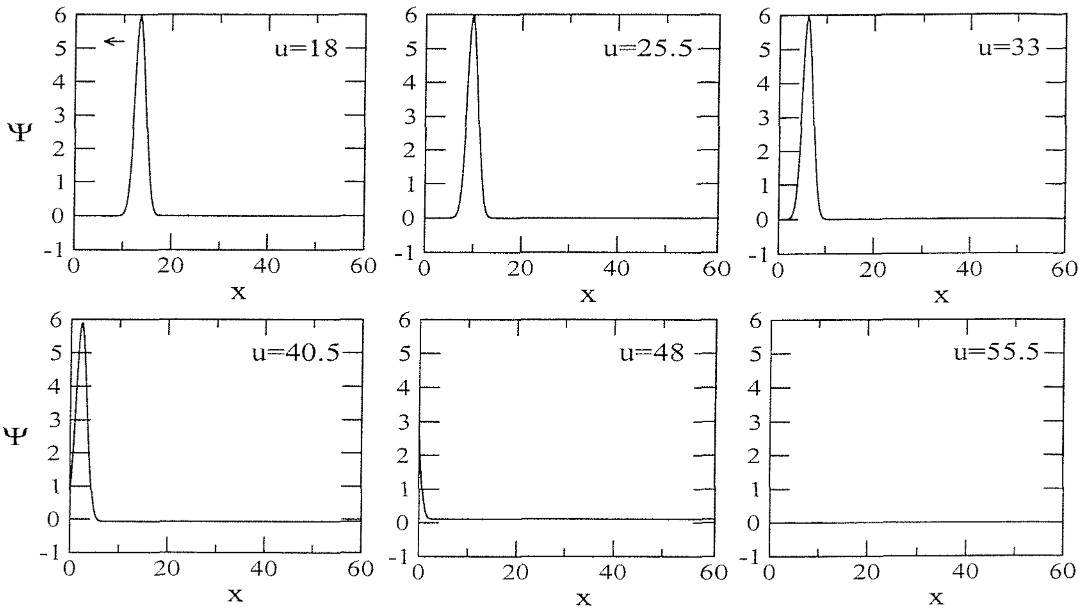

Figure 5.10: Null-timelike evolution of the one-dimensional wave equation with radiation boundary condition. The output is displayed on $u = const.$ slices which are equivalent to and we can see that the radiation travels quite cleanly off the grid at the inner boundary. Some small reflection at the boundary can be seen at $u = 40.5$ and $u = 48$. The reflected radiation travels at the characteristic speed in the positive $x$-direction, i.e. along a surface of $u = const.$, and therefore appears as a straight line here.

we will avoid artificial boundaries altogether. The zero boundary condition shows good second order convergence.

## 5.4 Characteristic Initial Data

In this chapter we have been able to specify equivalent initial data for all three initial value problems because we have an analytic solution to the wave equation. Later, when we consider more complex equations, without known analytic solutions, we may also want to use equivalent initial data. In some cases we may have some initial data specified on a Cauchy hypersurface and want to know how to translate this to initial data on a characteristic hypersurface. One way to do this is to evolve for some time on Cauchy slices, then use interpolation to find the solution on a particular characteristic hypersurface which is within the domain of the Cauchy evolution.

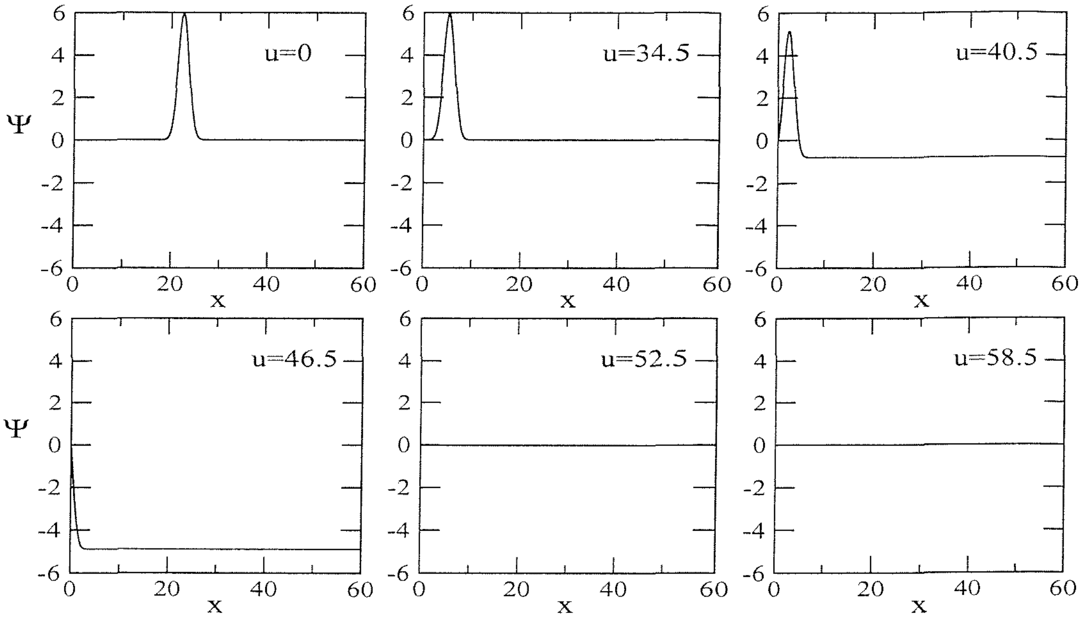

Figure 5.11: Null-timelike evolution of the one-dimensional wave equation with zero boundary condition. The output is displayed on $u = const.$ slices. The reflected and inverted pulse travels back in the negative $x$-direction at the characteristic speed and therefore appears as a straight line of negative amplitude here.

The solution can be found at any position $x$ which lies on the interpolating polynomial though 3 points $y_1 = f(x_1)$, $y_2 = f(x_2)$ and $y_3 = f(x_3)$ as given by the classical Lagrange formula

$$P(x) = \frac{(x-x_2)(x-x_3)}{(x_1-x_2)(x_1-x_3)}y_1 + \frac{(x-x_1)(x-x_3)}{(x_2-x_1)(x_2-x_3)}y_2 + \frac{(x-x_1)(x-x_2)}{(x_3-x_1)(x_3-x_2)}y_3 \tag{5.45}$$

For our spacetime grid, we first interpolate for a solution at $x$ on three timeslices surrounding $(x, t)$ and then use these three values as the points for interpolation to $(x, t)$. This is shown in Fig. 5.14

The solution from the Cauchy evolution can be output on $u$ slices and compared with the solution to both the double-null and null-timelike evolutions. The areas in which comparisons are free from boundary reflections are shown in Fig. 5.15 and Fig. 5.16. Outside these areas the interpolated data may be contaminated by boundary reflections from the Cauchy evolution, depending on the nature of the initial data. In the comparison with null-timelike evolutions there may still be

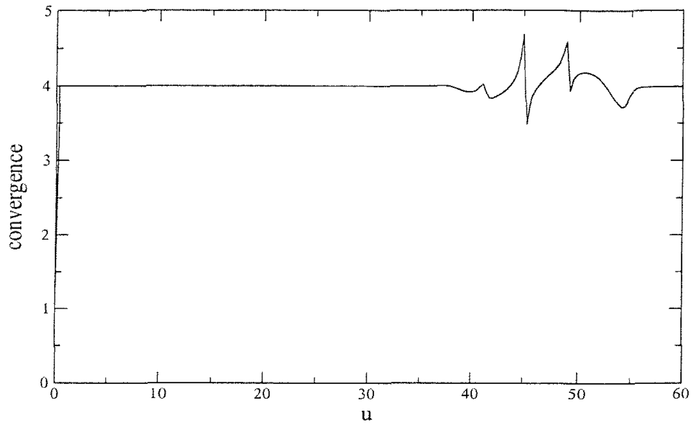

Figure 5.12: Convergence test of null-timelike evolution of the one-dimensional wave equation with zero boundary condition, showing second order convergence.

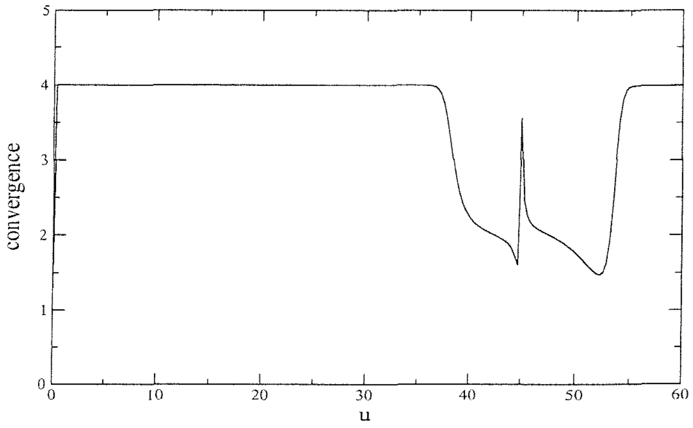

Figure 5.13: Convergence test of null-timelike evolution of the one-dimensional wave equation with radiation boundary condition. There are clearly some convergence problems when the pulse hits the inner boundary at $u \approx 35$. I avoid the use of such boundary conditions in the null-timelike evolutions of later chapters.

reflections from the inner null-timelike boundary at $x = const$ and these could effect the comparison.

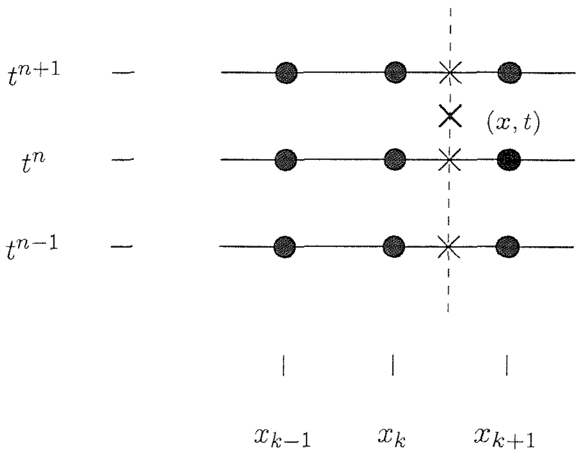

Figure 5.14: Interpolation using three points. First interpolate for a solution at $x$ on three timeslices, i.e. at the points on the timeslices marked with a cross, surrounding $(x, t)$, marked by a bold cross, and then use these three values as the points for interpolation to $(x, t)$.

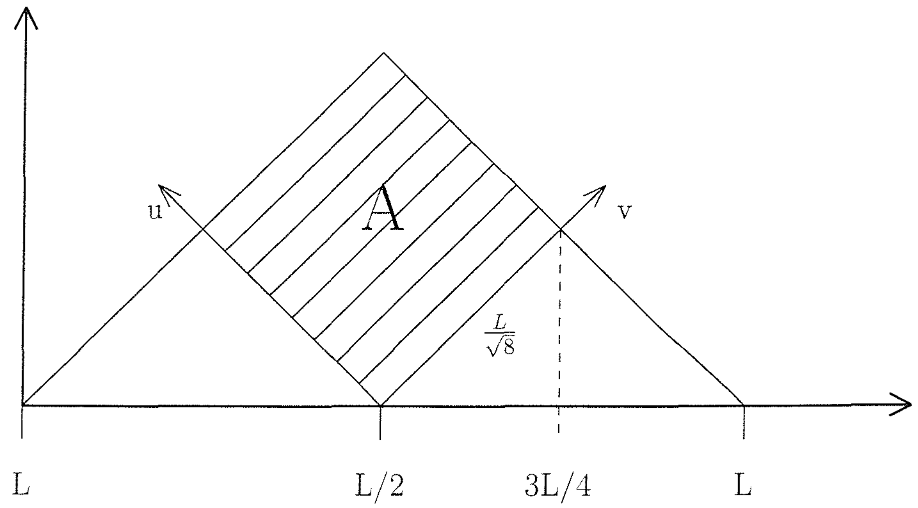

Figure 5.15: The comparison of Cauchy and double-null evolutions is valid in the shaded area. Outside this area, the Cauchy data may be contaminated by spurious reflections.

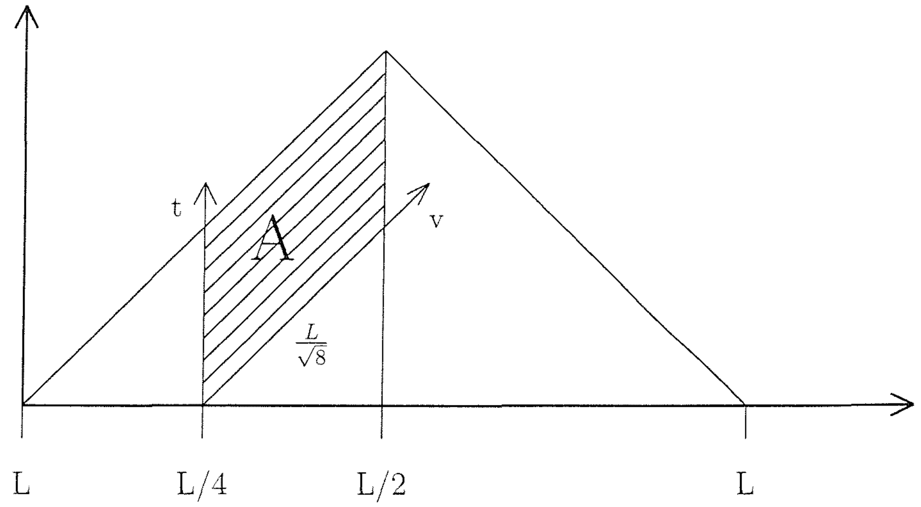

Figure 5.16: The comparison of Cauchy and null-timelike evolutions is valid in the shaded area. Outside this area, the Cauchy data may be contaminated by spurious reflections. This comparison is, however, not free from boundary effects from the null-timelike evolution itself.

# Chapter 6

# Perturbed Schwarzschild Black Holes

In 1957 Regge and Wheeler derived an equation governing small, linear perturbations of a field in Schwarzschild spacetime [15]. In this section I re-derive the Regge Wheeler equation, first for scalar perturbations, then for the more general case, including vector and tensor perturbations. I describe the Green's function approach which can be used to calculate the frequencies of the quasi-normal mode frequencies. I also evolve the scalar equation using the numerical methods outlined for the one-dimensional wave equation in flat space for each of the three initial value problems, Cauchy, double-null, and null-timelike. I introduce compactification in the retarded null coordinate, and combine the evolution on compactified retarded hypersurfaces with an evolution on compactified advanced hypersurfaces by matching, and thus evolve the entire spacetime outside the black hole. I test the results by comparing the quasi-normal mode frequencies, damping and the late time tails to results obtained elsewhere using the Green's function method, and I also test for second order convergence.

## 6.1 The Scalar Wave Equation in Schwarzschild Geometry

Consider a massless scalar field propagating in Schwarzschild geometry. A massless scalar field evolves according to the Klein Gordon eq.

$$\Box\Psi = (-g)^{1/2}\partial_\mu[(-g)^{1/2}g^{\mu\nu}\partial_\nu\Psi] = 0 \tag{6.1}$$

The Schwarzschild metric is given by

$$g_{\mu\nu} = \begin{pmatrix} \frac{2M}{r} - 1 & 0 & 0 & 0 \\ 0 & \left(1 - \frac{2M}{r}\right)^{-1} & 0 & 0 \\ 0 & 0 & r^2 & 0 \\ 0 & 0 & 0 & r^2 \sin^2\theta \end{pmatrix} \tag{6.2}$$

$$g = |g_{\mu\nu}| = -r^4 \sin^2\theta \tag{6.3}$$

and substituting this into eq. (6.1) we find

$$\Box\Psi = \partial_\mu[r^2 \sin\theta g^{\mu\nu}\partial_\nu\Psi] = 0 \tag{6.4}$$

$$\begin{aligned} -r^2\left(1-\frac{2M}{r}\right)^{-1}\partial_{tt}\Psi + r^2\left(1-\frac{2M}{r}\right)\partial_{rr}\Psi + 2r\left(1-\frac{M}{r}\right)\partial_r\Psi \\ +\frac{1}{\sin\theta}\partial_\theta(\sin\theta\partial_\theta\Psi) + \frac{1}{\sin^2\theta}\partial_{\phi\phi}\Psi = 0 \end{aligned} \tag{6.5}$$

When working with a spherically symmetric metric we can introduce the spherical harmonic mode decomposition:

$$\Psi = \Sigma\Psi_{lm} \tag{6.6}$$

$$\Psi_{lm} = \frac{u_{lm}}{r}(r,t)Y_{lm}(\theta,\phi) \tag{6.7}$$

where the $Y_{lm}$ provide a complete set of basis functions, each satisfying

$$\frac{1}{\sin\theta}\partial_\theta[\sin\theta\partial_\theta Y_{lm}] + \frac{1}{\sin^2\theta}\partial_{\phi\phi}Y_{lm} = -l(l+1)Y_{lm} \tag{6.8}$$

By substitution into eq. (6.5) we find

$$\begin{aligned} \Box\Psi_{lm} = \left[-r^2\left(1-\frac{2M}{r}\right)^{-1}\partial_{tt}u_{lm} + r^2\left(1-\frac{2M}{r}\right)\partial_{rr}u_{lm} + 2r\left(1-\frac{M}{r}\right)\partial_r u_{lm}\right]Y_{lm} \\ + \left[\frac{1}{\sin\theta}\partial_\theta(\sin\theta\partial_\theta Y_{lm}) + \frac{1}{\sin^2\theta}\partial_{\phi\phi}Y_{lm}\right]u_{lm} = 0 \end{aligned} \tag{6.9}$$

Using eq. (6.8) we obtain an equation involving only $r$ and $\theta$

$$-r^2\left(1-\frac{2M}{r}\right)^{-1}\partial_{tt}u_{lm} + r^2\left(1-\frac{2M}{r}\right)\partial_{rr}u_{lm} + 2r\left(1-\frac{M}{r}\right)\partial_r u_{lm} = l(l+1)u_{lm} \tag{6.10}$$

We transform to the tortoise coordinate $r_*$

$$\frac{d}{dr_*} = \left(1 - \frac{2M}{r}\right)\frac{d}{dr} \tag{6.11}$$

i.e. $r_* = r + 2Mln\left(\frac{r}{2M} - 1\right)$. The tortoise coordinate goes to minus infinity at the horizon, i.e. $r_* \longrightarrow -\infty$ as $r \longrightarrow 2M$ and $r_* \sim r$ as $r \longrightarrow \infty$. Our equation reduces to

$$[\partial_{tt} - \partial_{r_*r_*} + V_{lm}(r)]u_{lm} = 0 \tag{6.12}$$

where

$$V_{lm}(r) = \left(1 - \frac{2M}{r}\right)\left(\frac{l(l+1)}{r^2} + \frac{2M}{r^3}\right) \tag{6.13}$$

This is the Regge Wheeler equation for scalar perturbations.

## 6.2 The Regge-Wheeler equation

Regge and Wheeler derived their equation by introducing small perturbations, $h_{\mu\nu}$, to the background metric $g_{\mu\nu}^{(B)}$

$$g_{\mu\nu} = g_{\mu\nu}^{(B)} + h_{\mu\nu} \tag{6.14}$$

They considered the linear perturbations to the Ricci tensor $\delta R$ by calculating with the above metric and retaining only terms linear in $h_{\mu\nu}$ whilst discarding higher order terms.

The standard equation for the Christoffel symbols in terms of the metric tensor is

$$\Gamma^{\alpha}_{\beta\gamma} = \frac{1}{2}g^{\alpha\nu}(g_{\nu\beta,\gamma} + g_{\nu\gamma,\beta} - g_{\beta\nu,\nu}) \tag{6.15}$$

and using the perturbed metric we find

$$\Gamma^{\alpha}_{\beta\gamma} = \Gamma^{\alpha\ (B)}_{\beta\gamma} + \delta\Gamma^{\alpha}_{\beta\gamma} \tag{6.16}$$

$$\delta\Gamma^{\alpha}_{\beta\gamma} = \frac{1}{2}g^{\mu\alpha}(h_{\alpha\beta;\gamma} + h_{\alpha\gamma;\beta} - h_{\beta\gamma;\alpha}) \tag{6.17}$$

where we denote ";" the covariant derivative with respect to the background metric.

Similarly we find the perturbation to the Ricci tensor:

$$R_{\alpha\beta} = R^{(B)}_{\alpha\beta} + \delta R_{\alpha\beta} \tag{6.18}$$

$$= \Gamma^{\gamma}_{\alpha\gamma,\beta} - \Gamma^{\gamma}_{\alpha\beta,\gamma} + \Gamma^{\mu}_{\alpha\gamma}\Gamma^{\gamma}_{\beta\mu} - \Gamma^{\gamma}_{\alpha\beta}\Gamma^{\mu}_{\gamma\mu} \tag{6.19}$$

$$\delta R_{\alpha\beta} = \delta\Gamma^{\gamma}_{\alpha\gamma;\beta} - \delta\Gamma^{\gamma}_{\alpha\beta;\gamma} \tag{6.20}$$

Then by substituting these equations into Einstein's equations in vaccum, $\delta R_{\alpha\beta} = 0$, we get a second order differential equation for $h_{\mu\nu}$. These equations are decomposed into spherical harmonics.

Two different kinds of perturbations can be examined. In the terminology of Regge and Wheeler, these are called *odd* perturbations which transform as $(-1)^l$ under space inversion, and *even* perturbations which transform as $(-1)^{l+1}$. Chandrasekhar(1983) [80] refers to them as *axial* perturbations which cause dragging of the inertial frames, and *polar* perturbations which are independent of the sign of $\phi$ and therefore do not induce rotation. The most general odd perturbation is given by Regge and Wheeler as

$$h_{\mu\nu} = \begin{bmatrix} 0 & 0 & \frac{-h_0^{(a)}(t,r)}{\sin\theta}\partial_\phi Y_{lm} & \frac{h_0^{(a)}(t,r)}{\sin\theta}\partial_\theta Y_{lm} \\ 0 & 0 & -\frac{h_1^{(a)}(t,r)}{\sin\theta}\partial_\phi Y_{lm} & \frac{h_1^{(a)}(t,r)}{\sin\theta}\partial_\theta Y_{lm} \\ Sym & Sym & -\frac{h_2(t,r)}{\sin\theta}X_{lm} & -h_2(t,r)W_{lm}\sin\theta \\ Sym & Sym & Sym & -h_2(t,r)X_{lm}\sin\theta \end{bmatrix} \tag{6.21}$$

Similarly, for even perturbations

$$h_{\mu\nu} = \begin{bmatrix} \left(1-\frac{2M}{r}\right)H_0(t,r)Y_{lm} & H_1(t,r)Y_{lm} & h_0^{(p)}(t,r)\partial_\theta Y_{lm} & h_0^{(p)}(t,r)\partial_\phi Y_{lm} \\ Sym & \left(1-\frac{2M}{r}\right)H_2(t,r)Y_{lm} & h_1^{(p)}(t,r)\partial_\theta Y_{lm} & h_1^{(p)}(t,r)\partial_\phi Y_{lm} \\ Sym & Sym & \begin{matrix} r^2[K(t,r) \\ +G(t,r)\partial_{\theta\theta}]Y_{lm} \end{matrix} & r^2G(t,r)X_{lm} \\ Sym & Sym & Sym & \begin{matrix} r^2\sin^2\theta[K(t,r)Y_{lm} \\ +G(t,r)(Y_{lm}-W_{lm})] \end{matrix} \end{bmatrix} \tag{6.22}$$

where

$$X_{lm} = 2(\partial_{\theta\phi}Y_{lm} - \partial_{\phi}cot\theta) \tag{6.23}$$

$$W_{lm} = \partial_{\theta\theta}Y_{lm} - \partial_{\theta}Y_{lm}cot\theta - \frac{1}{\sin^2\theta}\partial_{\phi\phi}Y_{lm} \tag{6.24}$$

The perturbations are simplified by the following three steps:

- Frequency analysis: Because the background metric, eq. (6.3), is time independent, we can assume that every component of the perturbation $h_{\mu\nu}$ will have a time dependence of the form $e^{-i\omega t}$ and consider perturbations of a particular frequency, $\omega$.
- Specialization to $m = 0$: Schwarzschild spacetime is spherically symmetric. For all values of $l$, $k$ and parity all values of $m$ will lead to the same radial equation, so Regge and Wheeler have specialized to $m = 0$ with the advantage that $\phi$ will completely disappear from the calculations.
- Gauge transformation: By an appropriate gauge transformation it is possible to impose additional simplifying conditions on the perturbations. Regge and Wheeler have chosen to eliminate those terms which contain the derivatives of highest order with respect to the angles.

The final simplified form for the odd perturbations is

$$h_{\mu\nu} = \begin{bmatrix} 0 & 0 & 0 & h_0(r) \\ 0 & 0 & 0 & h_1(r) \\ 0 & 0 & 0 & 0 \\ Sym & Sym & 0 & 0 \end{bmatrix} \times e^{-i\omega t}(\sin\theta\frac{\partial}{\partial\theta})P_l(\cos\theta) \tag{6.25}$$

and the even perturbations are similarly written as

$$h_{\mu\nu} = \begin{bmatrix} H_0(r)\left(1-\frac{2M}{r}\right) & H_1(r) & 0 & 0 \\ H_1(r) & H_2(r)\left(1-\frac{2M}{r}\right)^{-1} & 0 & 0 \\ 0 & 0 & r^2K & 0 \\ Sym & Sym & 0 & r^2K\sin^2\theta \end{bmatrix} \times e^{-i\omega t}P_l(\cos\theta) \tag{6.26}$$

The problem is now reduced to only two unknowns in the odd case and four unknowns in the even case. These expressions can be substituted into eqs. (6.17) and (6.20) to yield the desired Einstein equations. Whereas Regge and Wheeler must have spent considerable time doing this by hand, I have used GR Tensor, a computer software package for use in the computer algebra system MAPLE. The first step is to define $g^{(B)}_{\mu\nu}$ and $h_{\mu\nu}$, then to calculate the perturbed Christoffel symbols, then the perturbed Ricci tensor. Some simple operations such as *collect, simplify,* *expand* are required in order to find the most suitable form for the equations. Standard relations for the differentiation of spherical harmonics are also substituted into the equations.

For odd perturbations only three nontrivial Einstein equations are found. For even perturbations the Einstein equations give one algebraic condition, three first order differential equations and three second order differential equations.

Regge and Wheeler consider odd perturbations. The three non-trivial equations are

$$\delta R_{\theta\phi} = 0$$

$$\left(1-\frac{2M}{r}\right)^{-1} i\omega h_0 + \frac{d}{dr}\left(1-\frac{2M}{r}\right) h_1 = 0 \tag{6.27}$$

$$\delta R_{r\phi} = 0$$

$$\left(1-\frac{2M}{r}\right)^{-1} \omega \left(i\frac{dh_0}{dr} - \omega h_1 - 2\frac{h_0}{r}\right) + (l-1)(l+2)\frac{h_1}{r^2} = 0 \tag{6.28}$$

$$\delta R_{t\phi} = 0$$

$$\frac{d}{dr}\left(i\omega h_1 + \frac{dh_0}{dr}\right) + 2i\omega\frac{h_1}{r} + \left(1-\frac{2M}{r}\right)^{-1}\left(4m\frac{h_0}{r} - l(l+1)h_0\right)\frac{1}{r^2} = 0 \tag{6.29}$$

Using the definition

$$Q = r\left(1-\frac{2M}{r}\right) h_1 \tag{6.30}$$

and eliminating $h_0$ gives us the second order wave equation with potential

$$\partial_{tt}Q - \partial_{r_* r_*}Q + V(r)Q = 0 \tag{6.31}$$

where

$$V(r) = \left(1-\frac{2M}{r}\right)\left(\frac{l(l+1)}{r^2} - \frac{6M}{r^3}\right) \tag{6.32}$$

This is the potential for gravitational perturbations, but a general form of the potential may be written as

$$V(r) = \left(1-\frac{2M}{r}\right)\left(\frac{l(l+1)}{r^2} + \frac{2M(1-s^2)}{r^3}\right) \tag{6.33}$$

where $s$ is the spin-weight of the perturbing field, with $s = 2$ for gravitational waves, $s = 1$ for electromagnetic waves and $s = 0$ for scalar waves.

## 6.3 Green's Function Approach

We may solve the Regge-Wheeler equation in the frequency domain for given initial data using the Green's function method. We must find the Green's function $G(r_*, r'_*, t)$ which satisfies the equation

$$(\partial_{r_* r_*} - \partial_{tt} - V_l(r))\, G(r_*, r'_*, t) = \delta(t)\delta(r_* - r'_*) \tag{6.34}$$

where we impose the condition $G(r_*, r'_*, t) = 0$ for $t \leq 0$.

In order to find the Green's function we transform to the frequency domain and thus reduce eq. (6.34) to an ordinary differential equation. We follow Andersson [81] and use the transformation

$$F(G(r_*, \omega)) \equiv \hat{G}(r_*, r'_*, \omega) = \int_0^{+\infty} e^{i\omega t} G(r_*, r'_*, t)dt \tag{6.35}$$

which is well defined for $Im(\omega) \geq 0$. The Green's function in the frequency domain can now be expressed in terms of two linearly independent solutions to the homogeneous equation

$$\left[\frac{d^2}{dr_*^2} + \omega^2 - V(r)\right] \hat{\Phi}(r_*, \omega) = 0 \tag{6.36}$$

The forms of the solutions depend upon the boundary conditions. The first solution (at $r_* < r'_*$) corresponds to purely ingoing waves at the horizon

$$\hat{\Phi}^-(r_*, \omega) \sim \begin{cases} e^{-i\omega r_*} & r_* \rightarrow -\infty \\ A_{out}(\omega)e^{i\omega r_*} + A_{in}(\omega)e^{-i\omega r_*} & r_* \rightarrow \infty \end{cases} \tag{6.37}$$

The second solution at $(r_* > r'_*)$ corresponds to purely outgoing waves at infinity

$$\hat{\Phi}^+(r_*, \omega) \sim \begin{cases} B_{out}(\omega)e^{i\omega r_*} + B_{in}(\omega)e^{-i\omega r_*} & r_* \rightarrow -\infty \\ e^{i\omega r_*} & r_* \rightarrow \infty \end{cases} \tag{6.38}$$

Then the Green's function may be written as

$$\hat{G}(r_*, r'_*, \omega) = \frac{1}{W(\omega)} \begin{cases} \hat{\Phi}^-(r_*, \omega)\hat{\Phi}^+(r'_*, \omega) & r_* < r'_* \\ \hat{\Phi}^-(r'_*, \omega)\hat{\Phi}^+(r_*, \omega) & r_* > r'_* \end{cases} \tag{6.39}$$

where

$$W(\omega) = \hat{\Phi}^- \frac{d\hat{\Phi}^+}{dr_*} - \hat{\Phi}^+ \frac{d\hat{\Phi}^-}{dr_*} = 2i\omega A_{in}(\omega) \tag{6.40}$$

is the Wronskian of the two solutions. After finding $\hat{G}(r_*, r'_*, \omega)$ we can return to the time domain using the inverse transform

$$G(r_*, r'_*, t) = \frac{1}{2\pi} \int_{-\infty+ic}^{+\infty+ic} \hat{G}(r_*, r'_*, \omega) e^{-i\omega t} d\omega \tag{6.41}$$

Finally, the solution to the Regge-Wheeler equation is given by (see e.g. [82])

$$\hat{\Phi}(r_*, t) = \int_{-\infty}^{\infty} \left[\partial_t G(r_*, r'_*, t)\Phi(r'_*, 0) + \partial_t \Phi(r'_*, 0) G(r_*, r'_*, t)\right] dr'_* \tag{6.42}$$

By direct integration we can discover how some initial perturbation evolves in time but it does not give much insight into the physics behind the different features of the solution at different times. It is possible, however, to investigate the behaviour of the Greens function in different regions of the time domain using the method of analytic continuation and using the residue theorem.

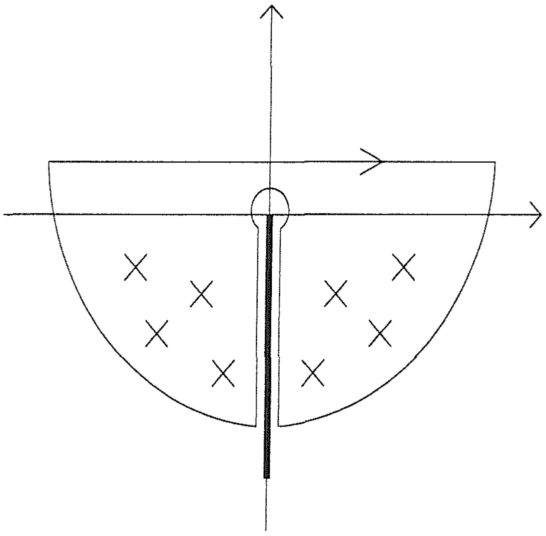

Figure 6.1: Analytic extension of the contour in the complex frequency plane. Crosses represent the singularities which are associated with the quasinormal modes. A branch cut, marked here by a bold line, is introduced along the negative imaginary axis in order to avoid including the point $\omega = 0$ in the integration.

When $A_{in}(\omega) = 0$, the Greens function $\hat{G}(r_*, r'_*, \omega)$ is singular and the two solutions, $\Phi^+$ and $\Phi^-$, are no longer linearly independent. From eq. (6.37) we can see that this corresponds to a solution with purely outgoing waves at spatial infinity and purely ingoing waves at the horizon. These are the quasinormal mode solutions whose characteristic frequencies all lie in the lower half of the complex $\omega$-plane. Near the quasinormal mode frequencies $(\omega_q)$ we can approximate $A_{in}$ by

$$A_{in}(\omega) \approx (\omega - \omega_q) \left. \frac{dA_{in}}{d\omega} \right|_{\omega=\omega_q} = (\omega - \omega_q)\alpha_q \tag{6.43}$$

Using eqs. (6.39), (6.40) and (6.43) we can approximate the frequency domain Green's function by

$$G(r_*, r'_*, \omega) \sim \frac{\hat{\Phi}^-(r_{*<}, \omega)\hat{\Phi}^+(r_{*>}, \omega)}{2\omega(\omega - \omega_q)\alpha_q} \tag{6.44}$$

where we have used the notation $r_{*<}$ for $min(r_*, r'_*)$ and $r_{*>}$ for $max(r_*, r'_*)$ . We extend our integration contour as illustrated in Fig. 6.1. There are some difficulties involved in this step due to the fact that the transformation in eq. (6.35) is defined only in the upper half of the $\omega$-plane (see [49] for discussion) but we assume here that such an analytic continuation is possible. A branch cut is introduced along the negative imaginary axis to avoid including the point $\omega = 0$ in the integration. Using the new contour, the Green's function may be written as three terms

$$G(r_*, r'_*, t) = G_f(r_*, r'_*, t) + G_q(r_*, r'_*, t) + G_b(r_*, r'_*, t) \tag{6.45}$$

$G_q$ is the sum of the residues at the poles of $G(r_*, r'_*, \omega)$, corresponding to the quasi-normal ringing, $G_b$ is the integral of $G(r_*, r'_*, \omega)$ around the branch cut, and $G_f$ is the integral along the large quarter circles. The branch cut contribution is associated with the late time power law decay of the solution [57] and the large arcs which close the contour are associated with the high-frequency response. $G_f$ reduces to the free-space Green's function in the limit of zero mass for the black hole.

It is possible to calculate the quasi-normal mode frequencies and this has been done by several accurate methods, e.g. [48], [49]. Finding the quasinormal mode contribution to the Green's function is a lengthy process [? ]. Andersson has used an asymptotic approximation to arrive at a simplified formula for the mode excitations [81][49]. I will not present the full details of the Green's function calculations here but I will use the results of Leaver and Andersson for the quasi-normal mode frequencies for comparison with the results of time evolutions I have carried out as explained in the next section.

The late time decay of the solution was studied by Price [47]. He showed that the field decays with a power law tail at late times according to the formula

$$\Psi(r, t) \sim t^{-(2l+P+1)} \tag{6.46}$$

where $P = 1$ for static initial data and $P = 2$ otherwise. This was confirmed by Gundlach et al [62] using linear and non-linear evolutions.

## 6.4 Numerical Evolution

It is fairly straightforward to use our basic numerical techniques from the previous section to evolve the Regge Wheeler equation. We set up a numerical grid in the radial coordinate $r_*$.

### *6.4.1 Calculating the Potential*

One immediate obstacle is that the potential is a function of $r$ which is not a simple analytic function of $r_*$ (eq. (6.11)), i.e. the equation

$$r_* = r + 2Mln\left(\frac{r}{2M} - 1\right) \tag{6.47}$$

is not invertible. We cannot find an analytic expression for $V(r_*)$ and therefore must use a numerical method for calculating the potential at each gridpoint. For an initial value we pick some value of $r$ and calculate $r_*$ at that point using eq.(6.47). Numerical integration is carried out using the fourth order Runge-Kutta method described in section (4.2). The convergence of this method has been tested by outputing results for double, quadruple etc. grid resolutions. The order of convergence was calculated in MAPLE using the function *fit[leastsquare]* in the stats package. The result is given as 3.939899563, very close to the expected second order value of 4.

The form of the Regge-Wheeler potential in $r$ and $r_*$ coordinates is shown in Figs. 6.2 and 6.3.

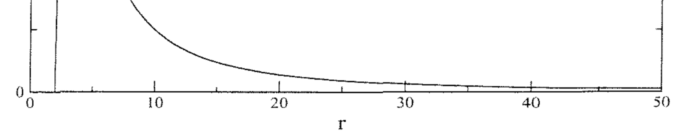

Figure 6.2: The Regge-Wheeler potential for scalar waves as a function of $r$ .

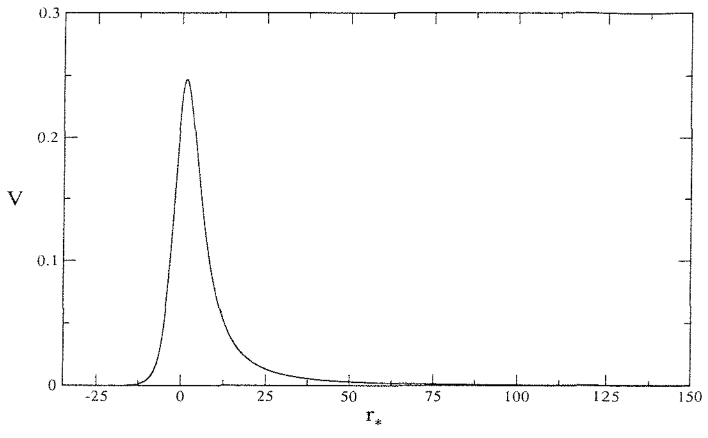

Figure 6.3: The Regge-Wheeler potential for scalar waves as a function of $r_*$

### *6.4.2 Cauchy Evolution*

Following the same scheme given in section 5.1, the Regge-Wheeler equation is written in finite difference form as

$$p_k^{n+1} = 2p_k^n - p_k^{n-1} + (p_{k+1}^n - 2p_k^n + p_{k-1}^n)\left(\frac{\Delta t}{\Delta x}\right)^2 - V(k)p_k^n\Delta t^2 \tag{6.48}$$

As initial data we again consider a Gaussian pulse which is travelling to the left. This represents the physical situation of a small perturbation travelling inwards towards a black hole.

The output from this evolution is shown in Fig. 6.4. The pulse becomes distorted as it travels inward. On reaching the potential peak the majority of the pulse is reflected, but some passes through the potential and falls inward further towards the horizon. Fig. 6.5 shows how the log of the solution varies with time at a fixed point (in this case $r_* \approx 30$). Here we can clearly see the initial reflection, the quasi-normal ringing and the late time tail. The modes can be seen more clearly in Fig. 6.6.

One way to test our results is to measure the frequency and damping of the quasi normal modes and the gradient of the late time tail. These calculations can then be compared to known analytic approximations. The results are shown for gravitational perturbations with $l = 2$ and the least damped quasi normal modes in this case have complex frequency [49][57]

$$\omega \approx 0.376 - 0.0899i \tag{6.49}$$

thus we would expect a half-period of

$$\frac{P}{2} = \frac{\pi}{Re(\omega)} \approx 8.35 \tag{6.50}$$

By measurement from Fig. 6.6 we get the value 8.3 which compares favourably. The gradient is measured as $-0.083$ which is close to the expected value of $-0.09$. The time behaviour of the tail at future null infinity is given by $t^{-(2l+3)}$ [62] so we would expect here to find $t^{-7}$. The measured fall off is 7.7. It is possible that we have not evolved to late enough times to get a good estimation of the power law behaviour. Another explanation could be that we are seeing the effect of modes of higher multipoles. The next higher multipole has fall off $t^{-9}$.

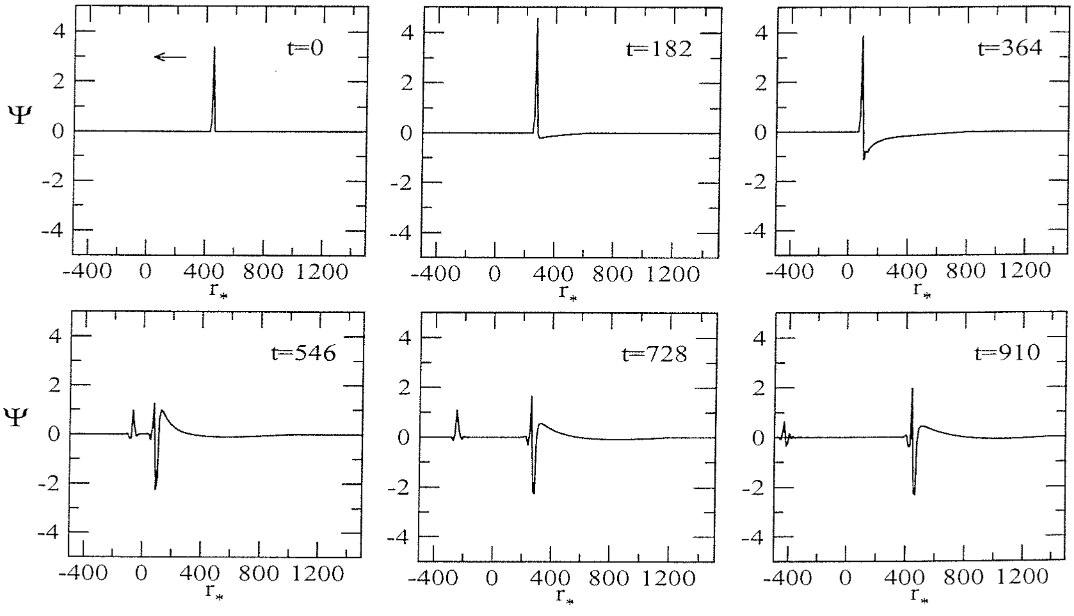

Figure 6.4: Cauchy evolution of the Regge-Wheeler equation. On reaching the potential peak the majority of the pulse is reflected, but some passes through the potential and falls inward further towards the horizon.

The convergence for this code is shown in Fig. 6.7.

Gundlach et al [62] have poi nted out that using this kind of finite differencing leads to a ghost potential which can affect the magnitude of the late time tail. Here we do not concern ourselves too much about this as a precise Cauchy evolution of the Regge-Wheeler equation is not our ultimate goal. This section is mainly an

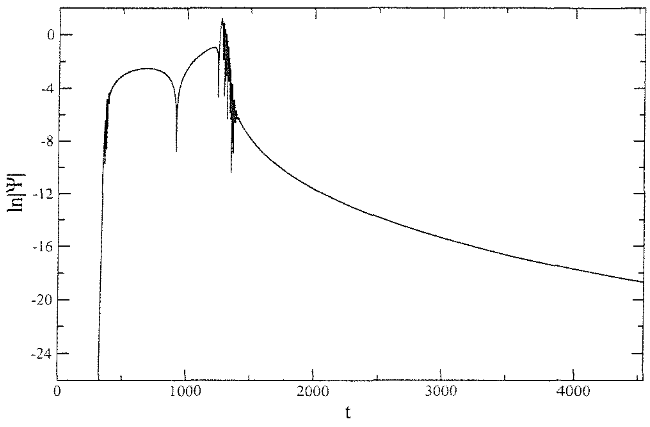

Figure 6.5: Log of the solution at one gridpoint, from the Cauchy evolution of the Regge-Wheeler equation. The quasinormal modes can be seen, followed by the power-law tail.

exercise in evolving different kinds of initial value problems for the wave equation in Schwarzchild spacetime.

Although the Cauchy evolution gives good results, there are problems due to boundary reflections which contaminate the solution at late times. This is shown clearly in Fig. 6.8. This is a general disadvantage of Cauchy evolution and in an attempt to avoid this problem we move to a characteristic formulation.

### *6.4.3 Double-Null Evolution*

The Regge-Wheeler equation can be evolved on characteristics. We have used double-null coordinates, $u$ and $v$ where

$$u = t - r_* \tag{6.51}$$

$$v = t + r_* \tag{6.52}$$

giving

$$4\Psi_{uv} + V(r)\Psi = 0 \tag{6.53}$$

This is finite differenced using the scheme described in section 5.2 for the one dimensional wave equation. The Regge-Wheeler equation becomes

$$p_{k+1}^{n+1} = -p_k^n + p_{k+1}^n + p_k^{n+1} - 0.25\Delta u \Delta v p_{k+\frac{1}{2}}^{n+\frac{1}{2}} V_{k+\frac{1}{2}}^{n+\frac{1}{2}} \tag{6.54}$$

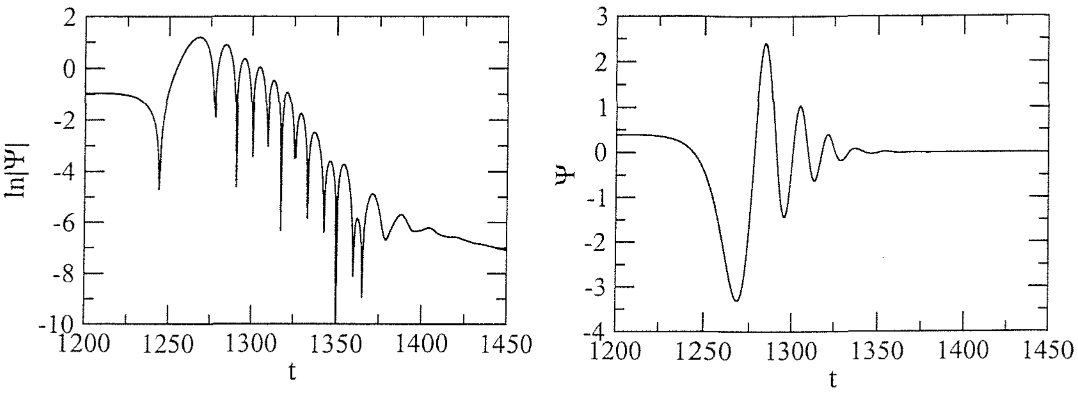

Figure 6.6: The quasi normal modes in Cauchy evolution. The picture on the left shows the behaviour of the log of the solution at one gridpoint and the picture on the right shows the behaviour of the solution itself at the same gridpoint.

We also need to write the potential, $V$, on our $u$ and $v$ slices. For any value of $u$ and $v$ we can find the corresponding $r_* = (v - u)/2$. $r$ is approximated by numerical integration and substituted into eq. (6.33) to find $V(u, v)$.

The results for this evolution scheme, output on constant $u$ slices, are shown in Fig. 6.9. Surfaces of increasing $u$ follow the part of the initial perturbation which travels unimpeded towards the horizon along surfaces of constant $v$. Any reflections from the potential travel along the positive $u$ direction and are thus immediately integrated off the grid. The log of the solution at constant $r_*$ is shown as a function of time in Fig. 6.10. The quasinormal modes are shown in Fig. 6.11 and the power law tail can be seen in fig. 6.12

As in the case of the Cauchy evolution, we test our results by comparison with analytic approximation. The half period of the quasi normal modes is measured as 8.29 and the damping is measured at $-0.081$. The measured tail is $t^{-7.5}$ which compares quite well with the expected $t^{-7}$.

This scheme leads to a very clean evolution and gives good results. By extending the domain of integration we can get better approximations for the late time tail at null infinity, however this could be a computationally expensive procedure. One of the benefits of characteristic coordinates is that we can compactify for solutions at future null infinity. This would be achieved in the double-null case by compactification of the $v$ coordinate. For solutions at the horizon we could compactify in the $u$ coordinate. This involves a compactification in time and space. Although it is not a problem here, in more general cases the double null formulation could

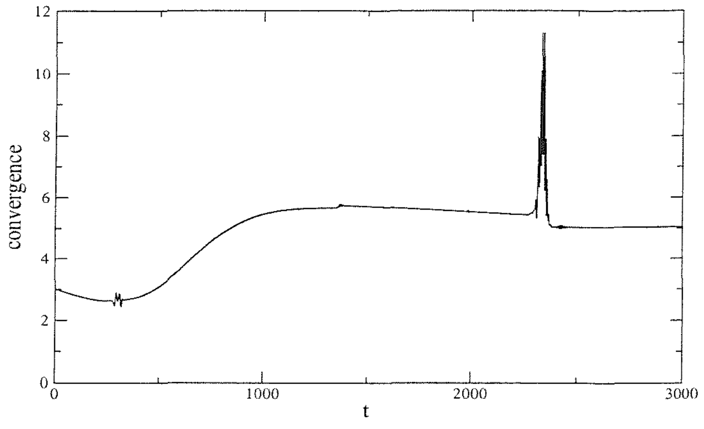

Figure 6.7: Results of the convergence test for the Cauchy evolution of the Regge-Wheeler equation. The sharp peak appears when data hits the boundary.

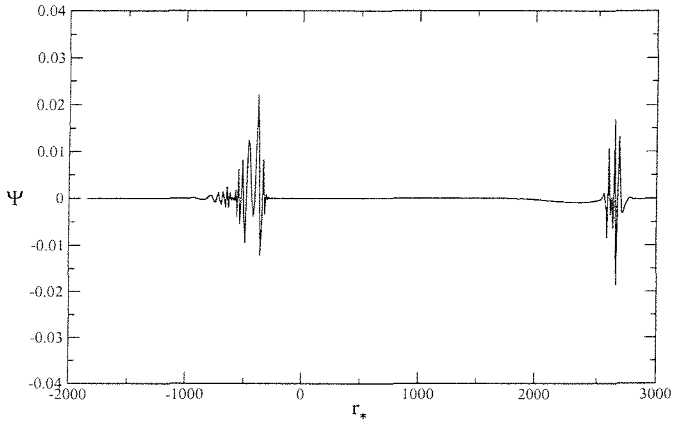

Figure 6.8: Boundary reflections in the Cauchy evolution. This is a snapshot taken at late times, after all the radiation should have left the grid.

lead to some difficulties in black hole spacetimes as outgoing rays may cross near the horizon and ingoing rays may cross at large radius. This would lead to caustic formation, which our simple numerical treatments cannot deal with.

The code is second order convergent as can be seen from Fig. 6.13.

### *6.4.4 Null-Timelike Evolution*

The Regge-Wheeler equation can be written in retarded null-timelike coordinates, $r_*$, $u = t - r_*$

$$2\Psi_{ur_*} - \Psi_{r_*r_*} + V(r_*)\Psi = 0 \tag{6.55}$$

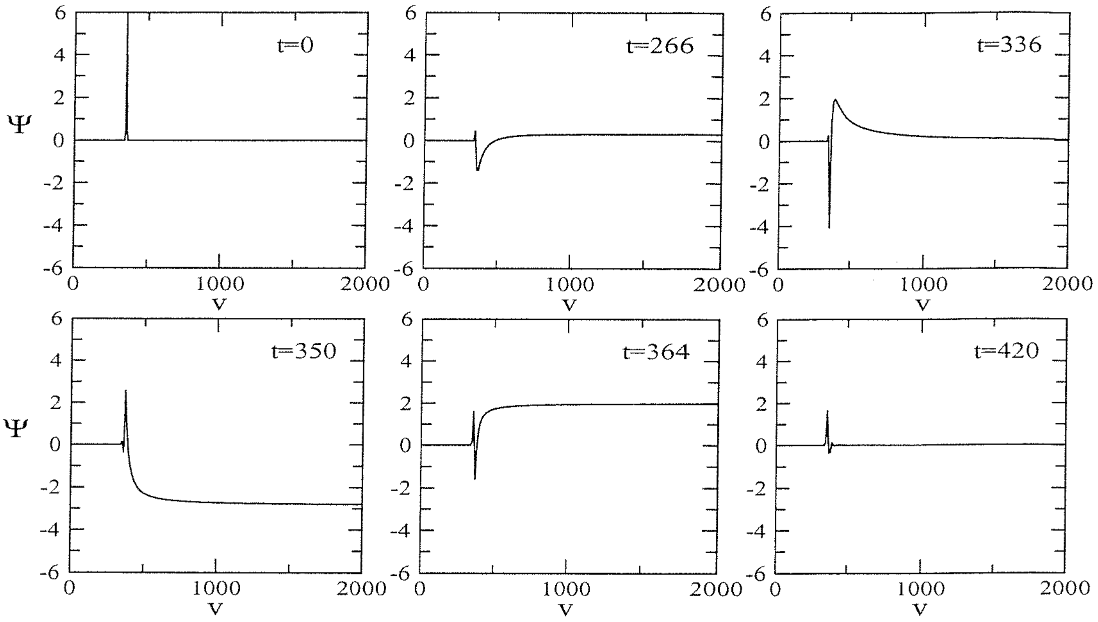

Figure 6.9: Double null evolution of Regge-Wheeler equation on constant u slices. The reflections from the potential travel straight off the grid and a appear as straight lines here.

The derivatives are written in finite difference form using the second order scheme described in section 5.3, giving the second order finite difference equation

$$p_k^{n+1} = -\frac{1}{1-A}(-p_{k-1}^{n+1} - p_k^n + p_{k-1}^n) + \frac{A}{1-A}(-2p_{k-1}^{n+1} + p_{k-2}^{n+1} + p_{k+1}^n - 2p_k^n + p_{k-1}^n) \tag{6.56}$$

$$-\frac{\Delta u \Delta r_*}{2(1-A)} p_{k-\frac{1}{2}}^{n+\frac{1}{2}} V_{k-\frac{1}{2}}^{n+\frac{1}{2}} \tag{6.57}$$

where $A = \dfrac{\Delta u}{4\Delta r_*}$.

An ingoing wave boundary condition is imposed at the inner boundary. This, along with a description of the treatment of the first gridpoint near the inner boundary, can be found in section 5.3. The outer boundary is treated using a second order one-sided derivative.

As initial data we consider a Gaussian pulse situated outside the potential peak. This represents a perturbation moving in the negative radial direction. The output from this evolution is shown in Fig. 6.14 as the time variation of the solution at

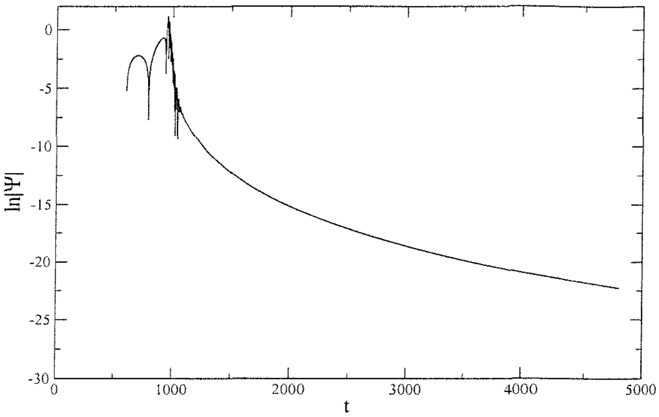

Figure 6.10: Log of the solution at one gridpoint, from the double-null evolution of the Regge-Wheeler equation. The quasinormal modes can be seen, followed by the power-law tail.

$r_* = 30$. It is apparent from this figure that there are serious boundary condition problems. There are reflections from both the inner and outer boundaries.

In order to solve the problems with the boundaries we can compactify our radial coordinate. We choose to compactify in both directions in order to include both future null infinity and the black hole horizon on our numerical grid. It is essential however that we have enough gridpoints near the potential peak in order to resolve the potential features here and we also require good resolution near the initial data. We do not worry about the late time resolution near the horizon for now but we will return to that problem shortly. We use the compactified radial coordinate

$$x = \tan^{-1}(fr_*) \tag{6.58}$$

The constant, $f$, determines the gradient of the function $x$. By choosing a small value for $f$ we can compactify far away and also very near to the horizon, whilst leaving good resolution in the region near the initial data and potential. Fig. 6.15 plots $x$ as a function of $r_*$ for $f = 0.0017$.

Written in terms of $x$ and $u$ the Regge-Wheeler equation is

$$2\gamma\Psi_{ux} - \gamma^2\Psi_{xx} + 2\gamma^2 \tan x \Psi_x + V\Psi = 0 \tag{6.59}$$

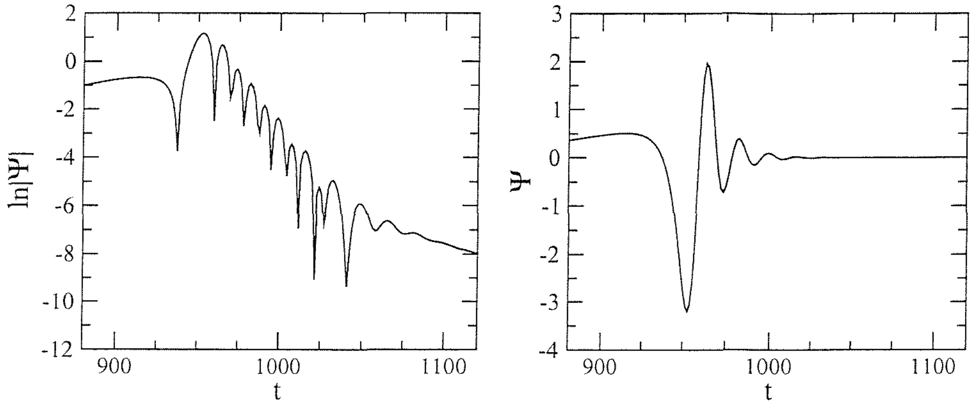

Figure 6.11: The quasi normal modes in the double-null evolution of the Regge-Wheeler equation. The picture on the left shows the behaviour of the log of the solution at one gridpoint and the picture on the right shows the behaviour of the solution itself at the same gridpoint.

which is written in finite difference form as

$$\begin{aligned} p_k^{n+1} = &- \frac{2\gamma}{\Delta u \Delta x \beta}\left(-p_{k-1}^{n+1} - p_k^n + p_{k-1}^n\right) \\ &+ \frac{\gamma^2}{2\Delta x^2 \beta}\left(-2p_{k-1}^{n+1} + p_{k-2}^{n+1} + p_{k+1}^n - 2p_k^n + p_{k-1}^n\right) \\ &- \frac{\gamma^2 \tan x}{\Delta x \beta}\left(-p_{k-1}^{n+1} + p_k^n - p_{k-1}^n\right) - \frac{1}{\beta} V_{k-\frac{1}{2}} p_{k-\frac{1}{2}}^{n+\frac{1}{2}} \end{aligned} \qquad (6.60)$$

where $\gamma = f/(1 + \tan^2 x)$ and

$$\beta = \frac{2\gamma}{\Delta u \Delta x} - \frac{\gamma^2}{2\Delta x^2} + \frac{\gamma^2 \tan x}{\Delta x} \qquad (6.61)$$

To calculate the value of the potential for very large positive values of $x$ we choose a nearby value of $r$ which is approximated by $r = r_*$, calculate the actual value of $r_*$ at this point and then integrate to the required position. This solves the problem of integrating over huge distances. For large negative values of $r_*$ I integrate from $r = 2.001$, although it may be more accurate, and efficient, to use some approximation for the potential near the horizon.

The results are shown on constant $u$ surfaces in Fig. 6.16. The outgoing radiation integrates cleanly off the grid and the part of the initial perturbation which passes through the potential barrier travels inward towards the horizon. Due to the fact that this part is so small, it cannot be seen in Fig. 6.16, but the late time behaviour can be seen in Fig. 6.17 in which the scale is magnified. As expected,

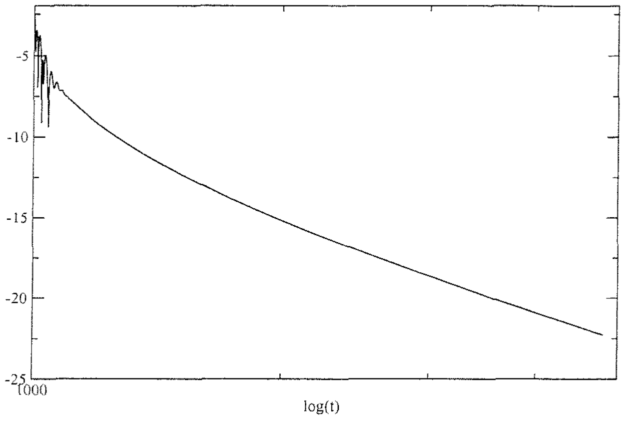

Figure 6.12: Log log plot of the solution at constant $r_*$ as a function of time for the double null evolution of the Regge-Wheeler equation. The data approaches a straight line at late times, indicating a power-law solution.

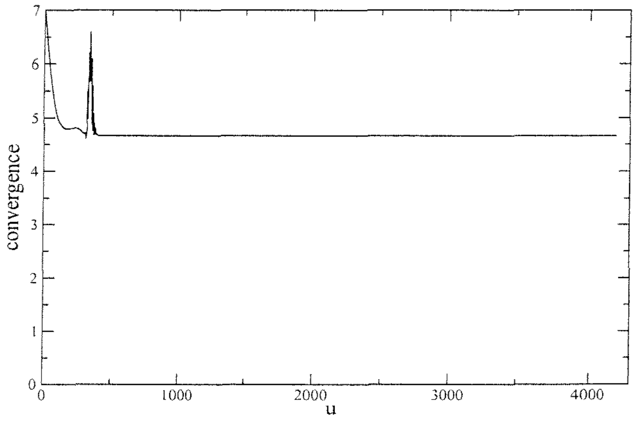

Figure 6.13: Second order convergence for double-null evolution

the lack of resolution near the horizon causes problems at late times and spoils the evolution. In order to avoid this problem we would like to match to an ingoing characteristic evolution. This is described in the next section.

### *6.4.5 Characteristic-Characteristic Matching (c2m)*

We match two characteristic codes, one ingoing and one outgoing. This is illustrated in Fig. 6.18. This solves the problem of having to impose boundary conditions at the inner and outer boundaries.

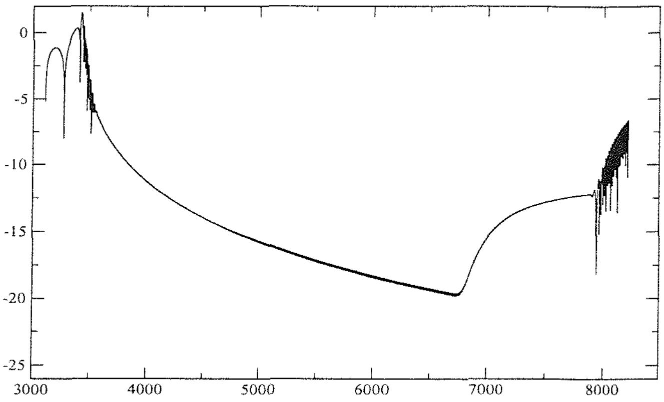

Figure 6.14: Log output from null-timelike evolution of Regge-Wheeler equation. The boundary reflections can be seen clearly. In order to avoid these reflections we will use a compactified radial coordinate.

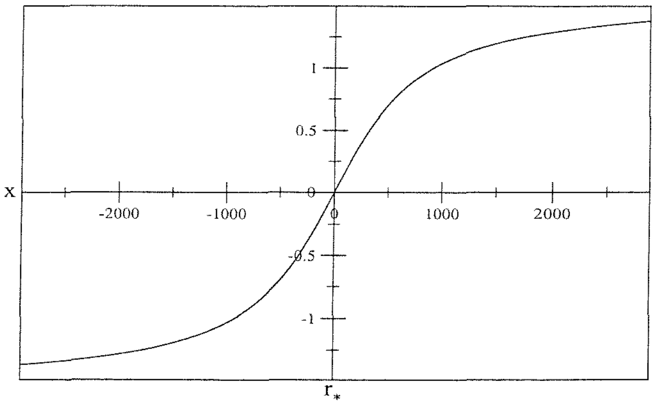

Figure 6.15: The compactified radial coordinate $x$ plotted as a function of $r_*$ for $f = 0.0017$, see eq. (6.58)

The Regge Wheeler equation written in ingoing null-timelike coordinates ($v = t + r_*, r_*$) is

$$2\Psi_{vr_*} + \Psi_{r_*r_*} - V\Psi = 0 \tag{6.62}$$

We compactify using the coordinate $x = \tan^{-1}(fr_*)$ giving

$$2\gamma\Psi_{vx} + \gamma^2\Psi_{xx} - 2\gamma^2 \tan x\Psi_x - V\Psi = 0 \tag{6.63}$$

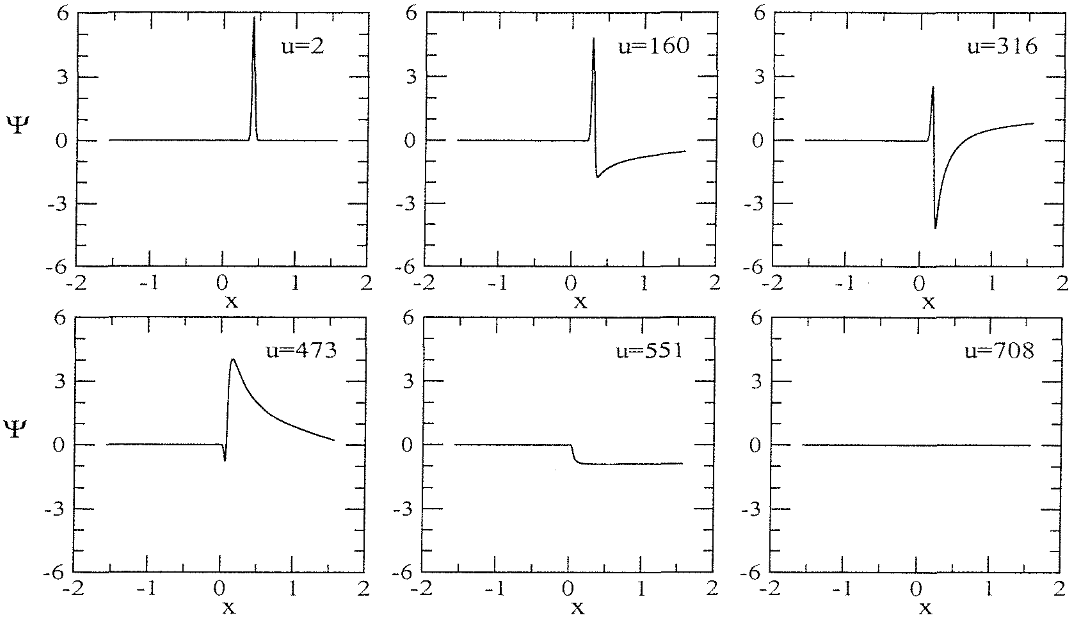

Figure 6.16: Retarded null-timelike evolution of Regge-Wheeler equation with the radial coordinate compactified. The initial pulse hits the potential and the reflected radiation passes cleanly off the grid.

and, finite differencing in the same way as we have done for outgoing characteristics, we get

$$
\begin{aligned}
p_k^{n+1} = & -\frac{2\gamma}{\Delta u \Delta x \beta}\left(-\Phi_{k-1}^{n+1} - \Phi_k^n + \Phi_{k-1}^n\right) \\
& - \frac{\gamma^2}{2\Delta x^2 \beta}\left(-2\Phi_{k-1}^{n+1} + \Phi_{k-2}^{n+1} + \Phi_{k+1}^n - 2\Phi_k^n + \Phi_{k-1}^n\right) \\
& + \frac{\gamma^2 \tan x}{\Delta x \beta}\left(-\Phi_{k-1}^{n+1} + \Phi_k^n - \Phi_{k-1}^n\right) + \frac{1}{\beta} V_{k-\frac{1}{2}} \Phi_{k-\frac{1}{2}}^{n+\frac{1}{2}}
\end{aligned}
\tag{6.64}
$$

where $k$ increases in the direction of the horizon.

To update the solution at the matching boundary we use a slightly modified version of our double null scheme described in section 5.2. This is illustrated in Fig. 6.18. We know the solution at all points on $u^n$ and $v^n$ and we require the solution at point $S$. The intersection of $u^{n+1}$ and $v^n$, is marked $P$. We calculate the value of $x = x^v$ at this point by first calculating the value of $r_*$ here

$$
r_*^v = \frac{v^n - u^{n+1}}{2} \tag{6.65}
$$

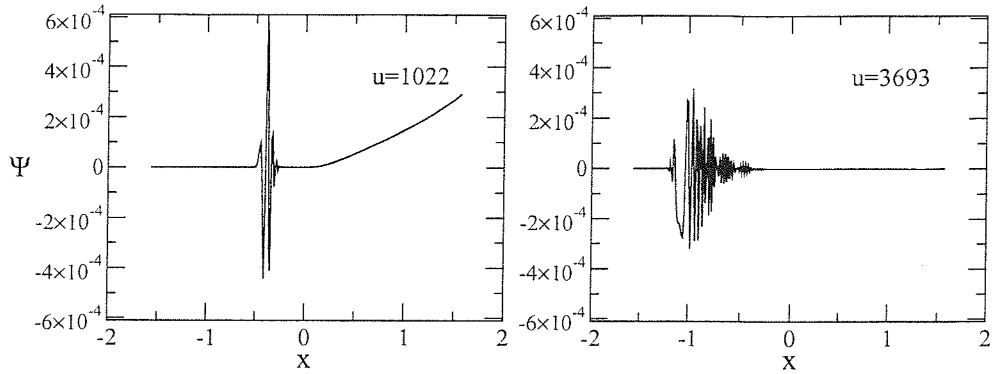

Figure 6.17: Late time behaviour on a u slice for the compactified retarded null timelike evolution of Regge-Wheeler equation. Compactification near the horizon causes resolution problems for the ingoing quasi normal modes. This could be solved by matching to an evolution ingoing null hypersurface before the resolution breaks down.

$x^v$ is then given by

$$x^v = \tan^{-1}(ar_*^v) \tag{6.66}$$

The solution is obtained at this point by interpolation of the solution at $v^n_{k_m}$, $v^n_{k_m-1}$, and $v^n_{k_m-2}$ as described in section 5.4. By an analogous procedure we can interpolate for the solution at the intersection of $v^{n+1}$ and $u^n$, marked $Q$. We now have four points, including the previous boundary point $R$, of a double null cell and we can use eq. (6.54) to update the solution at the matching boundary, point $S$.

The results are shown in Fig. 6.19. Fig. 6.21 shows the late time behaviour for this evolution and we can see the field decay. Even at this scale, where we have zoomed in from Fig. 6.19 by a factor of $10^7$ we do not see reflections or noise. Of course this code is not perfect and if we zoom in a few more factors of ten we will see some problems.

The quasi normal mode output at future null infinity is shown in Fig. 6.20 and Fig. 6.22 shows the power law behaviour of the late time tail. The half-period of the modes is measured as 8.3 and the damping is measured as $-0.089$ which are both in good agreement with the analytic approximations. The late time power law is measured as $u^{4.6}$ which is not in good agreement with the analytically obtained $u^4$ law. It is possible that we have not evolved to late enough times to properly measure the late time tail, or that we are seeing some mixing of higher order modes.

This code is second order convergent, as shown in Fig. 6.23.

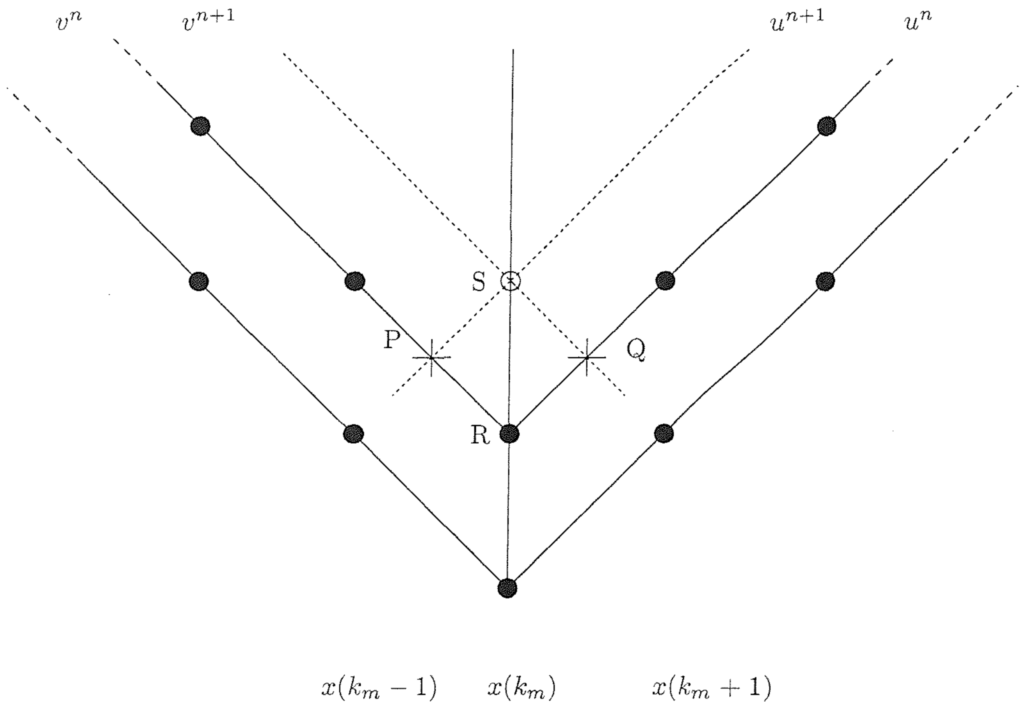

Figure 6.18: Calculating the solution at the matching bounday in the c2m evolution. We require the solution at point $S$. We calculate the value of $x = x^v$ at the point $P$ and calculate the solution at this point by interpolation of the solution at $v^n_{k_m}$, $v^n_{k_m-1}$, and $v^n_{k_m-2}$. We similarly interpolate for the solution at the point $Q$. The four points, $S$, $P$, $Q$ and $R$, form a double-null cell and we can use eq. (6.54) to update the solution at the matching point, $S$.

## 6.5 Chapter Summary

In this chapter I have evolved the Regge-Wheeler equation as a Cauchy, a double-null and a null-timelike initial value problem. In the null-timelike evolution I have compactified the radial coordinate and matched ingoing to outgoing evolutions and this has proven to be a very effective method for a good, clean evolution with second order convergence. The Regge-Wheeler equation has been a useful toy-problem, introducing aspects of black hole spacetimes which will carry over to later chapters where I deal with Kerr and Kerr-de Sitter spacetimes.

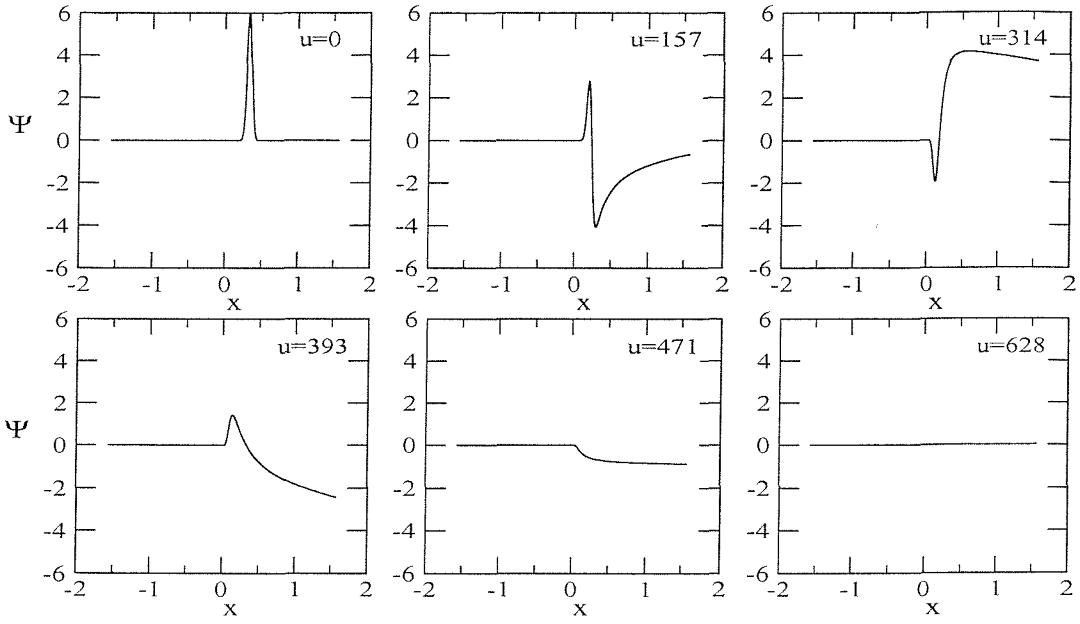

Figure 6.19: Results of the compactified c2m evolution of the Regge-Wheeler equation displayed on $u = const$ slices. This looks very similar to Fig. 6.16 but the difference is seen when the solution is magnified at late times.

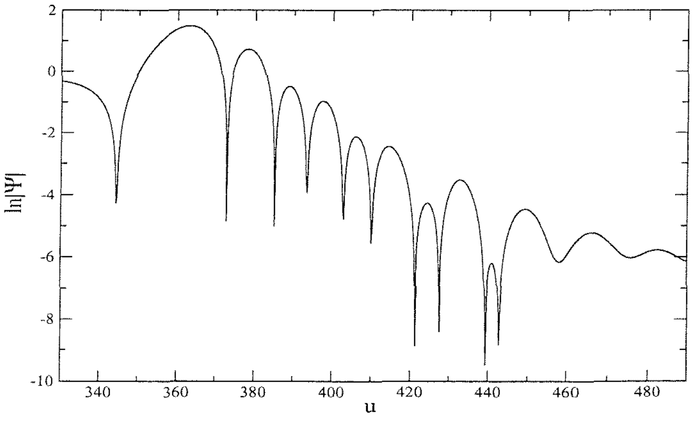

Figure 6.20: The quasi normal modes at future null infinity from the compactified c2m evolution of the Regge-Wheeler equation.

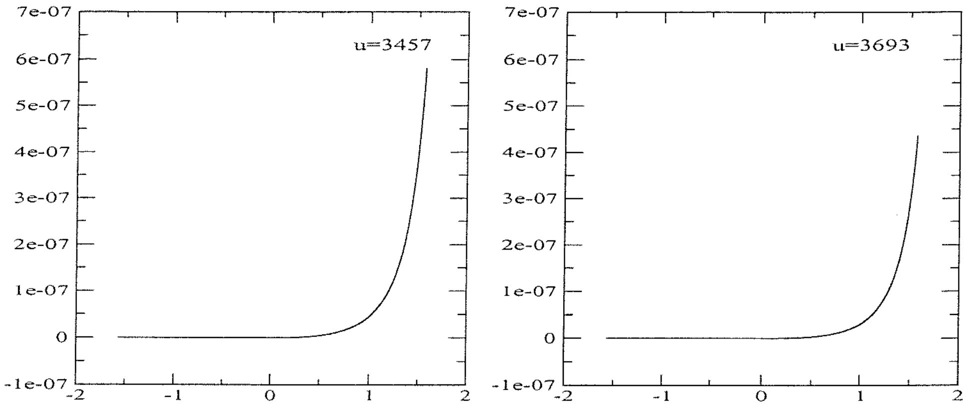

Figure 6.21: Late time behaviour on constant $u$ slices. Here we have magnified the $y$-axis to show that the problems seen in Fig. 6.17 are no longer present.

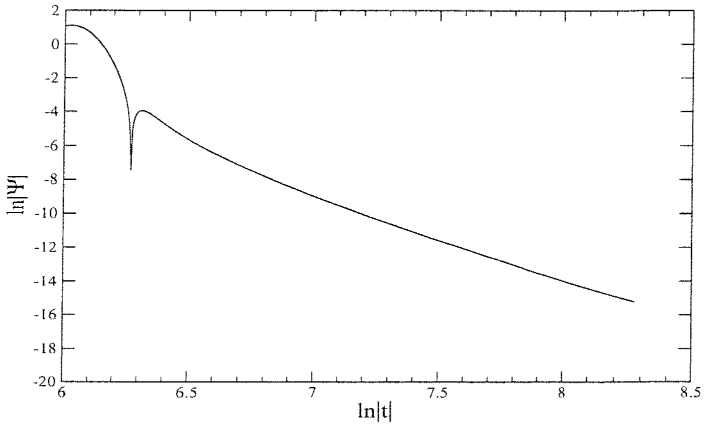

Figure 6.22: Log-log plot of compactified c2m evolution of Regge-Wheeler equation at future null infinity, showing late time power law tail.

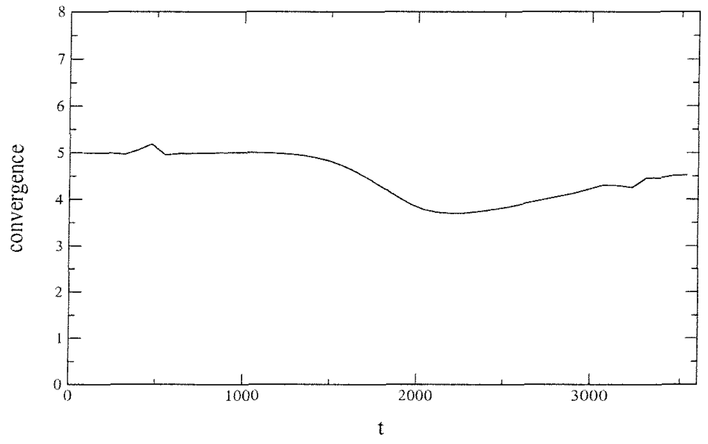

Figure 6.23: Second order convergence for the c2m code

# Chapter 7

# The Axisymmetric Wave Equation

In this chapter I extend the work of previous chapters to two-dimensional space. As a toy-problem I consider the wave equation in spherical polar coordinates. Assuming axisymmetry we can write a two-dimensional equation in $(t, r, \theta)$ or $(u, r, \theta)$. The resulting equations are similar to the one-dimensional equation with a potential. Assuming a reflective boundary at $r = a$ we can calculate the resulting modes which are scattered. The analytic derivation for the frequency of these modes was carried out in [85] and is reproduced here. I use these analytic results to test the numerical time evolutions which are also described in this chapter. I have chosen this toy-problem because the equations are similar to the equations governing perturbations in Kerr spacetime, enabling me to test the numerical schemes which I will use in the next chapter.

## 7.1 Calculating the Mode Frequency

The wave equation in spherical polar coordinates is

$$\begin{aligned}\Psi_{tt} - \frac{1}{r^2}\left(r^2\Psi_r\right)_r - \frac{1}{r^2\sin\theta}\left(\sin\theta\,\Psi_\theta\right)_\theta \\ -\frac{1}{r^2\sin^2\theta}\Psi_{\phi\phi} = 0\end{aligned} \tag{7.1}$$

In order to find a general solution we use the Fourier transform:

$$\Psi(\mathbf{x}, \omega) = \int_{-\infty}^{\infty} \Psi(\mathbf{x}, t) e^{i\omega t} dt \tag{7.2}$$

with each Fourier component satisfying the Helmholtz eq.

$$(\nabla^2 + \omega^2)\Psi(\mathbf{x}, \omega) = 0 \tag{7.3}$$

We can separate the variables using

$$\Psi(r,\theta,\phi) = R(r)\Theta(\theta)\Phi(\phi) \tag{7.4}$$

substitute into eq. (7.3) and divide by $R\Theta\Phi$ to get

$$\frac{1}{Rr^2}\frac{d}{dr}\left(r^2\frac{dR}{dr}\right) + \frac{1}{\Theta r^2 \sin\theta}\frac{d}{d\theta}\left(\sin\theta\frac{d\Theta}{d\theta}\right) + \frac{1}{\Phi r^2\sin^2\theta}\left(\frac{d^2\Phi}{d\phi^2}\right) = -\omega^2 \tag{7.5}$$

If we multiply by $r^2\sin^2\theta$ and rearrange we find

$$\frac{1}{\Phi}\left(\frac{d^2\Phi}{d\phi^2}\right) = r^2\sin^2\theta\left(-\omega^2 - \frac{1}{Rr^2}\frac{d}{dr}\left(r^2\frac{dR}{dr}\right) - \frac{1}{\Theta r^2\sin\theta\, d\theta}\frac{d}{d\theta}\left(\sin\theta\frac{d\Theta}{d\theta}\right)\right) \tag{7.6}$$

Since the left side of this equation depends only on $\phi$ and the right side depends only on $r$ and $\theta$ we can equate each side to a constant

$$\frac{1}{\Phi}\left(\frac{d^2\Phi}{d\phi^2}\right) = -m^2 \tag{7.7}$$

and

$$\frac{1}{Rr^2}\frac{d}{dr}\left(r^2\frac{dR}{dr}\right) + \frac{1}{\Theta r^2\sin\theta}\frac{d}{d\theta}\left(\sin\theta\frac{d\Theta}{d\theta}\right) + \omega^2 = \frac{m^2}{r^2\sin^2\theta} \tag{7.8}$$

or, separating variables again in the last eq.

$$\frac{1}{R}\frac{d}{dr}\left(r^2\frac{dR}{dr}\right) + r^2\omega^2 = -\frac{1}{\Theta\sin\theta}\frac{d}{d\theta}\left(\sin\theta\frac{d\Theta}{d\theta}\right) + \frac{m^2}{\sin^2\theta} \tag{7.9}$$

leading to two separate eqs. for $r$ and $\theta$

$$\frac{1}{\sin\theta}\frac{d}{d\theta}\left(\sin\theta\frac{d\Theta}{d\theta}\right) - \frac{m^2}{\sin^2\theta}\Theta + l(l+1)\Theta = 0 \tag{7.10}$$

$$\frac{1}{r^2}\frac{d}{dr}\left(r^2\frac{dR}{dr}\right) + \omega^2 R - \frac{l(l+1)R}{r^2} = 0 \tag{7.11}$$

Eq. (7.10) is the associated Legendre equation with solutions $P_l^m(\cos\theta)$, the associated Legendre functions. Solutions to eq. (7.7) are of the form $e^{\pm im\phi}$. Combining these two solutions gives the spherical harmonics

$$Y_l^m(\theta,\phi) \propto P_l^m(\cos\theta)e^{im\phi} \tag{7.12}$$

and the solution may be represented as

$$\Psi(\mathbf{x},\omega) = \sum_{l,m} f_{lm}(r,w)\, Y_{lm}(\theta,\phi) \tag{7.13}$$

Eq. (7.11) has solutions which are spherical Bessel functions or Hankel functions [86]. Substituting $R(r) = r^{-\frac{1}{2}}u_l(r)$ we get

$$\left(\frac{d^2}{dr^2} + \frac{1}{r}\frac{d}{dr} + \omega^2 - \frac{(l+\frac{1}{2})^2}{r^2}\right) u_l(r) = 0 \tag{7.14}$$

which is the Bessel eqn. with $\nu = l + \frac{1}{2}$. The most general solution of (7.3) in spherical polar coordinates is given by

$$\Psi(\mathbf{x},\omega) = \sum_{l,m} [A^{(1)}_{lm} h^{(1)}_l(\omega r) + A^{(2)}_{lm} h^{(2)}_l(\omega r)]\, Y_{lm}(\theta,\phi) \tag{7.15}$$

where $h_l$ are the spherical Hankel functions. The actual solution will depend on the initial data and boundary conditions.

To find the solution for some given initial data at $t = 0$ we take the Laplace transform of our wave equation but substitute $s = -i\omega$ so that we are actually using a one-sided Fourier transform. This is preferable because it enables us to work directly in the frequency plane.

$$\mathcal{L}[\nabla^2\Psi - \ddot{\Psi}] = \mathcal{L}[\nabla^2\Psi] - \mathcal{L}[\ddot{\Psi}] \tag{7.16}$$

where

$$\begin{aligned}
\mathcal{L}[\ddot{\Psi}] =& \int_0^\infty \ddot{\Psi} e^{i\omega t} dt \\
=& [e^{i\omega t}\dot{\Psi}]_0^\infty - i\omega \int_0^\infty \dot{\Psi} e^{i\omega t} dt \\
=& [e^{i\omega t}\dot{\Psi}]_0^\infty - i\omega \left( [e^{i\omega t}\Psi]_0^\infty - i\omega \int_0^\infty \Psi e^{i\omega t} dt \right) \\
=& -\dot{\Psi}|_{(t=0)} - i\omega[-\Psi_{(t=0)} - i\omega\hat{\Psi}] \\
=& -\omega^2\hat{\Psi} + i\omega\Psi_{(t=0)} - \dot{\Psi}_{(t=0)}
\end{aligned} \tag{7.17}$$

$$\begin{aligned}
\mathcal{L}[\nabla^2\Psi] =& \int_0^\infty \nabla^2\Psi e^{i\omega t} dt \\
=& \nabla^2\mathcal{L}[\Psi] = \hat{\Psi}''
\end{aligned} \tag{7.18}$$

Therefore the wave equation becomes

$$\nabla^2\hat{\Psi} + \omega^2\hat{\Psi} = i\omega\Psi(t=0) + \dot{\Psi}(t=0) \tag{7.19}$$

We solve this inhomogeneous equation using the method of Green's functions. The Greens function is given by the solutions to

$$\left(\frac{d^2}{dr^2} + \frac{1}{r}\frac{d}{dr} + \omega^2 - \frac{l(l+1)}{r^2}\right) g_l = -\frac{1}{r^2}\delta(r-r') \tag{7.20}$$

The solution when $r \neq r'$ is the same as the solution to the homogeneous equation, eq. (7.14). For $r < r'$

$$g_l = A_l(wr')h_l^{(1)}(wr) + B_l(wr')h_l^{(2)}(wr) \tag{7.21}$$

where, due to zero boundary conditions on $r = a$

$$A_l(wr') = -B_l(wr')\frac{h_l^{(2)}(wa)}{h_l^{(1)}(wa)} \tag{7.22}$$

For $r > r'$, using the outgoing wave boundary condition, we have

$$g_l = C_l(wr')h_l^{(1)}(wr) \tag{7.23}$$

We use the condition that $g_l$ must be continuous at $r'$ to write

$$C_l(wr')h_l^{(1)}(wr') = -B_l(wr')\frac{h_l^{(2)}(wa)}{h_l^{(1)}(wa)}h_l^{(1)}(wr') + B_l(wr')h_l^{(2)}(wr') \tag{7.24}$$

which leads to

$$g_l(r,r') = B_l(wr')\left(h_l^{(2)}(wr) - \frac{h_l^{(2)}(wa)}{h_l^{(1)}(wa)}h_l^{(1)}(wr)\right) \qquad (r < r') \tag{7.25}$$

$$g_l(r,r') = B_l(wr')\left(\frac{h_l^{(2)}(wr')}{h_l^{(1)}(wr')}h_l^{(1)}(wr) - \frac{h_l^{(2)}(wa)}{h_l^{(1)}(wa)}h_l^{(1)}(wr)\right) \qquad (r > r') \tag{7.26}$$

which can be written in the form

$$g_l(r,r') = D_l(wr')\left(h_l^{(2)}(wr_<)h_l^{(1)}(wr_>) - \frac{h_l^{(2)}(wa)}{h_l^{(1)}(wa)}h_l^{(1)}(wr)h_l^{(1)}(wr')\right) \tag{7.27}$$

where $D_l(wr') = B_l(wr')h_l^{(1)}(wr')$ and $r_<(r_>)$ is the smallest(greatest) of $r$ and $r'$. To find an expression for $D_l(wr')$ we use the *jump condition* due to the delta function at $r = r'$.

$$-\frac{d}{dr}[g_l]_{r'-\epsilon} + \frac{d}{dr}[g_l]_{r'+\epsilon} = -\frac{1}{r^2} \tag{7.28}$$

At $r = r' + \epsilon$ we use $r_< = r'$ and $r_> = r$, i.e.

$$\frac{d}{dr}[g_l]_{r'+\epsilon} = D_l(wr')\left(h_l^{(2)}(wr')h_l^{(1)}(wr) - \frac{h_l^{(2)}(wa)}{h_l^{(1)}(wa)}h_l^{(1)}(wr)h_l^{(1)}(wr')\right) \tag{7.29}$$

At $r = r' - \epsilon$ we use $r_< = r$ and $r_> = r'$, i.e.

$$\frac{d}{dr}[g_l]_{r'-\epsilon} = D_l(wr')\left(h_l^{(2)}(wr)h_l^{(1)}(wr') - \frac{h_l^{(2)}(wa)}{h_l^{(1)}(wa)}h_l^{(1)}(wr)h_l^{(1)}(wr')\right) \tag{7.30}$$

Substituting into (7.28) gives

$$D_l(wr')\left(h_l^{(2)}(wr')\frac{d}{dr}(h_l^{(1)}(wr))_{r=r'} - h_l^{(1)}(wr')\frac{d}{dr}(h_l^{(2)}(wr))_{r=r'}\right) = \frac{1}{r^2} \tag{7.31}$$

The expression in brackets above is the Wronskian. We calculate this using $h_0^{(1)}(wr) = -\frac{i}{wr}e^{iwr}$ and $h_0^{(2)} = \frac{i}{wr}e^{-iwr}$

$$\begin{aligned} W =& \frac{i}{wr}e^{-iwr}\frac{d}{dr}\left(-\frac{i}{wr}e^{iwr}\right) + \frac{i}{wr}e^{iwr}\frac{d}{dr}\left(\frac{i}{wr}e^{-iwr}\right) \\ =& \frac{i}{wr}e^{-iwr}\left(-\frac{i^2w}{wr}e^{iwr} + \frac{i}{wr^2}e^{iwr}\right) + \frac{i}{wr}e^{iwr}\left(\frac{-i^2w}{wr}e^{-iwr} - \frac{i}{wr^2}e^{-iwr}\right) \\ =& \frac{i(-i^2)}{wr^2} + \frac{i(-i^2)}{wr^2} = \frac{2i}{wr^2} \end{aligned} \tag{7.32}$$

Therefore

$$D_l(wr') = -\frac{1}{r^2}\frac{wr^2}{2i} = \frac{iw}{2} \tag{7.33}$$

and

$$g_l(r,r') = \frac{iw}{2}\left(h_l^{(2)}(wr_<)h_l^{(1)}(wr_>) - \frac{h_l^{(2)}(wa)}{h_l^{(1)}(wa)}h_l^{(1)}(wr)h_l^{(1)}(wr')\right) \tag{7.34}$$

We may now recover the time domain Green's function by the inverse transform

$$G(r,r',t) = \int_{-\infty+ic}^{\infty+ic} \hat{g}(r,r')e^{-i\omega t}d\omega \tag{7.35}$$

the solution is then given by

$$\hat{\Psi}(r,t) = \int_{-\infty}^{+\infty} dr' S_{lm}(r',\omega) G(r,r',t) \tag{7.36}$$

where

$$S_{lm}(r',\omega) = i\omega\Psi(r',0) - \dot{\Psi}(r',0) \tag{7.37}$$

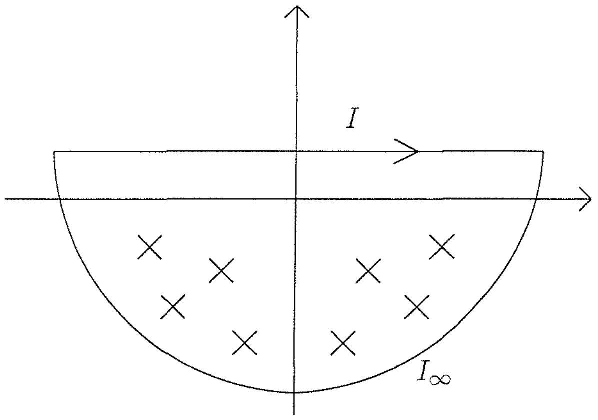

Figure 7.1: Integration contour in complex frequency plane. Crosses mark the singularities which correspond to the modes

In order to calculate the complex integral we consider the contour shown in Fig. 7.1 and use the residue theorem

$$\int I + \int I_\infty = 2\pi i \Sigma Res \tag{7.38}$$

where $I$ is the integral we are interested in and $I_\infty$ is the extension in the lower half of the frequency plane. Following Andersson [81] we argue that the high-frequency semicircle at infinity will not contribute to the integral at most times (but give roughly the "flat space progenitors" at early times) and thus the integral of eq. (7.35) may be found by simply calculating the residue, i.e. by finding the poles of $g_l$. From eq. (7.34) we can see that the singularities of $g_l(r,r',\omega)$ are at $h_l^1(\omega a) = 0$, so the roots of $h_l^1(\omega a)$ will give us the mode frequencies.

## 7.2 Numerical Evolution

We begin again from eq. (7.1) and assuming axisymmetry we remove the $\phi$ dependence

$$\Psi(t,r,\theta,\phi) = \Psi e^{im\phi} \tag{7.39}$$

so that the wave equation becomes

$$\partial_{tt}\Psi - \frac{1}{r^2}\partial_r\left(r^2\partial_r\Psi\right) - \frac{1}{r^2\sin\theta}\partial_\theta\left(\sin\theta\,\partial_\theta\Psi\right) + \frac{m^2}{r^2\sin^2\theta}\Psi = 0 \tag{7.40}$$

### *7.2.1 Cauchy Evolution*

We use our standard second order leapfrog finite difference scheme as described for the one-dimensional wave equation. Here, however we must also use

$$\partial_\theta\Psi^n_{k,j} = \frac{1}{2\Delta\theta}(p^n_{k,j+1} - p^n_{k,j-1}) \tag{7.41}$$

$$\partial_{\theta\theta}\Psi^n_{k,j} = \frac{1}{\Delta\theta^2}(p^n_{k,j+1} - 2p^n_{k,j} + p^n_{k,j-1}) \tag{7.42}$$

and the finite difference version of the two-dimensional wave equation is

$$\begin{aligned} p^{n+1}_{k,j} =& 2p^n_{k,j} - p^{n-1}_{k,j} + \frac{\Delta t^2}{\Delta r^2}(p^n_{k+1,j} - 2p^n_{k,j} + p^n_{k-1,j}) + \frac{\Delta t^2}{\Delta r\, r}(p^n_{k+1,j} - p^n_{k-1,j}) \\ &+ \frac{\Delta t^2}{\Delta\theta^2\, r^2}(p^n_{k,j+1} - 2p^n_{k,j} + p^n_{k,j-1}) + \frac{\Delta t^2\cos\theta}{2\Delta\theta\, r^2\sin^2\theta}(p^n_{k,j+1} - p^n_{k,j-1}) - \frac{\Delta t^2 m^2}{r^2\sin^2\theta}p^n_{k,j} \end{aligned} \tag{7.43}$$

We evolve the area $0 < \theta < \pi$ and use boundary conditions

$$\Psi^n_{0,j} = 0 \tag{7.44}$$

$$\partial_t\Psi^n_{K,j} + \partial_r\Psi^n_{K,j} = 0 \tag{7.45}$$

$$\Psi^n_{k,0} = 0 \tag{7.46}$$

$$\Psi^n_{k,J} = 0 \tag{7.47}$$

We choose as initial data a Gaussian pulse which is moving inwards. For the $\theta$ dependence we choose a function which is consistent with our boundary conditions and with the value of $m$ which is used to separate the $\phi$ coordinate. The results shown in this section are obtained using the function $\sin^2\theta\cos\theta$, i.e. $l = 3$.

Fig. 7.2 shows the output along the direction $\theta = 0.9$ with the inner boundary set at $r = 10$ and the outer boundary at $r = 230$. Fig. 7.3 shows the evolution for $0 < \theta < \pi$ at constant radius, $r = 20$. Fig. 7.4 shows the time variation of the log of the solution at $\theta = 0.9$, $r = 30$. Here we see the quasi normal modes of the system. The expected frequency can be calculated as the zero of the spherical Hankel function of the first kind. Since we are using initial data with $m = 2, l = 3$ we must find the roots of

$$(\omega a)^3 + 6i(\omega a)^2 - 15(\omega a) + 15i = 0 \tag{7.48}$$

The roots may be found quite easily using a computer algebra system such as MAPLE. We find the following three roots

$$z_1 = 1.7544 - 1.8389i \tag{7.49}$$

$$z_2 = -1.7544 - 1.8389i \tag{7.50}$$

$$z_3 = 0 - 2.3222i \tag{7.51}$$

We expect that $\omega a = 1.75$, i.e $\omega = 0.175$ for $a = 10$. This gives us a frequency and half period for the modes of

$$f = \frac{\omega}{2\pi} \tag{7.52}$$

$$\frac{P}{2} = \frac{\pi}{\omega} \approx 18 \tag{7.53}$$

This half period approximately fits the measured value from Fig. 7.4 of 16.7. It is not surprising that the fit is not very close because we see so few modes with which to measure the frequency. The accuracy of the frequency calculation could be improved by using a fast Fourier transform.

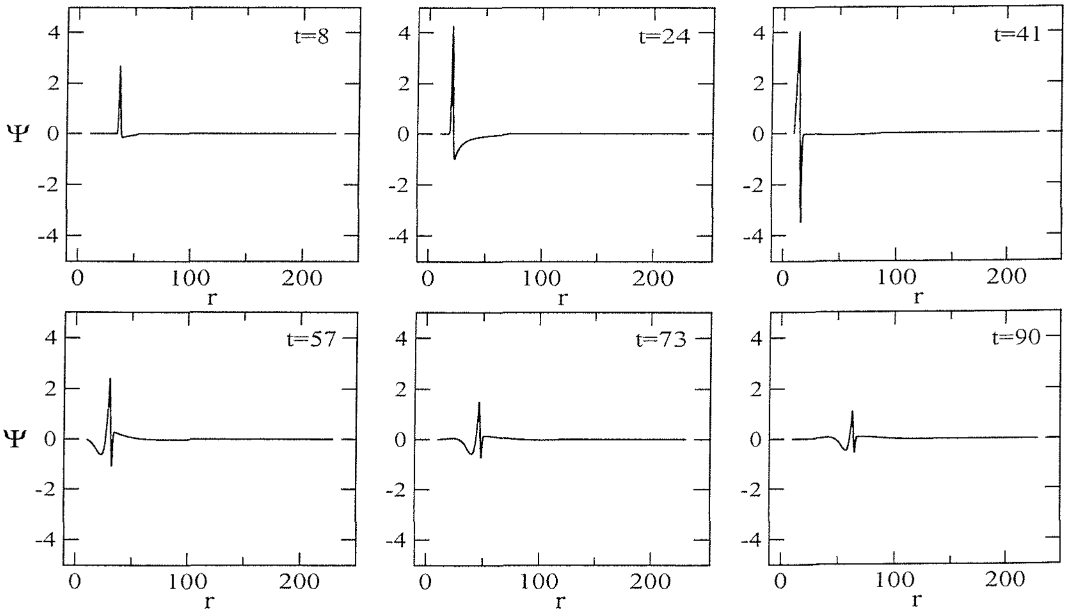

Figure 7.2: Cauchy evolution of the two-dimensional wave equation for a constant $\theta$ direction. The initial pulse is reflected by the hard sphere at the inner boundary.

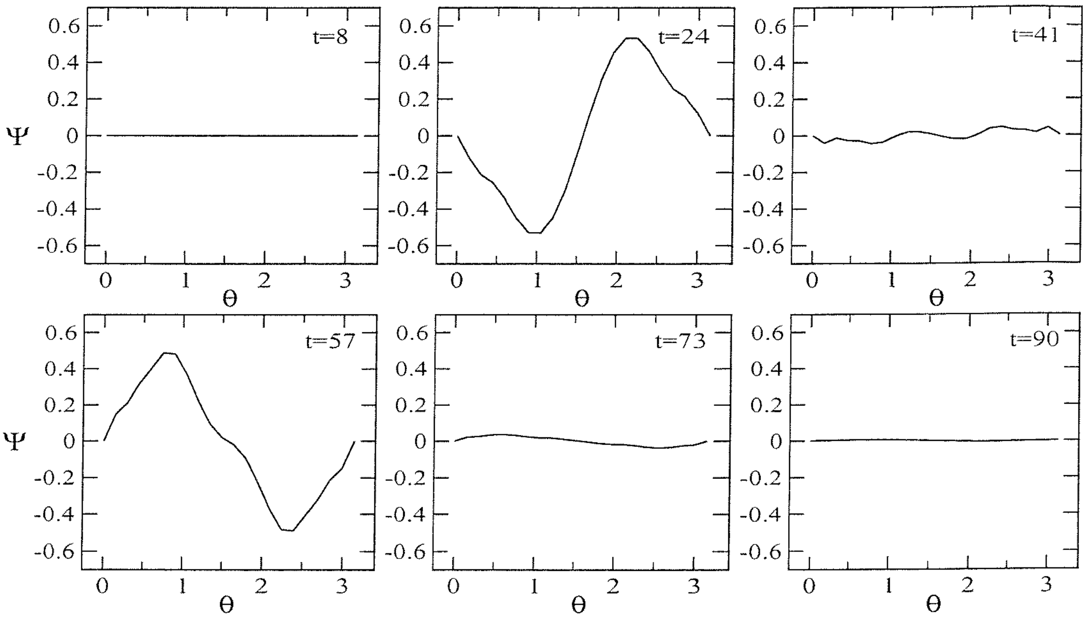

Figure 7.3: Cauchy evolution of the axisymmetric wave equation for a constant $r$ surface. The results are not so smooth in the $\theta$ direction but this is improved by adjusting the resolution, $\Delta\theta$.

### *7.2.2 Characteristic evolution*

We transform eq. (7.40) to characteristic coordinates $(u, r, \theta)$ where $u = t - r$ to get

$$2\partial_{ru}\Psi + \frac{2}{r}\Psi_u - \frac{1}{r^2}(r^2\Psi_r)_r - \frac{1}{r^2\sin\theta}(\sin\theta\Psi_\theta)_\theta + \frac{m^2}{r^2\sin^2\theta}\Psi = 0 \qquad (7.54)$$

In order to fully exploit the characteristic formulation we compactify the radial coordinate by transforming to a new coordinate $x$ given by

$$x = \frac{r}{1+r}, \qquad 0 < r < \infty, \qquad 0 < x < 1 \qquad (7.55)$$

The wave eq. written in terms of this new coordinate is

$$2(1-x)^2\partial_{ux}\Psi + \frac{2}{x}(1-x)\partial_u\Psi - (1-x)^4\partial_{xx}\Psi + 2(1-x)^3\left(1-\frac{1}{x}\right)\partial_x\Psi$$
$$-\frac{(1-x)^2}{x^2\sin\theta}\partial_\theta(\sin\theta\partial_\theta\Psi) + \frac{m^2(1-x)^2}{x^2\sin^2\theta} = 0 \qquad (7.56)$$

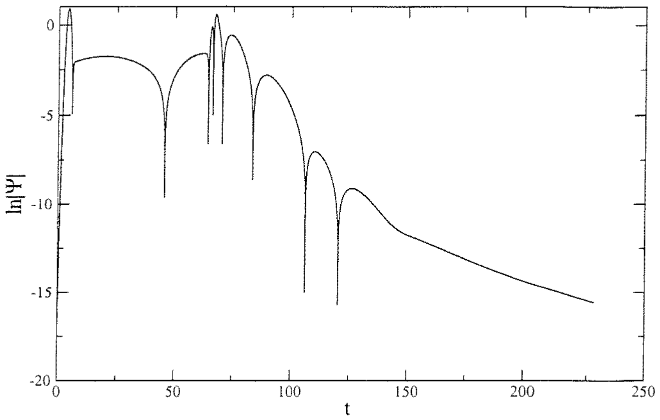

Figure 7.4: Log of the solution from the Cauchy evolution to the axisymmetric wave equation, showing modes

We finite difference this equation using by calculating the derivatives at position $(n+1/2, k-1/2, j)$. The derivatives involving $u$ and $x$ are finite differenced using the same scheme we used for the one-dimensional null-timelike evolutions. Now we also include the derivatives in $\theta$ as

$$\partial_\theta \Psi = \frac{1}{4\Delta x}(p^{n+1}_{k-1,j+1} - p^{n+1}_{k-1,j-1} + p^{n}_{k,j+1} - p^{n}_{k,j-1}) \tag{7.57}$$

$$\partial_{\theta\theta} \Psi = \frac{1}{2\Delta x^2}(p^{n+1}_{k-1,j+1} - 2p^{n+1}_{k-1,j} + p^{n+1}_{k-1,j-1} + p^{n}_{k,j+1} - 2p^{n}_{k,j} + p^{n}_{k,j-1}) \tag{7.58}$$

and our finite differenced evolution equation is

$$\begin{aligned} p^{n+1}_{k,j} = {} & \frac{D2}{D1}p^{n+1}_{k-1,j} + \frac{D3}{D1}(p^{n+1}_{k-2,j} + p^{n}_{k+1,j}) + \frac{D4}{D1}p^{n}_{k,j} + \frac{D5}{D1}p^{n}_{k-1,j} \\ & + \frac{D6}{D1}(p^{n+1}_{k-1,j+1} + p^{n}_{k,j+1}) + \frac{D7}{D1}(p^{n+1}_{k-1,j-1} + p^{n}_{k,j-1}) \end{aligned} \tag{7.59}$$

where

$$D1 = \frac{2(1-x)^2}{\Delta u \Delta x} + \frac{(1-x)}{x\Delta u} + \frac{(1-x)^3}{\Delta x}\left(1+\frac{1}{x}\right) - \frac{(1-x)^4}{2\Delta x^2} \tag{7.60}$$

$$D2 = \frac{2(1-x)^2}{\Delta u \Delta x} - \frac{(1-x)}{x\Delta u} + \frac{(1-x)^3}{\Delta x}\left(1+\frac{1}{x}\right) - \frac{(1-x)^4}{\Delta x^2} - \frac{(1-x)^2}{\Delta\theta^2 x^2} - \frac{m^2(1-x)^2}{2x^2\sin^2\theta} \tag{7.61}$$

$$D3 = \frac{(1-x)^4}{2\Delta x^2} \tag{7.62}$$

$$D4 = \frac{2(1-x)^2}{\Delta u \Delta x} + \frac{(1-x)}{x\Delta u} - \frac{(1-x)^3}{\Delta x}\left(1+\frac{1}{x}\right) - \frac{(1-x)^4}{\Delta x^2} - \frac{(1-x)^2}{\Delta\theta^2 x^2} - \frac{m^2(1-x)^2}{2x^2\sin^2\theta} \tag{7.63}$$

$$D5 = -\frac{2(1-x)^2}{\Delta u \Delta x} + \frac{(1-x)}{x\Delta u} + \frac{(1-x)^3}{\Delta x}\left(1+\frac{1}{x}\right) + \frac{(1-x)^4}{2\Delta x^2} \tag{7.64}$$

$$D6 = \frac{(1-x)^2}{2\Delta\theta^2 x^2} + \frac{(1-x)^2\cos\theta}{4\Delta\theta x^2\sin\theta} \tag{7.65}$$

$$D7 = \frac{(1-x)^2}{2\Delta\theta^2 x^2} - \frac{(1-x)^2\cos\theta}{4\Delta\theta x^2\sin\theta} \tag{7.66}$$

and all coefficients are calculated at $(n+1/2, k-1/2, j)$.

A zero boundary condition is implemented at $k=0$, i.e at some positive value of $x$. As in the one dimensional case, we must make some adjustment to our evolution equation in order to calculate the new value at position $k=1$, the first radially inward point from the inner boundary. Here we cannot use point $(n+1, k-2, j)$ because it does not exist. We use the same method described previously in one dimension, i.e. the double $x$-derivative is calculated to first order here only. At the outer boundary another small adjustment is made to eqs. (7.59) and (7.66). We do not have a gridpoint at $(n, k+1, j)$ and so we use a second order one sided derivative here. Zero boundary conditions are imposed at $\theta = 0$ and $\theta = \pi$.

We choose initial data which is a pulse in the $x$ direction and the function $\sin^2\theta\cos\theta$ in the theta direction with $m=2$. We therefore expect modes of $l=3$ and a frequency given by $\omega a = 1.75$.

The results are shown in Fig. 7.5 for output on a constant $\theta = 0.54$, and in Fig. 7.6 for a constant radius. We have set the inner boundary, $a$, at $x=0.5$, i.e. $r=1$ and therefore expect the quasi-normal modes to have frequency and half-period given by

$$f = \frac{\omega}{2\pi} \tag{7.67}$$

$$P = \frac{\pi}{\omega} \approx 1.8 \tag{7.68}$$

The log of the solution obtained for an angle $\theta = 0.9$ at future null infinity is shown in Fig. 7.7 as function of $u$. The calculated frequency of 1.63 compares well with the analytic result.

I have tested the characteristic code for second order convergence. The results are shown in Fig. 7.8. The solid line is the result for a test using $x$-direction resolutions of 2000, 4000 and 8000 gridpoints, whereas the dashed line shows the result for a lower resolution test of 1000, 2000 and 4000 gridpoints. The convergence is second order up to about $t = 5$ but then increases. This could be due to instability problems with the lower resolution runs. This is supported by the fact that the second order convergence is extended in the higher resolution test. Low resolution stability problems can be seen in Fig. 7.9 which shows the output at one point for successively higher resolution runs.

One condition which is necessary for stability is the Courant condition, i.e. that the numerical domain of dependence should include the physical domain of dependence. In the case of the characteristic code described above, this translates to the necessity for the three points, $p^n_{k+1,j}$, $p^n_{k,j+1}$ and $p^n_{k,j-1}$ to lie outside the past null-cone from the point $p^{n+1}_{k,j}$. The equation of the characteristics in flat space is given by

$$(x - x_0)^2 + (y - y_0)^2 + (z - z_0)^2 - (t - t_0)^2 = 0 \tag{7.69}$$

so for the example above, considering the point $p^n_{k+1,j}$ gives the condition

$$(\Delta r)^2 - (-\Delta u + \Delta r)^2 = 0 \tag{7.70}$$

$$\therefore \Delta u \leq 2\Delta r \tag{7.71}$$

Considering the other two points we require

$$(r\sin\theta - r\sin(\theta + \Delta\theta))^2 + (r\cos\theta - r\cos(\theta + \Delta\theta))^2 - (-\Delta u)^2 = 0 \tag{7.72}$$

$$\therefore \Delta u \leq \sqrt{2}r\sqrt{\cos(\Delta\theta) - 1} \tag{7.73}$$

At large $r$ the first condition will dominate, but near the origin the second condition becomes highly restrictive and we can see that this scheme leads to an unconditional instability at the point $r = 0$. Fortunately, in the above example of waves reflecting from a solid sphere we do not have to worry about this problem but we must consider the second condition when the radius of the sphere is very small.

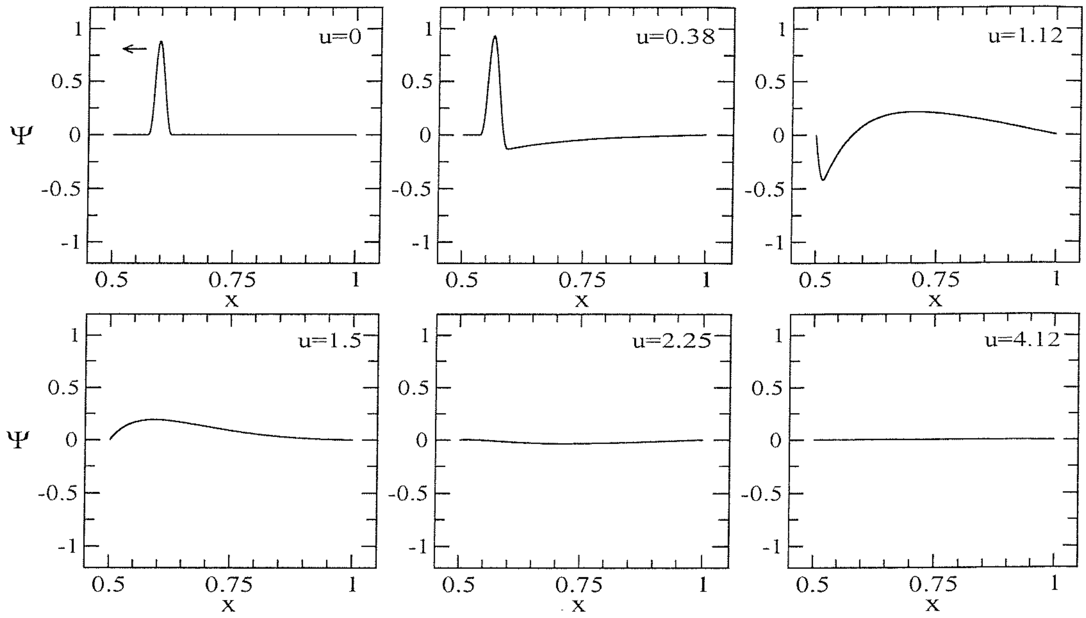

Figure 7.5: Characteristic (null-timelike) evolution of the axisymmetric wave equation with reflection from a hard sphere shown on a constant $\theta$ surface. The $y$ axis is scaled by $10^3$.

## 7.3 Chapter Summary

In this chapter I have evolved the axisymmetric wave equation as a Cauchy and a characteristic initial value problem for the case of a pulse scattering off a hard sphere. This toy problem has been good preparation because it has extended the numerical techniques to two dimensions. The axisymmetric wave equation is similar in form to the scalar wave equation in Kerr and Kerr-de Sitter spacetimes which will be the focus of the next two chapters. I have also investigated the convergence and stability properties of numerical schemes that I will use in the following chapters.

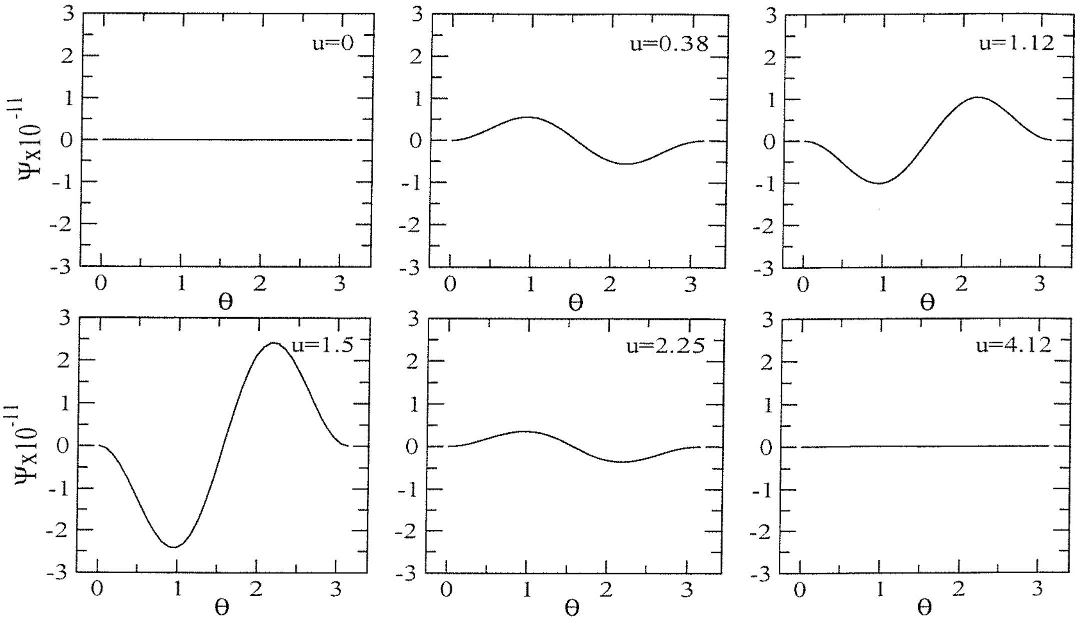

Figure 7.6: Characteristic (null-timelike) evolution of the axisymmetric wave equation with reflection from hard sphere shown on a constant $r$ surface.

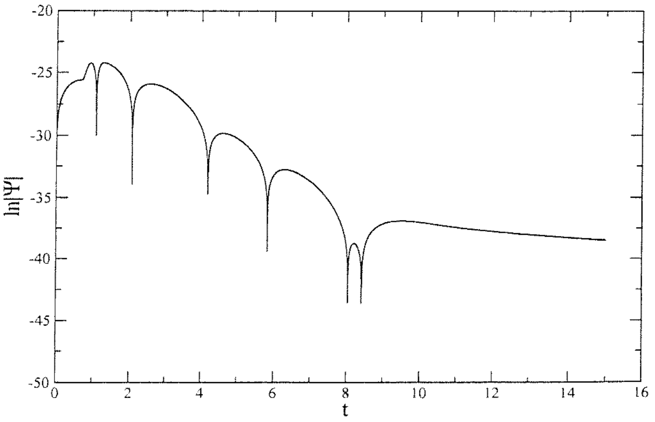

Figure 7.7: Log of the solution to the characteristic evolution of the axisymmetric wave equation at future null infinity, showing modes

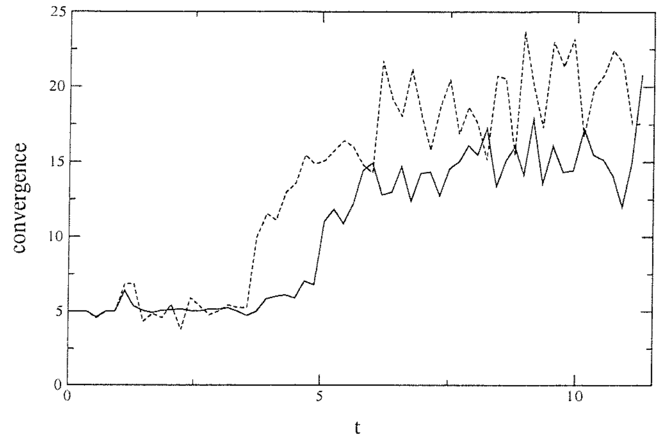

Figure 7.8: Results of two convergence tests on the characteristic evolution of the axisymmetric wave equation. The dashed line represents a lower resolution convergence test. This figure shows that the convergence improves with higher resolution.

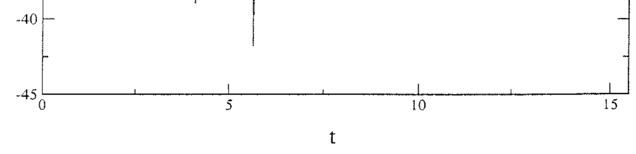

Figure 7.9: Solution from axisymmetric wave characteristic evolution at one point for three grids of different resolution. Dotted line: 1000 gridpoints, dashed line: 2000 gridpoints, solid line: 4000 gridpoints. The amplitude was shifted slightly in order to display the results together more clearly.

# Chapter 8

# A Characteristic Approach to Perturbed Kerr Black Holes

## 8.1 Kerr Spacetime

As a rotating star collapses to form a black hole, its rotation increases, although according to Thorne [87] the maximum angular velocity for a Kerr black hole is, $a/M = 0.998$. Rotation has a dramatic effect on the structure of the spacetime surrounding the black hole. As the black hole rotates it drags the spacetime with it. This results in two photon orbits on the equatorial plane, one for co-rotating and another for counter-rotating photons. The distance between those two photon orbits increases with the angular velocity. Rotating black holes possess an *ergosphere*, a region of spacetime in which it is impossible to stay still. The outer boundary of the ergosphere corresponds to the static limit of the black hole but, unlike the case of non-rotating black holes, this boundary is outside the event horizon, and therefore, particles may return from this region.

Whereas Schwarzschild black holes have only one horizon, a Kerr black hole has two. At the outer horizon, an observer would experience a reversal of roles for time and space. At the inner horizon, time and space switch roles again to act as they do outside the horizons. There is much more that could be said about the internal structure and the singularity beyond the Kerr horizons, but the focus of this chapter is on the exterior region.

In the previous chapters I have developed the necessary skills for evolving perturbations against the exterior spacetime of a Kerr black hole. Here I describe the derivation of the Teukolsky equation governing scalar, electromagnetic, and gravitational perturbations in Kerr spacetime. I then describe characteristic codes that I have developed to evolve the scalar equation in null-timelike and double-null coordinates. I also present some results using an old Cauchy code [2] which contribute to a recent debate over the late-time fall-off for initial data of spherical harmonic form with $m = 0, l = 4$, and some evidence to support the superradiant resonance cavity interpretation for the late-time behaviour or rapidly rotating black holes.

## 8.2 The Teukolsky Equation

The derivation of the Regge-Wheeler equation in Chapter 6 involved perturbing the metric, $g^{(B)}_{\mu\nu} + h_{\mu\nu}$, calculating the Ricci tensor, keeping only the terms which are of first-order in $h_{\mu\nu}$, and then substituting into the vacuum Einstein equations. In that case spherical symmetry allowed us to decompose into spherical harmonics, however the axial-symmetry of Kerr space-time makes the separation of the $r$ and $\theta$ coordinates impossible by this method and we end up with a PDE in $r$ and $\theta$ rather than two separated ODEs. In Kerr spacetime an alternative method for separating the $r$ and $\theta$ equations must be used, as first presented by Teukolsky [21]. This method utilizes the Newman-Penrose formalism which I describe here following the presentation of Chandrasekhar [80]. We will return to the derivation of the wave equation in Kerr spacetime after reviewing the mathematical foundations.

### *8.2.1 Tetrad Formalism*

In the tetrad formalism a suitable tetrad basis of four linearly independent vector-fields is chosen and the equations are expressed in terms of the relevant quantities projected onto that basis. We represent our basis of four contravariant vectors as

$$e^i_{(a)} \, (a = 1, 2, 3, 4) \tag{8.1}$$

Note that here I use Latin indices to represent 4-dimensions whereas I have previously used Greek indices. This is to avoid confusion later when using spin coefficients (with Greek symbols) in the Newman-Penrose formalism The associated covariant vectors are

$$e_{(a)i} = g_{ik} e^k_{(a)} \tag{8.2}$$

where $g_{ik}$ denotes the metric tensor. The inverse of (8.1) is $e^{(b)}_i$ so that

$$e^i_{(a)} e^{(b)}_i = \delta^{(b)}_{(a)} \tag{8.3}$$

$$e^i_{(a)} e^{(a)}_j = \delta^i_j \tag{8.4}$$

It is also assumed that

$$e^i_{(a)} e_{(b)i} = \eta_{(a)(b)} \tag{8.5}$$

where $\eta_{(a)(b)}$ is a constant symmetric matrix with inverse $\eta^{(a)(b)}$.

Given any vector or tensor field, its tetrad components are obtained by projection onto the tetrad frame. In general we have

$$T_{(a)(b)} = e^i_{(a)} e^j_{(b)} T_{ij} = e^i_{(a)} T_{i(b)} \tag{8.6}$$

$$T_{ij} = e^{(a)}_i e^{(b)}_j T_{(a)(b)} = e^{(a)}_i T_{(a)j} \tag{8.7}$$

By considering the contravariant vectors $e_{(a)}$ as tangent vectors we can define directional derivatives as

$$e_{(a)} = e^i_{(a)} \frac{\partial}{\partial x^i} \tag{8.8}$$

and using this definition gives

$$A_{(a),(b)} = e^j_{(a)} A_{j;i} e^i_{(b)} + \gamma_{(c)(a)(b)} A^{(c)} \tag{8.9}$$

where

$$\gamma_{(c)(a)(b)} = e_{(a)k;i} e^i_{(b)} e^k_{(c)} \tag{8.10}$$

are called the Ricci rotation-coefficients and are antisymmetric in the first pair of indices. If eq.(8.9) is written in the form

$$e^j_{(a)} A_{j;i} e^i_{(b)} = A_{(a),(b)} + \eta^{(n)(m)} \gamma_{(n)(a)(b)} A_{(m)} \tag{8.11}$$

then the right-hand side of this equation is called the *intrinsic derivative* of $A_{(a)}$ in the direction $e_{(b)}$, which is written as $A_{(a)|(b)}$. The directional and intrinsic derivatives are therefore related by

$$A_{(a)|(b)} = A_{(a),(b)} + \eta^{(n)(m)} \gamma_{(n)(a)(b)} A_{(m)} \tag{8.12}$$

The Lie bracket, $[e_{(a)}, e_{(b)}] = (e_{(a)} e_{(b)} - e_{(b)}, e_{(a)})$, can also be expanded in terms of our tetrad basis as

$$[e_{(a)}, e_{(b)}] = C^{(c)}_{(a)(b)} e_{(c)} \tag{8.13}$$

where the coefficients, $C^{(c)}_{(a)(b)}$ are called the *structure constants*. They are antisymmetric in the indices $(a)$ and $(b)$ and thus there are 24 in total. The structure constants can be written in terms of the rotation coefficients as

$$C^{(c)}_{(a)(b)} = \gamma^{(c)}_{(b)(a)} - \gamma^{(c)}_{(a)(b)} \tag{8.14}$$

When eq. (8.13) is written out explicitly with the structure constants written in terms of the rotation coefficients, the resultant 24 equations are called the *commutation relations*.

It is also possible to project the Ricci identity onto the tetrad frame. The result is given interms of the rotation coefficients as

$$\begin{aligned} R_{(a)(b)(c)(d)} =& -\gamma_{(a)(b)(c),(d)} + \gamma_{(a)(b)(d),(c)} + \gamma_{(b)(a)(f)}\left[\gamma_{(c)}{}^{(f)}{}_{(d)} - \gamma_{(d)}{}^{(f)}{}_{(c)}\right] \\ &+ \gamma_{(f)(a)(c)}\gamma_{(b)}{}^{(f)}{}_{(d)} - \gamma_{(f)(a)(d)}\gamma_{(b)}{}^{(f)}{}_{(c)} \end{aligned} \tag{8.15}$$

which, considering symmetries, gives 36 equations in total. The Bianchi identity can similarly be written as

$$\begin{aligned} R_{(a)(b)[(c)(d)|(f)]} =& \frac{1}{6}\sum_{[(c)(d)(f)]}\{R_{(a)(b)(c)(d),(f)} \\ &- \eta^{(n)(m)}[\gamma_{(n)(a)(f)}R_{(m)(b)(c)(d)} + \gamma_{(n)(b)(f)}R_{(a)(m)(c)(d)} \\ &+ \gamma_{(n)(c)(f)}R_{(a)(b)(m)(d)} + \gamma_{(n)(d)(f)}R_{(a)(b)(c)(m)}]\} \end{aligned} \tag{8.16}$$

### *8.2.2 Newman-Penrose Formalism*

In the Newman-Penrose (NP) formalism the basis vectors are chosen as a tetrad of null vectors, $l, n, m$ and $m^*$, where $l$ and $n$ are real and $m$ and $m^*$ are complex conjugates of one another. The null vectors satisfy orthogonality conditions

$$l \cdot m = l \cdot m^* = n \cdot m = n \cdot m^* = 0 \tag{8.17}$$

and we also impose normalisation conditions

$$l \cdot n = 1 \qquad m \cdot m^* = -1 \tag{8.18}$$

which are not necessary but lead to significant simplification. These conditions together with the null properties

$$l \cdot l = n \cdot n = m \cdot m = m^* \cdot m^* = 0 \tag{8.19}$$

enable us to write the fundamental matrix $\eta_{(a)(b)}$ (see eq.(8.5)) as

$$\eta_{(a)(b)} = \begin{pmatrix} 0 & 1 & 0 & 0 \\ 1 & 0 & 0 & 0 \\ 0 & 0 & 0 & -1 \\ 0 & 0 & -1 & 0 \end{pmatrix} \tag{8.20}$$

where we have used

$$e_1 = l, \qquad e_2 = n, \qquad e_3 = m, \qquad e_4 = m^* \tag{8.21}$$

The directional derivatives are given special symbols

$$e_1 = e^2 = D, \qquad e_2 = e^1 = \Delta, \qquad e_3 = -e^4 = \delta, \qquad e_4 = -e^3 = \delta^* \tag{8.22}$$

as also are the rotation coefficients, now refered to as *spin coefficients*

$$\begin{array}{lll} \kappa = \gamma_{311} & \rho = \gamma_{314} & \epsilon = \frac{1}{2}(\gamma_{211} + \gamma_{341}) \\ \sigma = \gamma_{313} & \mu = \gamma_{243} & \gamma = \frac{1}{2}(\gamma_{212} + \gamma_{342}) \\ \lambda = \gamma_{244} & \tau = \gamma_{312} & \alpha = \frac{1}{2}(\gamma_{214} + \gamma_{344}) \\ \nu = \gamma_{242} & \pi = \gamma_{241} & \beta = \frac{1}{2}(\gamma_{213} + \gamma_{343}) \end{array} \tag{8.23}$$

The equation relating the Weyl, Riemann and Ricci tensors and the scalar curvature is

$$\begin{aligned} R_{abcd} = C_{abcd} &- \frac{1}{2}(\eta_{ac}R_{bd} - \eta_{bc}R_{ad} - \eta_{ad}R_{bc} + \eta_{bd}R_{ac} \\ &+ \frac{1}{6}(\eta_{ac}\eta_{bd} - \eta_{ad}\eta_{bc})R \end{aligned} \tag{8.24}$$

where $R_{abcd}$ is the Riemann tensor, $C_{abcd}$ is the Weyl tensor, $R_{ab}$ is the Ricci tensor, and $R$ is the scalar curvature. By using the trace-free property of the Weyl tensor along with the property

$$C_{1234} + C_{1342} + C_{1423} = 0 \tag{8.25}$$

we find 10 independent components of the Weyl tensor, which are represented by the five NP complex scalars

$$\begin{aligned} \Psi_0 &= -C_{1313} = -C_{pqrs}l^p m^q l^r m^s \\ \Psi_1 &= -C_{1213} = -C_{pqrs}l^p n^q l^r m^s \\ \Psi_2 &= -C_{1342} = -C_{pqrs}l^p m^q m^{*r} n^s \\ \Psi_3 &= -C_{1242} = -C_{pqrs}l^p n^q m^{*r} n^s \\ \Psi_4 &= -C_{2424} = -C_{pqrs}n^p m^{*q} n^r m^{*s} \end{aligned} \tag{8.26}$$

We can therefore obtain

$$C_{1334} = \Psi_1 \qquad C_{2443} = \Psi_3 \qquad C_{1212} = C_{3434} = -(\Psi_2 + \Psi_2^*) \qquad C_{1234} = \Psi_2 - \Psi_2^* \tag{8.27}$$

The ten components of the Ricci tensor are defined by the following scalars

$$\begin{aligned}
&\Phi_{00} = -\frac{1}{2}R_{11} \qquad \Phi_{22} = -\frac{1}{2}R_{22} \qquad \Phi_{02} = -\frac{1}{2}R_{33} \qquad \Phi_{20} = -\frac{1}{2}R_{44} \\
&\Phi_{01} = -\frac{1}{2}R_{13} \qquad \Phi_{10} = -\frac{1}{2}R_{14} \qquad \Phi_{12} = -\frac{1}{2}R_{23} \qquad \Phi_{21} = -\frac{1}{2}R_{24} \\
&\Phi_{11} = -\frac{1}{4}(R_{12} + R_{34}) \qquad \Lambda = \frac{1}{24}R = \frac{1}{12}(R_{12} - R_{34})
\end{aligned} \tag{8.28}$$

The commutation relations, Ricci identities and Bianchi identities can now be written out in terms of the symbols introduced in this formalism. This leads to a large set of equations which we will not repeat here. They may be found in [80] or [56]. The physical meaning of all the NP quantities and equations is not clear, however we do not worry too much about this - the equations serve our purposes in deriving a separable equation for perturbations in Kerr spacetime.

In order to get some feeling for working in the NP formalism we explicitly work out some of the main equations. Consider the commutation relation

$$\begin{aligned}
[\delta, D] = [e_3, e_1] &= (\gamma_{c13} - \gamma_{c31})e^c \\
&= (\gamma_{213} - \gamma_{231})D - \gamma_{131}\Delta - \gamma_{313}\delta^* - (\gamma_{413} - \gamma_{431})\delta
\end{aligned} \tag{8.29}$$

where we have used eq. (8.13), eq. (8.14) and eq. (8.22). By applying eqs.(8.23) we get the NP equation

$$\delta D - D\delta = (\alpha^* + \beta - \pi^*)D + \kappa\Delta - (\rho^* + \epsilon - \epsilon^*)\delta - \sigma\delta^* \tag{8.30}$$

Now consider the (1313)-component of eq. (8.15), the Ricci identity. By writing this equation out in full and using $\eta$, eq. (8.20), for lowering tetrad indices and also using the fact that the rotation coefficients are antisymmetric on the first two indices, we find

$$\begin{aligned}
R_{1313} = \gamma_{131,3} + \gamma_{133,1} &+ \gamma_{133}(\gamma_{121} + 2\gamma_{431} - \gamma_{413} + \gamma_{134}) \\
&- \gamma_{131}(\gamma_{433} + \gamma_{123} - \gamma_{213} + \gamma_{231} + \gamma_{132})
\end{aligned} \tag{8.31}$$

Then using eq. (8.22) and eq. (8.23) we obtain the NP equation

$$-\Psi_0 = -D\sigma - \delta\kappa + \sigma(\rho^* + \rho + 3\epsilon - \epsilon^*) + \kappa(-\tau + \pi^* - 3\beta - \alpha^*) \tag{8.32}$$

A similar operation enables us to write out the 20 linearly independent Bianchi identities, eq. (8.16), in this formalism. Consider the identity

$$R_{13[13|4]} = R_{1313|4} + R_{1334|1} + R_{1341|3} = 0 \tag{8.33}$$

This can also be written as

$$C_{1313|4} + (C_{1334} + \frac{1}{2}R_{13})_{|1} - \frac{1}{2}R_{11|3} = 0 \tag{8.34}$$

where

$$C_{1313|4} = -\delta^*\Psi_0 + 4\alpha\Psi_0 - 4\rho\Psi_1 \tag{8.35}$$

$$C_{1334|1} = D\Psi_1 - 2\epsilon\Psi_1 + 3\kappa\Psi_2 - \pi\Psi_0 \tag{8.36}$$

and

$$\begin{aligned}\frac{1}{2}(R_{13|1} - R_{11|3}) =& - \Phi_{01,1} + \Phi_{00,3} - \Phi_{00}(-\gamma_{231} + 2\gamma_{213}) - 2\Phi_{11}\gamma_{131}\\ & - \Phi_{01}(-\gamma_{211} - 2\gamma_{413} + \gamma_{431}) + 2\Phi_{10}\gamma_{313} - \Phi_{02}\gamma_{411}\\ =& - D\Phi_{01} + \delta\Phi_{00} + 2\Phi_{01}(\epsilon + \rho^*) + 2\Phi_{10}\sigma - 2\Phi_{11}\kappa\\ & - \Phi_{02}\kappa^* + \Phi_{00}(\pi^* - 2\alpha^* - 2\beta)\end{aligned} \tag{8.37}$$

Eq. (8.33) can now be written explicitly in NP terms by combining eqs. (8.35), (8.36) and (8.37).

### *8.2.3 Tetrad Rotations and the Petrov Classifications*

When a Lorentz tranformation is imposed upon the basis vectors $l$, $n$, $m$ and $m^*$, it can be considered as belonging to one of three kinds of rotations:

- Class *I* - leaves vector $l$ unchanged
- Class *II* - leaves vector $n$ unchanged
- Class *III* - leaves the direction of $l$ and $n$ unchanged and rotates $m$ by some angle $\theta$ in the $(m, m^*)$-plane

The corresponding transformations of the various NP quantities can be found in Chandrasekhar [80].

We can classify the Weyl tensor into different types by subjecting the complex scalars, $\Psi_0 ... \Psi_4$, to Lorentz transformation and determining which of the complex scalars can be made to vanish. This is the *Petrov classification* and there are 5 *Petrov types.*

Consider a system with $\Psi_4 \neq 0$ and subject the frame to a rotation of class *II*. The Weyl scalar $\Psi_0$ transforms in the following manner (as given in eq. (346) of

Chandrasekhar [80]):

$$\Psi_0^{(new)} = \Psi_0 + 4b\Psi_1 + 6b^2\Psi_2 + 4b^2\Psi_3 + b^4\Psi_4 \tag{8.38}$$

To make $\Psi_0^{new}$ vanish we must find the roots of the right hand side of this equation. In an *algebraically general* tensor all four roots are distinct but an *algebraically special* tensor has two or more identical roots. The new directions of $l$, i.e.

$$l^{(new)} = l + b^*m + bm^* + bb^*n \tag{8.39}$$

are called the *principal null directions* of the Weyl tensor. The principal null directions are directly observable quantities of the spacetime [88], for more information on principal null directions see section 8 of Penrose and Rindler [89].

The Kerr metric is of Petrov type D. For type D, eq.(8.38) has two distinct double roots. In this case we can make $\Psi_0$, $\Psi_1$, $\Psi_3$ and $\Psi_4$ vanish to leave only $\Psi_2$. This is done by a rotation of class *II* followed by a rotation of class *I*. See Chandrasekhar [80] for more details about this and the other Petrov types.

### *8.2.4 Perturbation Equations*

We may now begin the derivation of the perturbation equations. Here we follow the method of Teukolsky [21]. Rather than perturb the metric directly as we did in the derivation of the Regge-Wheeler equation in Chapter 6, we now perturb the null basis vectors,$l = l^{(B)} + l^{(P)}$, $n = n^{(B)} + n^{(P)}$, etc. where the superscript $B$ labels the background quantities and $P$ labels the perturbed quantity. The NP quantities become $\Psi_2 = \Psi_2^{(B)} + \Psi_2^{(P)}$, $D = D^{(B)} + D^{(P)}$ etc.

The Kerr metric is of type D and therefore we may choose the $l$ and $n$ vectors of the unperturbed tetrad to lie along the repeated principle null directions of the Weyl tensor. This simplifies the NP equations because several of the NP quantities become reduced to zero. The only remaining non-zero background scalar is $\Psi_2^{(B)}$ and the background spin coefficients, $\kappa^{(B)}$, $\sigma^{(B)}$, $\nu^{(B)}$, $\lambda^{(B)}$ also become zero.

Consider the following three perturbed NP equations

$$(\delta * -4\alpha + \pi)\Psi_0^{(P)} - (D - 4\rho - 2\epsilon)\Psi_1^{(P)} - 3\kappa^{(P)}\Psi_2 = 0 \tag{8.40}$$

$$(\Delta - 4\gamma + \mu)\Psi_0^{(P)} - (\delta - 4\tau - 2\beta)\Psi_1^{(P)} - 3\sigma\Psi_2 = 0 \tag{8.41}$$

$$(D - \rho - \rho * -3\epsilon + \epsilon *)\sigma^{(P)} - (\delta - \tau + \pi * -\alpha * -3\beta)\kappa^{(P)} - \Psi_0^{(P)} = 0 \tag{8.42}$$

These correspond to equations (321a), (321e) and (310b) respectively in Chandrasekhar [80]. We also use the equations

$$D\Psi_2 = 3\rho\Psi_2 \tag{8.43}$$

$$\delta\Psi_2 = 3\tau\Psi_2 \tag{8.44}$$

which correspond to equations (321b) and (321f) respectively in Chandrasekhar, to write eq. (8.42) as

$$(D - 3\epsilon + \epsilon * -4\rho - \rho *)\Psi_2\sigma^{(P)} - (\delta + \pi * -\alpha * -3\beta - 4\tau)\Psi_2\kappa^{(P)} - \Psi_0^{(P)}\Psi_2 \tag{8.45}$$

By operating with $(D - 3\epsilon + \epsilon * -4\rho - \rho *)$ on eq. (8.41) and with $(\delta + \pi * -\alpha * -3\beta - 4\tau)$ on eq. (8.40) and subtracting one equation from the other, we can use the commutation relation

$$\begin{aligned}&(D - (p+1)\epsilon + \epsilon * +q\rho - \rho *)(\delta - p\beta + q\tau)\\ &\qquad - (\delta - (p+1)\beta - \alpha * +\pi * +q\tau)(D - p\epsilon + q\rho) = 0\end{aligned} \tag{8.46}$$

with $p = 2$ and $q = -4$ to eliminate $\Psi_1^{(P)}$. Then eq. (8.45) may be used to eliminate $\sigma^{(P)}$ and $\kappa^{(P)}$ in favour of $\Psi_2\Psi_0^{(P)}$. This gives us the decoupled equation for $\Psi_0^{(P)}$

$$+\pi - 4\alpha) - 3\Psi_2]\Psi_0^{(P)} = 0$$

A similar equation may be found for $\Psi_4^{(P)}$ by making the transformations $l \rightarrow n$ and $m \rightarrow m^*$ under which the NP equations are invariant. The result is

$$\begin{aligned}&[(\Delta + 3\gamma - \gamma^* + 4\mu + \mu^*)(D + 4\epsilon - \rho)\\ &\qquad - (\delta^* - \tau^* + \beta^* + 3\alpha + 4\pi)(\delta - \tau + 4\beta) - 3\Psi_2]\Psi_4^{(P)} = 0\end{aligned} \tag{8.47}$$

The Kerr metric in Boyer-Lindquist coordinates is

$$\begin{aligned}ds^2 = \left(1 - \frac{2Mr}{\Sigma}\right) dt^2 + \frac{4Mr}{\Sigma}\sin^2\theta dt d\phi - \frac{\Sigma}{\Delta}dr^2 - \Sigma d\theta^2\\ - \sin^2\theta\left(r^2 + a^2 + \frac{2Ma^2r}{\Sigma}\sin^2\theta\right) d\phi^2\end{aligned} \tag{8.48}$$

where

$$\Sigma = r^2 + a^2 \cos^2\theta \tag{8.49}$$

$$\Delta = r^2 - 2Mr + a^2 \tag{8.50}$$

Using the Kinnersley tetrad

$$l^i = \left[\frac{(r^2+a^2)}{\Delta}, 1, 0, \frac{a}{\Delta}\right] \tag{8.51}$$

$$n^i = \frac{1}{\Sigma}[r^2+a^2, -\Delta, 0, a] \tag{8.52}$$

$$m^i = \frac{1}{\sqrt{2}(r+ia\cos\theta)}\left[ia\sin\theta, 0, 1, \frac{i}{\sin\theta}\right] \tag{8.53}$$

we can now write the gravitational perturbation equations, eqs. (8.46) and (8.47), in terms of the usual black hole parameters. Teukolsky has presented one master equation for the gravitational perturbations as well the electromagnetic and scalar perturbations:

$$\begin{aligned}&\left[\frac{(r^2+a^2)^2}{\Delta} - a^2\sin^2\theta\right]\partial_{tt}\Psi + \frac{4Mar}{\Delta}\partial_{t\phi}\Psi + \left[\frac{a^2}{\Delta} - \frac{1}{\sin^2\theta}\right]\partial_{\phi\phi}\Psi \\ &- \Delta^{-s}\partial_r(\Delta^{s+1}\partial_r\Psi) - \frac{1}{\sin\theta}\partial_\theta\left(\sin\theta\partial_\theta\Psi\right) - 2s\left[\frac{a(r-M)}{\Delta} + \frac{i\cos\theta}{\sin^2\theta}\right]\partial_\phi\Psi \\ &- 2s\left[\frac{M(r^2-a^2)}{\delta} - r - ia\cos\theta\right]\partial_t\Psi + (s^2 cot^2\theta - s)\Psi = 0\end{aligned} \tag{8.54}$$

For gravitational perturbations, $s = \pm 2$, $\Psi$ represents $\Psi_0^{(P)}$ or $\rho^{-4}\Psi_4^{(P)}$. This is the equation we would like to solve.

## 8.3 A Characteristic Approach to Perturbed Kerr Black Holes

We consider scalar waves in Kerr geometry. This is simpler than solving the gravitational problem, yet we expect the same features to be prominent in both cases and the methods we use may be extended later to solve the gravitational equation. The wave equation is written in Boyer-Lindquist coordinates as

$$\begin{aligned}&-\frac{\Sigma R^2}{\Delta}\partial_{tt}\Psi - \frac{4Mar}{\Delta}\partial_{t\phi}\Psi + \partial_r\left(\Delta\partial_r\Psi\right) \\ &+ \frac{1}{\sin\theta}\partial_\theta\left(\sin\theta\,\partial_\theta\Psi\right) + \left(\frac{1}{\sin^2\theta} - \frac{a^2}{\Delta}\right)\partial_{\phi\phi}\Psi = 0\end{aligned} \tag{8.55}$$

where

$$\Sigma R^2 = (r^2+a^2)^2 - \Delta a^2\sin^2\theta \tag{8.56}$$

We would like to write this as a characteristic initial value problem. Transforming to coordinates $(u_s, r_s, \theta, \phi)$ where $u_s = t - r_s$ is the usual so-called *retarded Kerr time* determined by $\frac{dr_s}{dr} = \frac{r^2 + a^2}{\Delta}$, we immediately encounter a problem - the double $u_s$ derivative does not vanish. This problem is due to the fact that $u_s = const.$ hypersurfaces are spacelike, i.e not lightlike. There has not been much previous investigation of light cones in Kerr geometry. This may stem from a fear that such hypersurfaces would develop caustics due to the twist in the metric. As far as we are aware, Pretorius and Israel are the first to have presented such an investigation [90]. They define *quasi-spherical light cones* which turn out to be free from caustics for all positive values of the radial Kerr coordinate, $r$.

We follow Pretorius & Israel [90] and define coordinates $(u, r_*, lambda, \phi)$ where $r_*$ and $\lambda$ are functions of the Boyer-Lindquist coordinates $r$ and $\theta$. The wave eq. becomes

$$\begin{aligned}
&\left(-\frac{\Sigma R^2}{\Delta} + (\partial_\theta r_*)^2 + \Delta(\partial_r r_*)^2\right)\partial_{uu}\Psi - 2(\Delta(\partial_r r_*)^2 + (\partial_\theta r_*)^2)\partial_{ur}\Psi \\
&+ (\Delta(\partial_r r_*)^2 + (\partial_\theta r_*)^2)\partial_{rr}\Psi + ((\partial_\theta\lambda)^2 + \Delta(\partial_r\lambda)^2)\partial_{\lambda\lambda}\Psi \\
&+ 2(\Delta\partial_r\lambda\partial_r r_* + \partial_\theta\lambda\partial_\theta r_*)(\partial_{r_*\lambda}\Psi - \partial_{u\lambda}\Psi) + \left(\partial_r(\Delta\partial_r r_*) + \frac{1}{\sin\theta}\partial_\theta(\sin\theta\partial_\theta r_*)\right)(\partial_{r_*}\Psi - \partial_u\Psi) \\
&+ \left(\partial_r(\Delta\partial_r\lambda) + \frac{1}{\sin\theta}\partial_\theta(\sin\theta\partial_\theta\lambda)\right)\partial_\lambda\Psi - \frac{4Mar}{\Delta}\partial_{u\phi}\Psi + \left(\frac{1}{\sin^2\theta} - \frac{a^2}{\Delta}\right)\partial_{\phi\phi}\Psi = 0
\end{aligned} \tag{8.57}$$

from which we can see that a characteristic formulation requires

$$\Delta(\partial_r r_*)^2 + (\partial_\theta r_*)^2 = \frac{\Sigma R^2}{\Delta} \tag{8.58}$$

It is possible to obtain a particular separable solution of eq. (8.58) by adding a separation constant, $a^2\lambda$, on both sides.

$$\Delta\left((\partial_r r_*)^2 - \frac{(r^2 + a^2)^2 - a^2\lambda\Delta}{\Delta^2}\right) = \left((\partial_\theta r_*)^2 - a^2(\lambda - \sin^2\theta)\right) \tag{8.59}$$

Defining two new functions

$$P^2(\theta, \lambda) = a^2(\lambda - \sin^2\theta) \tag{8.60}$$

$$Q^2(r, \lambda) = (r^2 + a^2)^2 - a^2\lambda\Delta \tag{8.61}$$

such that

$$Q^2 + \Delta P^2 = \Sigma R^2 \tag{8.62}$$

we find

$$(\partial_r r_*)^2 - \frac{Q^2}{\Delta^2} = -\frac{1}{\Delta}\left((\partial_\theta r_*)^2 - P^2\right) \tag{8.63}$$

which can be satisfied if $\partial_r r_* = \frac{Q}{\Delta}$ and $\partial_\theta r_* = P$. i.e. we can write

$$\begin{aligned} dr_* &= \partial_r r_* dr + \partial_\theta r_* d\theta \\ &= \frac{Q}{\Delta} dr + P d\theta \end{aligned} \tag{8.64}$$

(for fixed $\lambda$).

Integrating this leads to an extra constant which we call $\frac{a^2}{2} f$ i.e.

$$r_* = \int^r \frac{Q}{\Delta} dr + \int^\theta P d\theta + \frac{a^2}{2} f \tag{8.65}$$

We now have a two-parameter family of solutions to eq.(8.58)

$$r_* = r_*(r, \theta; \lambda, f) \tag{8.66}$$

This can be extended to a solution depending on $\lambda$ and an arbitrary function$f(\lambda)$ provided that

$$\partial_\lambda r_* + \frac{df}{d\lambda} \partial_f r_* = 0 \tag{8.67}$$

as explained on p.348 of *Applied PDEs* by Ockendon et al [91]. We can write this condition as

$$-\int^r \frac{1}{Q} dr + \int^\theta \frac{1}{P} d\theta + \partial_\lambda f(\lambda)|_{(r,\theta)} = 0 \tag{8.68}$$

We could have written equation (8.64) as

$$dr_* = \frac{Q}{\Delta} dr + P d\theta + \frac{a^2}{2} F d\lambda \tag{8.69}$$

Then

$$\partial_\lambda r_*|_{(r,\theta)} = \int^r \frac{1}{\Delta} \partial_\lambda Q|_{(r,\theta)} dr + \int^\theta \partial_\lambda P|_{(r,\theta)} d\theta + \frac{a^2}{2} \partial_\lambda f(\lambda)|_{(r,\theta)} \tag{8.70}$$

From eqs. (8.60),(8.61) we find

$$\partial_\lambda Q|_{(r,\theta)} = -\frac{a^2\Delta}{2Q} \tag{8.71}$$

$$\partial_\lambda P|_{(r,\theta)} = \frac{a^2}{2P} \tag{8.72}$$

i.e.

$$\partial_\lambda r_*|_{(r,\theta)} = -\int^r \frac{a^2}{2}\frac{1}{Q}dr + \int^\theta \frac{a^2}{2}\frac{1}{P}d\theta + \frac{a^2}{2}\partial_\lambda f(\lambda)|_{(r,\theta)} \tag{8.73}$$

and

$$F = -\int^r \frac{1}{Q}dr + \int^\theta \frac{1}{P}d\theta + \partial_\lambda f(\lambda)|_{(r,\theta)} \tag{8.74}$$

We can see that for $\lambda$ to be a function of $(r,\theta)$ and for all our equations to be consistent we must have $F = 0$, i.e. $\partial_\lambda r_* = 0$ (the same condition as given by equation (8.67)). In other words $r_*$ and $\lambda$ must be independent variables. We can see immediately that if $F = 0$, then when $\lambda = const.$, i.e. $\partial_\lambda f(\lambda)|_{(r,\theta)} = 0$ we have

$$\left(\frac{d\theta}{dr}\right)_\lambda = \frac{P}{Q} \tag{8.75}$$

which defines the lines of constant $\lambda$, i.e. the null rays. Since $F = 0$, from eq.(8.74) we find

$$dF = -\frac{1}{Q}dr + \frac{1}{P}d\theta + \partial_{\lambda\lambda} f(\lambda)|_{(r,\theta)}d\lambda = 0 \tag{8.76}$$

i.e.

$$\mu d\lambda = -\frac{1}{Q}dr + \frac{1}{P}d\theta \tag{8.77}$$

where we have defined

$$-\partial_{\lambda\lambda} f(\lambda)|_{(r,\theta)} = \mu \tag{8.78}$$

combining this with eq.(8.64) leads to the two important equations

$$\Sigma R^2 dr = \Delta Q(dr_* - \mu P^2 d\lambda) \tag{8.79}$$

$$\Sigma R^2 d\theta = P(\Delta dr_* + \mu Q^2 d\lambda) \tag{8.80}$$

Using eqs.(8.64) and (8.77) we can now work out all of the coefficients in the wave equation, eq.(8.57). We find

$$\begin{aligned}
\partial_r(\Delta\partial_r r_*) + \frac{1}{\sin\theta}\partial_\theta(\sin\theta P) =& \partial_r Q + \partial_\theta P + \frac{\cos\theta}{\sin\theta}P \\
=& \frac{4r}{2Q}(r^2+a^2) - \frac{a^2\lambda}{2Q}(2r-2m) - \frac{a^2\Delta}{2Q}\left(\frac{-1}{\mu Q}\right) \\
&+ \frac{a^2}{2P}\left(\frac{1}{\mu P}\right) - \frac{a^2}{P}\sin\theta\cos\theta + \frac{\cos\theta}{\sin\theta}P \\
\equiv& \frac{2\Sigma R^2}{\Delta}A \qquad (8.81) \\
\Delta(\partial_r\lambda)^2 + (\partial_\theta\lambda)^2 =& \Delta\left(\frac{-1}{\mu Q}\right)^2 + \left(\frac{1}{\mu P}\right)^2 \\
=& \frac{1}{\mu^2}\left(\frac{\Delta P^2 + Q^2}{Q^2P^2}\right) = \frac{\Sigma R^2}{\mu^2 Q^2 P^2} \\
\equiv& \frac{2\Sigma R^2}{\Delta}C \qquad (8.82) \\
\partial_r(\Delta\partial_r\lambda) + \frac{1}{\sin\theta}\partial_\theta(\sin\theta\partial_\theta\lambda) =& -\partial_r\left(\frac{\Delta}{\mu Q}\right) + \frac{1}{\sin\theta}\partial_\theta\left(\frac{\sin\theta}{\mu P}\right) \\
\equiv& \frac{2\Sigma R^2}{\Delta}D \qquad (8.83) \\
\Delta\partial_r r_*\partial_r\lambda + \partial_\theta r_*\partial_\theta\lambda =& \Delta\left(\frac{Q}{\Delta}\right)\left(\frac{-1}{\mu Q}\right) + P\left(\frac{1}{\mu P}\right) = 0 \qquad (8.84)
\end{aligned}$$

When we try to simplify eq.(8.83) further we encounter some serious problems in our attempts to calculate the derivatives of $\mu$. The $r$-derivative is difficult to calculate due to the presence of a second $\lambda$ partial derivative of $F$ (with $r$ and $\theta$ held constant)

$$\begin{aligned}
\partial_r\mu &= \partial_r\mu|_{(\theta,\lambda)} + \partial_r\lambda\partial_\lambda\mu|_{(r,\theta)} \\
&= \frac{a^2\Delta}{2Q^3} + \frac{1}{\mu Q}\partial_{\lambda\lambda}F|_{(r,\theta)} \qquad (8.85)
\end{aligned}$$

The $\theta$ derivative is more difficult. In this case we have

$$\begin{aligned}
\partial_\theta\mu &= \partial_\theta\mu|_{(r,\lambda)} + \partial_\theta\lambda\partial_\lambda\mu|_{(r,\theta)} \\
&= \frac{a^2}{2P^3} - \frac{1}{\mu P}\partial_{\lambda\lambda}F|_{(r,\theta)} \qquad (8.86)
\end{aligned}$$

The term $\frac{a^2}{2P^3}$ becomes singular as $a \to 0$, i.e. in the limit of flat space ($P \to 0$ as $a^2$). At the poles and equator we also have $P \to 0$. When we consider the second term of eq.(8.83) we find

$$\partial_\theta\left(\frac{1}{\mu P}\right) = -\frac{a^2}{\mu^2 P^4} + \frac{a^2}{\mu P^3}\sin\theta\cos\theta + \frac{1}{\mu^3 P^2}\partial_{\lambda\lambda}F|_{(r,\theta)} \tag{8.87}$$

The first two terms on the right hand side become singular in the flat-space limit and the third is unknown.

In order to avoid these problems we can rewrite D in the form:

$$D = \frac{1}{2}\left[\frac{1}{\mu PQ\sin\theta}\partial_\lambda\left(\frac{\Delta\sin\theta}{\mu PQ}\right)\right] \tag{8.88}$$

and calculate the $\lambda$ derivative numerically. This term is included in eq.(51) of [90] but the problem of how to evaluate the derivative is not dealt with by the authors. Our method is to integrate for $\frac{\Delta\sin\theta}{\mu PQ}$ at a small angular distance of $\delta\lambda$ on either side of the gridpoint at which we want to calculate the derivative. We then take the difference and divide by $2\delta\lambda$.

The wave equation can now be written as

$$\begin{aligned}&\partial_{ur_*}\Psi - \frac{1}{2}\partial_{r_*r_*}\Psi - A\left(\partial_{r_*}\Psi - \partial_u\Psi\right)\\&+ B\partial_{u\phi}\Psi - C\partial_{\lambda\lambda}\Psi - D\partial_\lambda\Psi - E\partial_{\phi\phi}\Psi = 0\end{aligned} \tag{8.89}$$

where the coefficients,$B$ and $E$ are given by

$$B = \frac{2Mar}{\Sigma R^2} \tag{8.90}$$

$$E = \frac{\Delta}{2\Sigma R^2}\left(\frac{1}{\sin^2\theta} - \frac{a^2}{\Delta}\right) \tag{8.91}$$

## 8.4 Numerical evolution

We would like to evolve eq.(8.89) numerically. A previously developed Cauchy code exists [2], but has some late-time convergence problems and according to the results of Krivan [92] it produces unexpectedly fast fall-off at late times. Here I focus on developing a characteristic evolution with the aim of obtaining more dependable late-time results while still retaining the simplicity of a linearized perturbation approach.

### *8.4.1 $\phi$-dependence*

In my treatment of the three-dimensional flat-space wave equation I have assumed axisymmetry with a $\phi$-dependence of $e^{im\phi}$. Kerr spacetime is also axisymmetric, however the Boyer-Lindquist coordinate, $\phi$, is defined by asymptotic observers and this coordinate system winds itself infinitely many times around the black hole, leading to problems. Initial attempts to evolve the scalar wave equation in Kerr spacetime using an azimuthal decomposition of $e^{im\phi}$ showed problems and instability at negative $r_*$. This problem was pointed out in [2] which includes an appendix showing how this problem manifests in the slow-rotation limit. Following [2] we use the Kerr azimuthal coordinate, $\tilde{\phi}$, given by

$$d\tilde{\phi} = d\phi + \frac{a}{\Delta} dr \tag{8.92}$$

### *8.4.2 Compactification*

In order to avoid problems with setting artificial boundary conditions and in order to evolve all the way out to future null infinity we compactify the radial coordinate by transforming to a new coordinate, $x$, given by

$$x = \tan^{-1}(f r_*) \tag{8.93}$$

where $f$ is chosen to give compactification to future null infinity but also to give the required resoluton near the potential peak and the intial data (which is of compact support). I have chosen to use $f = 0.0017$ as this pushes the compactification to sufficiently large $r$ (see Fig. 6.15 in Chapter 6). The relevant transformations are

$$\partial_{r_*}\Psi \rightarrow \alpha \partial_x \Psi \tag{8.94}$$

$$\partial_{r_* r_*}\Psi \rightarrow \alpha^2 \partial_{xx}\Psi - 2r_* f \alpha^2 \partial_x \Psi \tag{8.95}$$

where

$$\alpha = \frac{f}{1 + f^2 r_*^2} \tag{8.96}$$

### *8.4.3 Transforming the Angular Coordinate*

We choose to work with the angular coordinate $\theta_*$ which is related to $\lambda$ via

$$\lambda = \sin^2 \theta_* \tag{8.97}$$

As shown by Pretorius and Israel [90], this $\theta_*$ becomes the spherical polar coordinate $\theta$ asymptotically, i.e. in the flat space limit. The transformations from $\lambda$ to $\theta_*$ in our scalar wave equation are given by

$$\partial_\lambda \Psi \rightarrow \frac{1}{2\sqrt{\lambda(1-\lambda)}} \partial_{\theta_*}\Psi \tag{8.98}$$

$$\partial_{\lambda\lambda}\Psi \rightarrow \frac{1}{4\lambda(1-\lambda)} \partial_{\theta_*\theta_*}\Psi + \frac{2\lambda - 1}{4(\lambda(1-\lambda))^{3/2}} \partial_{\theta_*}\Psi \tag{8.99}$$

With these transformations, $(u, r_*, \lambda, \phi) \rightarrow (u, x, \theta_*, \tilde{\phi})$, the wave equation (8.89) becomes

$$
\begin{aligned}
&\alpha \partial_{ux}\Psi - \frac{1}{2}\alpha^2 \partial_{xx}\Psi - \left[\left(A + iam\frac{Q}{\Sigma R^2}\right)\alpha - r_* f \alpha^2\right]\partial_x \Psi \\
&+ \left[A + iam\frac{Q}{\Sigma R^2} + Bim\right]\partial_u \Psi - \frac{C}{4\sin^2\theta_* \cos^2\theta_*}\partial_{\theta_*\theta_*}\Psi \\
&- \left(\frac{D}{2\sin\theta_*\cos\theta_*} + \frac{C(2\sin^2\theta_* - 1)}{4\sin^3\theta_*\cos^3\theta_*} - i\frac{amP\Delta}{2\sin\theta_*\cos\theta_*(\mu P)Q\Sigma R^2}\right)\partial_{\theta_*}\Psi \\
&+ \frac{m^2\Delta}{2\sin^2\theta \Sigma R^2}\Psi = 0
\end{aligned}
\tag{8.100}
$$

### 8.4.4 *Setting Up the Grid*

We set up a numerical grid using the coordinates $(x(r_*), \theta_*)$. The value of $r_*$ can be calculated at each gridpoint as

$$r_* = \frac{\tan x}{f} \tag{8.101}$$

At each grid-point we must know the corresponding value of $r$, $\theta$ and $\mu$ in order to calculate the coefficients of the wave equation. To find these values we solve coupled differential equations along surfaces of constant $\lambda$ using a fourth-order Runge-Kutta scheme, with initial values approximated for large $r$.

I encountered many difficulties in this section. In particular I found that it was also necessary to integrate for $\Delta$ along the null generators because near the horizon it is not possible to calculate $\Delta$ numerically with the required precision from the value of $r$. It was also necessary to integrate for $\mu P$ rather than $\mu$ alone because the derivative of $\mu$ along the generators is not well behaved in the flat-space limit whereas $\mu P$ remains finite. There were also problems in calculating $P$ to the required precision when the difference between $\lambda$ and $\sin^2\theta$ becomes too small. I have therefore integrated for $P$ also.

I have chosen to integrate in $r_*$ for simplicity. The relevant equations are

$$
\begin{aligned}
(\partial_{r_*} r)_\lambda =& \frac{\Delta Q}{\Sigma R^2} && (8.102)\\
(\partial_{r_*} \theta)_\lambda =& \frac{\Delta P}{\Sigma R^2} && (8.103)\\
(\partial_{r_*} \mu)_\lambda =& \frac{a^2\Delta}{2PQ^2} - \frac{a^2\Delta}{PQ^2\Sigma R^2}\mu Q^2 \sin\theta\cos\theta && (8.104)\\
(\partial_{r_*} \Delta)_\lambda =& 2(r - M)\left(\partial_{r_*} r\right)_\lambda && (8.105)\\
(\partial_{r_*} P)_\lambda =& -a^2 \sin 2\theta \left(\partial_{r_*}\theta\right)_\lambda && (8.106)
\end{aligned}
$$

When setting up our grid we make use of the condition that

$$\theta_*(r = \infty) = \theta \tag{8.107}$$

We can therefore approximate our initial values at large $r$ by using asymptotic expansions and exploiting the fact that we expect $\theta - \theta_*$ to be small for large $r$. The resulting approximations are

$$r_* \approx r + 2Mln(r) + \frac{a^2\sin^2(\theta_*)}{2r} - \frac{4M^2}{r} \tag{8.108}$$

$$\theta \approx \theta_* - \frac{a^2\sin(2\theta_*)}{4r^2} \tag{8.109}$$

$$\mu P \approx \frac{1}{2\sin\theta_*\cos\theta_*} + \frac{(2-\sin^2\theta_*)a^2}{4\sin\theta_*\cos\theta_* r^2} \tag{8.110}$$

$$\Delta = r^2 - 2Mr + a^2 \tag{8.111}$$

$$P^2 \approx \frac{a^4}{r^2}\sin^2\theta_*\cos^2\theta_* + \frac{a^6}{4r^4}(\sin^4\theta_*\cos^2\theta_* - \cos^4\theta_*\sin^2\theta_*) \tag{8.112}$$

These approximations give us starting values or $r, \theta, \Delta, \mu P$ and $P$ so that we can shoot along the negative $r_*$ direction to find the values at other points on the grid.

There is a slight complication in the quadrant from $\theta = \pi/2$ to $\theta = \pi$ because P is antisymmetric. This is not a problem here because eqs.(8.108-8.112) are still valid in this quadrant as long as we remember to take the negative square root of $P^2$ in this quadrant.

Fig. 8.1 shows how $\theta$ varies with $r_*$ along lines of constant $\theta_*$. Over most of the grid the null generators look like lines of $\theta = const.$ however we can see a sharp twisting of the null generators occurring near $r_* = 0$.

### *8.4.5 Finite Difference Equations*

We write our derivatives in finite difference form using the same scheme described for the axisymmetric wave equation in flat space. This results in the equation

$$\begin{aligned} c1p_{i,j}^{n+1} =& c2p_{i-1,j}^{n+1} + c3(p_{i-2,j}^{n+1} + p_{i+1,j}^{n}) + c4p_{i,j}^{n} + c5p_{i-1,j}^{n} \\ &+ c6(p_{i-1,j+1}^{n+1} + p_{i,j+1}^{n}) + c7(p_{i-1,j-1}^{n+1} + p_{i,j-1}^{n}) \end{aligned} \tag{8.113}$$

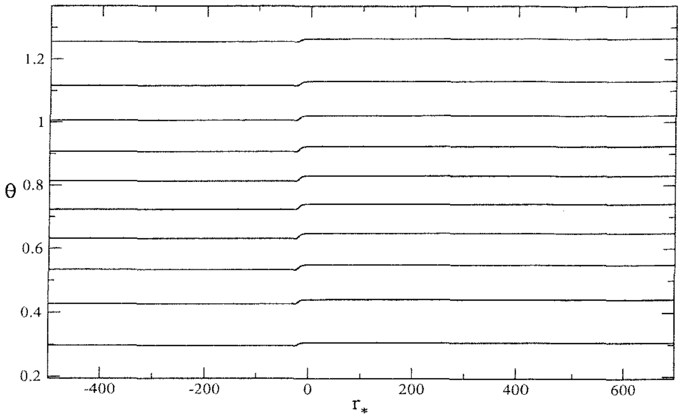

Figure 8.1: A plot $\theta$ vs $r_*$ for lines of constant $\theta_*$ in an extreme Kerr black hole. These lines are null generators for Kerr spacetime. A sharp twisting is visible near $r_* = 0$, the approximate position of the peak of the potential in the corresponding Schwarzschild problem.

The coefficients are calculated at position $r_*(i - 1/2, j)$ and are given by

$$c1 = \frac{\alpha}{\delta x \delta u} - \frac{\alpha^2}{4\delta x^2} - \frac{\alpha(A + imF)}{2\delta x} + \frac{A + im(F + B)}{2\delta u} + \frac{r_* f \alpha^2}{2\delta x} \tag{8.114}$$

$$\begin{aligned} c2 =& \frac{\alpha}{\delta x \delta u} - \frac{\alpha^2}{2\delta x^2} - \frac{\alpha(A + imF)}{2\delta x} - \frac{A + im(F + B)}{2\delta u} \\ &- \frac{C}{4\sin^2\theta_* \cos^2\theta_* \delta\theta_*^2} + \frac{r_* f \alpha^2}{2\delta x} - \frac{m^2 H}{2} \end{aligned} \tag{8.115}$$

$$c3 = \frac{\alpha^2}{4\delta x^2} \tag{8.116}$$

$$\begin{aligned} c4 =& \frac{\alpha}{\delta x \delta u} - \frac{\alpha^2}{2\delta x^2} + \frac{\alpha(A + imF)}{2\delta x} + \frac{A + im(F + B)}{2\delta u} \\ &- \frac{C}{4\sin^2\theta_* \cos^2\theta_* \delta\theta_*^2} - \frac{r_* f \alpha^2}{2\delta x} - \frac{m^2 H}{2} \end{aligned} \tag{8.117}$$

$$c5 = -\frac{\alpha}{\delta x \delta u} + \frac{\alpha^2}{4\delta x^2} - \frac{\alpha(A + imF)}{2\delta x} + \frac{A + im(F + B)}{2\delta u} + \frac{r_* f \alpha^2}{2\delta x} \tag{8.118}$$

$$c6 = \frac{C(2\lambda - 1)}{16\sin^3\theta_* \cos^3\theta_* \delta\theta_*} + \frac{C}{8\sin^2\theta_* \cos^2\theta_* \delta\theta_*^2} + \frac{D}{8\sin\theta_* \cos\theta_* \delta\theta_*} + \frac{imG}{4\delta\theta_*} \tag{8.119}$$

$$c7 = -\frac{C(2\lambda - 1)}{16\sin^3\theta_* \cos^3\theta_* \delta\theta_*} + \frac{C}{8\sin^2\theta_* \cos^2\theta_* \delta\theta_*^2} - \frac{D}{8\sin\theta_* \cos\theta_* \delta\theta_*} - \frac{imG}{4\delta\theta_*} \tag{8.120}$$

where we have used the substitutions

$$F = \frac{aQ}{\Sigma R^2} \tag{8.121}$$

$$G = -\frac{a\Delta}{2\mu Q \Sigma R^2 \sin\theta_* \cos\theta_*} \tag{8.122}$$

$$H = \frac{\Delta}{2\Sigma R^2 \sin^2\theta} \tag{8.123}$$

Near the horizon, at the inner boundary point I impose a zero boundary condition. This is not the physical condition, which is more closely approximated using an ingoing radiation condition but I avoid the problem altogether by pushing the boundary nearer the horizon, so that the pulse does not reach it even by the end of the evolutions. Later, this problem could be fixed by using characteristic-characteristic matching.

The first inner point and the outer boundary point are treated in a similar manner to that described for the 2d scalar wave equation in flat space. For the first point in we use

$$\partial_{xx}\Psi^{n+\frac{1}{2}}_{i-\frac{1}{2},j} = \frac{1}{2\Delta x^2}(3p^n_{i-1,j} - 7p^n_{i,j} + 5p^n_{i+1,j} - p^n_{i+2,j}) \tag{8.124}$$

and at the last point we use

$$\partial_{xx}\Psi^{n+\frac{1}{2}}_{i-\frac{1}{2},j} = \frac{1}{2\Delta x^2}(p^{n+1}_{i,j} - 2p^{n+1}_{i-1,j} + p^{n+1}_{i-2,j} + 2p^n_{i,j} - 5p^n_{i-1,j} + 4p^n_{i-2,j} - p^n_{i-3,j}) \tag{8.125}$$

The resulting finite difference equations at these points are similar in form to eq. (8.113) with some new terms and the coefficients slightly altered.

Another complication in moving from the flat space wave equation to the wave equation in Kerr spacetime is that we now have to deal with complex coefficients. This means that we have to treat the real and imaginary parts of the scalar $\Psi$ separately and we end up with coupled evolution equations. In other words we take the real part and the imaginary part of eq. (8.113) as two coupled equations. There are many equations to calculate at each time step but the coefficients are independent of $u$ and need only be calculated once, before the beginning of the evolution.

### *8.4.6 Initial Data*

I prescribe initial data on $u_0$ as

$$\Psi(r_*, \lambda) = G(r_*)P^m_l(\cos\theta) \tag{8.126}$$

where $G(r_*)$ is a Gaussian pulse, $e^{-b(r_*-r^0_*)}$, with width $b$ and peak at $r^0_*$, and $P^m_l(\cos\theta)$ is a particular associated Legendre function. Although we write the initial data in this way, as we have done previously, the evolution equation does not decouple in $P_{lm}$s and we therefore expect to see coupling of many multipoles in the evolution.

### *8.4.7 Results*

The scheme I have described above seems to have some stability problems but the stability improves with increased resolution in the radial direction. Fig. 8.2 shows how the results improve for radial resolutions of 2500, 5000 and 10000 gridpoints with $m = l = 2$ initial data. Fig. 8.3 shows the results of convergence testing and we can see that the scheme is second order convergent in $x$. The instability does not seem to be affected by the Courant factor but I have not been able to run the code for a very low Courant factor due to computational limitations. The instability seems to happen first near $x = 0$ and this is the position at which the Courant condition is severe because the stepsize in $r_*$ is least there. A full stability analysis would be complicated but, by comparison to the flat space problem of Chapter 7 where we found an instability at the origin, we might expect that there could be problems at $r_* = 0$.

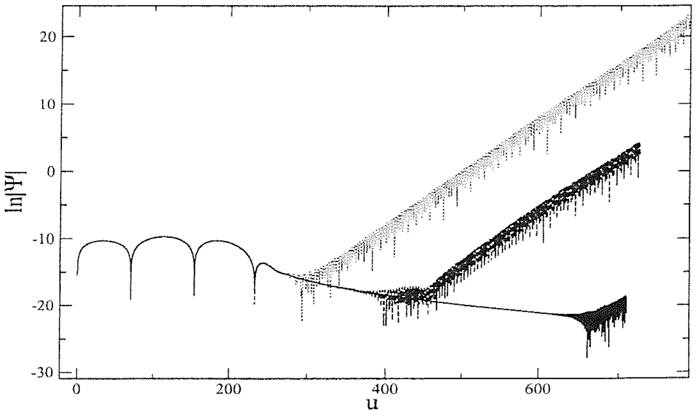

Figure 8.2: Results of the characteristic evolution for scalar waves in Kerr spacetime showing runs of successively higher resolution. Dotted line: 2500 gridpoints, dashed line: 5000 gridpoints, solid line: 10000 gridpoints. It is clear that the code remains stable for much longer with higher resolution runs.

In order to eliminate possible causes of the instability I have tested the set-up of the $(r_*, \theta_*)$ grid by performing a Cauchy evolution using the new grid, i.e. using coordinates $(t, r_*, \theta_*, \tilde{\phi})$. The wave equation in these coordinates, assuming $e^{im\tilde{\phi}}$

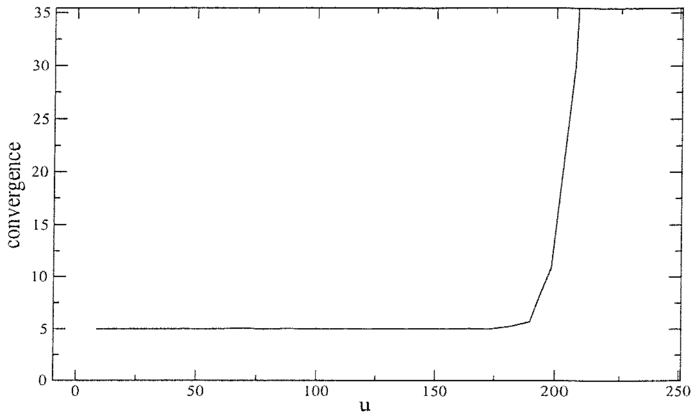

Figure 8.3: Convergence results for the characteristic evolution of the scalar wave equation in Kerr spacetime. The convergence test was carried out using runs with radial resolutions of 2500, 5000 and 10,000 gridpoints. The angular resolution is kept constant with 15 gridpoints. The code is second order convergent up until the time at which the instability begins in the lower resolution run.

dependence, is

$$
\begin{aligned}
&-\partial_{tt}\Psi + \partial_{r_* r_*}\Psi - 2Bim\partial_{t\tilde{\phi}}\Psi + (2A + imF)(\partial_{r_*}\Psi - \partial_u\Psi) + \frac{C}{2\sin^2\theta_*\cos^2\theta_*}\partial_{\theta_*\theta_*}\Psi \\
&-\left(\frac{D}{\sin\theta_*\cos\theta_*} + \frac{2C(2\sin^2\theta_* - 1)}{\sin^3\theta_*\cos^3\theta_*} - i\frac{amP\Delta}{\sin\theta_*\cos\theta_*(\mu P)Q\Sigma R^2}\right)\partial_{\theta_*}\Psi + \frac{m^2\Delta}{\sin^2\Sigma R^2}\Psi = 0
\end{aligned}
\tag{8.127}
$$

I have evolved this equation by making some adjustment to the old code [2] for the new coordinates. The results of this compare well with the old code, giving almost identical results, with the same quasinormal mode frequency and late-time fall-off. That the results for both coordinate sets compare well shows that we have successfully been able to calculate the coordinate values we require in the coefficients of the wave equation.

In Kerr spacetime, the radial coordinate goes not only through zero but extends to $-\infty$. This does not cause a problem in a 1-dimensional code such as the Schwarzschild example given in section 6.4.4 of this thesis, but leads to numerical difficulties in 2-dimensions. Perhaps we require an alternative finite difference scheme but my results show that there is a good possibility that with sufficient computing power this code could produce results into the late times that we are interested in.

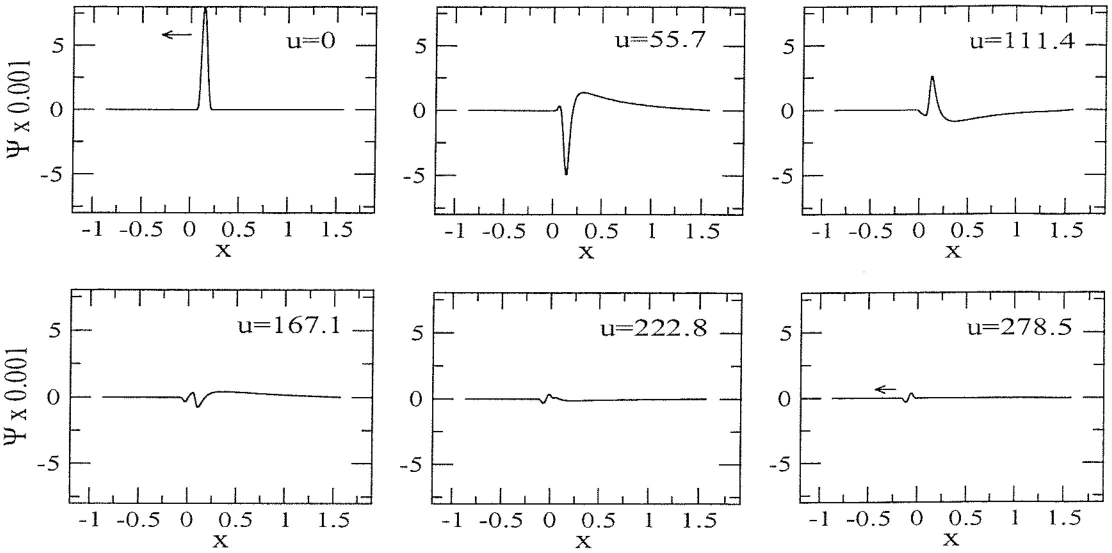

Figure 8.4: Real part of the solution from the null-timelike Kerr code on a $\theta_* =$ *const.* surface on surfaces of $u =$ *const.* The results are exactly as we would expect, before the instability appears. The reflected radiation travels immediately off the grid and the part of the pulse which passes through the potential continues to travel inwards.

### *8.4.8 Characteristic-characteristic Matching*

Ideally we would like to match the characteristic code in outgoing null coordinates to a compactified ingoing characteristic code near the horizon. In this way we could evolve the entire exterior spacetime of the black hole. If the stability issues discussed above can be resolved, the c2m matching scheme used in chapter 6 could easily be extended to two dimensions for an axisymmetric code.

### *8.4.9 Cauchy-characteristic matching (Ccm)*

Although the null-timelike formulation of the scalar wave equation in Kerr spacetime presented here may not be as useful as we had hoped for evolving over the entire exterior spacetime, perhaps it may still be used away from the origin ($r_* = 0$). It may be possible to match a null-timelike segment to the outer boundary of a Cauchy evolution. The Cauchy and characteristic sections are both already operational and therefore only a matching is required. Both segments use identical angular coordinates and the same quantity is being evolved. The radial coordinates of the segments are different because we use compactification in the outer segment,

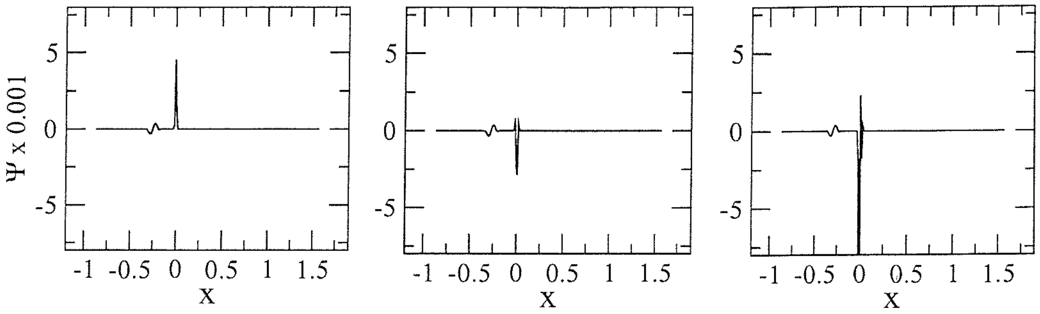

Figure 8.5: The appearance of an instability near $r_* = 0$ in the null-timelike Kerr code shown for $\theta_* = const.$ on surfaces of $u = const.$. The instability is centered near to $r_* = 0$ and grows very quickly.

however we know the analytic relation between the two coordinates. These features make the matching quite straightforward compared to the difficulties of Ccm in full numerical relativity. It should be possible to use the matching scheme described in [93]. This matching scheme involves interpolation between timeslices to obtain the solution at a ghost point of the null surfaces and between null surfaces and thus to obtain the solution at the outer boundary of the Cauchy surfaces . This method has been used successfully in spherical symmetry [94] and cylindrical symmetry [95] but has yet to be used successfully in axisymmetry. In order to take advantage of compactification near the horizon, the inner boundary of the Cauchy region could also be matched to a compactified ingoing null section and thus the entire exterior region may be evolved.

### 8.4.10 Double-null Evolution

The wave eq. in Kerr spacetime may also be written in double-null coordinates $(u, v, \theta_*)$. Assuming an azimuthal dependence of $e^{im\tilde{\phi}}$ the wave equation in these coordinates is

$$\begin{aligned}
&-4\partial_{uv}\Psi + \left[2A + \frac{2ima}{\Sigma R^2}(Q - 2Mr)\right]\partial_v\Psi - \left[2A + \frac{2ima}{\Sigma R^2}(Q + 2Mr)\right]\partial_u\Psi \\
&+ \frac{C}{2\sin^2\theta_*\cos^2\theta_*}\partial_{\theta_*\theta_*}\Psi \\
&- \left(\frac{D}{\sin\theta_*\cos\theta_*} + \frac{2C(2\sin^2\theta_* - 1)}{2\sin^3\theta_*\cos^3\theta_*} - i\frac{amP\Delta}{2\sin\theta_*\cos\theta_*(\mu P)Q\Sigma R^2}\right)\partial_{\theta_*}\Psi + \frac{m^2\Delta}{\sin^2\Sigma R^2}\Psi = 0
\end{aligned} \tag{8.128}$$

I have calculated the derivatives in $u$ and $v$ using the same finite difference scheme as for the one-dimensional wave equation and Regge-Wheeler equation, and used the finite difference forms of the $\theta_*$ derivatives as in eqs. (7.57) and (7.58) for the axisymmetric wave equation. Unfortunately this code is unstable. The double-null evolution has proven to be highly effective in solving 1D problems, therefore a stable evolution in Kerr spacetime is highly desirable but at this stage no such scheme is apparent.

## 8.5 The $m = 0$, $l = 4$ debate

The results of [2] indicate that the late-time behaviour of a perturbed scalar field in Kerr spacetime is determined by the lowest allowed multipole, $l > m$, which fits the symmetries of the initial data. The falloff of the dominant multipole is given by

$$|\Psi| \propto t^{-(2l+3)} \tag{8.129}$$

An analysis in the time domain by Barack and Ori [96] led them to present the late-time falloff at future timelike infinity as

$$|\Psi| \propto t^{-l-|m|-3-q} \tag{8.130}$$

where $q = 0$ if $l + m$ is even and $q = 1$ otherwise, but this result applies only when the $l = 0$ mode is present in the initial data.

Hod's analysis [97] in the frequency domain led him to the result that the late-time behaviour is dominated by the multipole $l = |m|$ if $l^* - |m|$ (where $l^*$ is the multipole of the initial data) is even and $l = |m| + 1$ otherwise. Hod predicts a late-time falloff of

$$\Psi \propto t^{-l^*-|m|-p-1} \qquad \text{if } l^* \geq |m| + 2 \tag{8.131}$$

$$\Psi \propto t^{-2l^*-3} \qquad \text{if } l^* = |m|, |m| + 1 \tag{8.132}$$

where $p = 0$ if $l^* - |m|$ is even and $p = 1$ otherwise.

Considering, for example, initial data of the form $m = 0$, $l^* = 4$, Hod's result predicts a falloff of $|\Psi| \propto t^{-5}$ at late times whereas Barack and Ori predict the more intuitive $|\Psi| \propto t^{-3}$. Krivan [92] used the Cauchy code of [2] to check these analytic prediction. He showed that there is indeed a transistion to the $l = 0$ mode but that the decay is given by the power law, $t^{-6.04}$ which does not agree with either of the analytic predictions. He suggests that this is likely to be a numerical artifact and confirms this by showing how the decay rate decreases with improved grid resolution. His final result of $t^{-5.5}$ still does not agree well with either prediction but is closer to that of Hod. This could be due to the fact that he reads off the decay rate between $t = 600$ and $t = 800$ which may be too early to properly represent to true late-time behaviour. He concludes that "an extension of the existing analytic and numerical studies is necessary."

Poisson [98] provided a possible solution to this problem of contradictory predictions with an extended and generalised formulation of Price's falloff theorem [47]. He concludes that the late-time behaviour of the scalar field is identical to what it would be in spherically symmetric spacetime. He explains the apparent contradictions as an artifact of the different coordinate systems used. The Kerr metric in Boyer-Lindquist coordinates does not reduce to the Minkowski metric in spherical polar coordinates $(r, \theta, \phi)$ in the limit as $M \to 0$. Instead it gives the Minkowski metric in spheroidal coordinates defined by $x = \sqrt{\hat{r}^2 + e^2} \sin\hat{\theta} \cos\phi$, $y = \sqrt{\hat{r}^2 + e^2} \sin\hat{\theta} \sin\phi$ where $e = J/M$ and $J$ is the total angular momentum. In order to compare the results of Hod with the results of Poisson we must transform from spherical coordinates to the spheroidal coordinates $(\hat{r}, \hat{\theta}, \phi)$. Poisson shows in this way that there is actually no contradiction between the results of Hod and the generalised Price theorem. This still does not explain the discrepancy between the results of Hod and Krivan as both involve initial data written in terms of Boyer-Lindquist coordinates.

Burko and Khanna [99] later argued however that Poisson is not correct to ignore the near field geometry in his analysis. They use a penetrating Teukolsky code which evolves the Teukolsky equation for linearized perturbations in ingoing Kerr coordinates $(\tilde{t}, r, \theta, \tilde{\phi})$. In these coordinates the Teukolsky equation has no singularity at the event horizon. They find a late-time falloff of $t^{-3}$. Their explanation for the discrepancy of Hod is that the excitation of dominating modes which are not present in the initial data is nonlinear in the gravitational potentials and is strongest at the near zone. Hod considered only leading order terms in $\omega$ and Burko and Khanna suggest that such selection will limit the excitation of the truly dominating modes. They claim that for the contested example of $m = 0, l^* = 4$ initial data, an analysis to leading order in $\omega$ could excite the $l = 1$ mode but not the $l = 0$ mode. They argue further that Poisson's large-$r$ approximation and Hod's small $\omega$ approach are equivalent.

Burko and Khanna explain the result of Krivan as an effect due to the fact that Krivan considers such a high angular momentum, $a/M = 0.9999$, in his evolutions. Such a high spin slows down the decay rate of the quasi-normal modes, requiring longer evolution times to obtain the true late-time behaviour. Another possible explanation is that Krivan's initial data is purely outgoing and is positioned quite far from the near zone. This severely limits the amplitude at which the $l = 0$ mode can become excited. They predict that the true late-time behaviour will be seen at later times than Krivan has considered. They finally conclude that a fully nonlinear solution will give simpler results than theirs as $m$ will no longer be conserved and the actual decay rate will be of the form $t^{-2|s|+3}$.

Scheel et al [100] contribute to the debate with a 3 + 1 spectral evolution code. They compare results from initial data in Kerr-Schild coordinates and Boyer-Lindquist coordinates and find that, whereas the behaviour at intermediate times is quite different, both cases possess the same late-time power law decay. The differences at intermediate times are due to different magnitudes of excitation of lower-order spherical harmonics. That the falloff at late times is the same for both sets of initial data suggests that Poisson's result is not applicable at late times because it does not take into account the effect of mode mixing in the strong field of the near zone.

So far there has been no conclusive explanation for Krivan's unexpected result. I have carried out a similar evolution using the old Cauchy code of [2] with initial data of the form $m = 0, l = 4$ and I calculate a late time falloff of $t^{-3}$. I have used initial data which is purely ingoing as well as initial data which is purely outgoing and I have placed a broad initial pulse far from the near zone but I have been unable to reproduce the $t^{-5.5}$ result of Krivan. The results are shown in Fig. 8.6. The late time tails of the ingoing and outgoing pulse have the same $t^{-3}$ fall off.

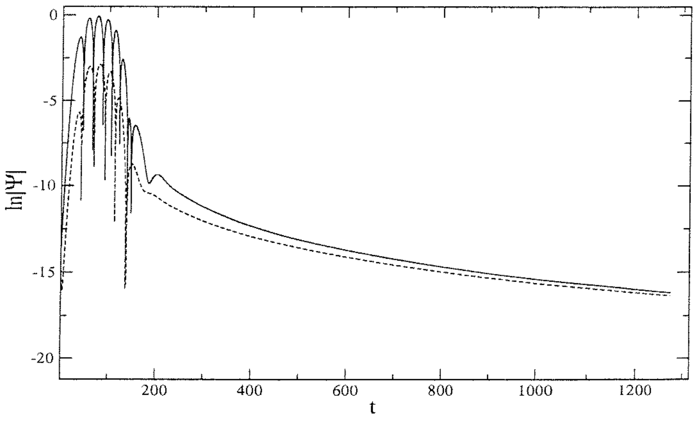

Figure 8.6: Late time tails for $m = 0, l = 4$ initial data. The solid line shows the log of the solution for an ingoing pulse, and the dashed line show the same for an outgoing pulse. The results show the same $t^{-3}$ late time behaviour for both cases.

I have also used the new Cauchy code in $(t, r_*, \theta_*)$ coordinates. The results are compared with those in standard Boyer-Linquist coordinates in Fig. 8.7. It is clear from these results that the late time tail in Kerr spacetime for $m = 0$, $l = 4$ initial data behaves as $t^{-3}$.

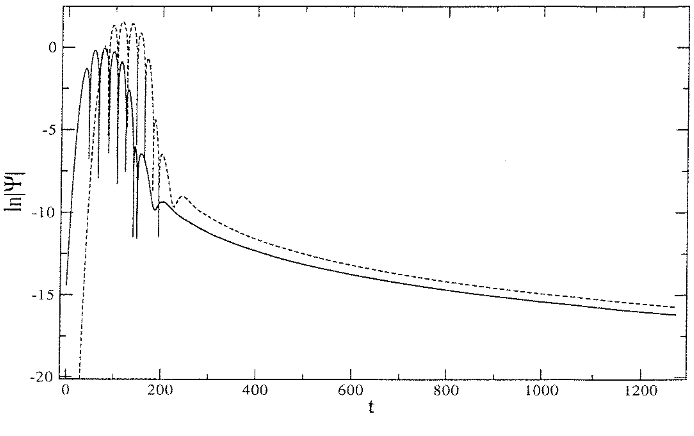

Figure 8.7: Late time tails for $m = 0, l = 4$ initial data. The solid line shows the log of the solution from the evolution using $(r_*, \theta_*)$ coordinates, the dashed lineshows the log of the solution from the evolution using the usual $(r_s, \theta)$ coordinates. The results show the same $t^{-3}$ late time behaviour for both cases

## 8.6 Evidence for a Superradiance Resonance Cavity

Perturbations in Kerr spacetime are expected to generate long lived quasi-normal modes [57]. Recently, Andersson and Glampedakis [51] have argued that unfortunately (from the point of view of detection) the amplitude of each long-lived mode should vanish in the limit $a \longrightarrow M$ because longer-lived modes are more difficult to excite. This argument is supported by their analytic calculations based on several simplifying assumptions, and by the results of Ferrari and Mashoon [101]. Despite the vanishing amplitude for such modes at the extreme limit, they also argue that a large number of very small amplitude modes could interfere constructively to give a considerable signal at late times. If this happens, as their calculations predict, the long-lived modes could completely dominate the late-time behaviour with oscillations of decaying amplitude at the rate $\frac{1}{t}$.

In order to achieve their analytic results, Andersson and Glampedakis use many simplifying approximations and therefore an alternative confirmation is required. They use the Cauchy evolution code of Krivan *et al*[2] for this purpose. They do indeed find an oscillating late-time tail with a fall-off of $\frac{1}{t}$ for extreme Kerr black holes with initial data of type $m \neq 0$, but they warn that the results of the numerical code may also not be trustworthy. They offer the physical interpretation of this phenomenon that, for frequencies close to the upper limit of the superradiant regime, there will be a peak in the (frequency dependent) effective potential just outside the black hole. Waves which "emerge from the horizon" according to a distant observer can now become trapped near the horizon by the potential peak. Waves in such a *superradiance resonance cavity* could experience a kind of parametric amplification and leak out through the horizon to infinity.

During the course of my research using the Cauchy code of [2] I have observed an amplification of the solution at negative $r_*$ in some cases. This can been seen by viewing the solution as a time-evolution on slice of constant $\theta$ as shown in Fig. 8.8. I have also observed some modes leaking out from near the horizon at late times. Fig. 8.9 shows the long-lived quasinormal modes for initial data consisting of a sharp Gaussian of width, $b = 0.13$ (see eq. (8.126)). As the initial pulse becomes wider the time at which the long-lived quasinormal modes appear becomes later. This is shown in Fig. 8.10 for near extreme black holes and Fig. 8.11 for black holes with $a = 0.6$. These results support the superradiance resonance cavity interpretation. The modes which appear at late times can be seen to appear first near the horizon and then leak out through the effective potential to infinity. Whereas this behaviour was observed only for extreme and near extreme black holes by Andersson and Glampedakis , my results indicate that the presence of a superradiance resonance cavity may lead to similar results for non-extreme Kerr black holes.

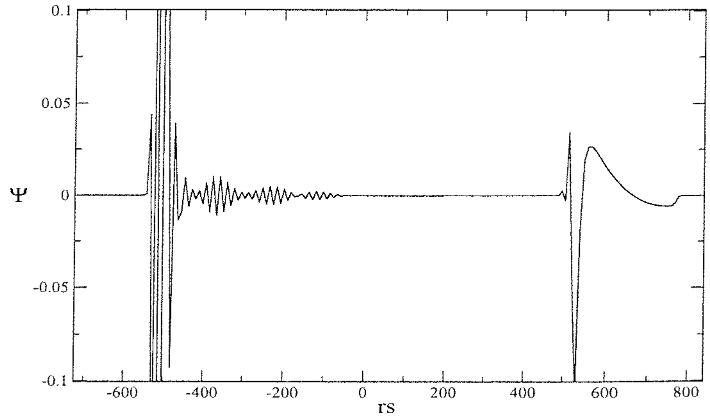

Figure 8.8: Evidence for a superradiant resonance cavity. The real part of the solution in the Cauchy evolution is shown on a surface of constant $\theta$ at time $t = 646$. The growth of the solution at negative $r_*$ supports the interpretation of a superradiant resonance cavity between the horizon and the potential peak.

## 8.7 Chapter Summary

In this chapter I have developed a numerical code for the characteristic evolution of perturbations in Kerr spacetime. The characteristic approach has proven to be very effective in the Schwarzschild case but this is the first such evolution code for perturbations in Kerr. There were several technical difficulties involved in the development of this code but the results show that the code can be stable for

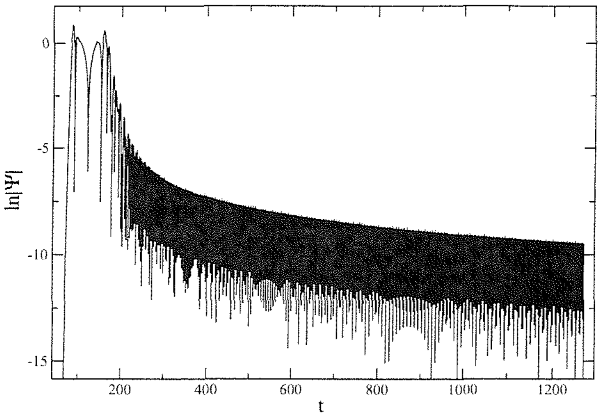

Figure 8.9: The long-lived quasinormal modes from narrow initial pulse in near extreme Kerr black hole. The log of the real part of the solution in Cauchy evolution is shown for $a = 0.999$ and $m = 2$ initial data with Gaussian pulse of width $b = 0.13$. This is similar to the figures of Andersson and Glampedakis.

some time, and that the duration of the stable solution is significant increased with increasing grid resolution in the radial direction. During this time of stability the code is second order convergent.

I have also used the old Cauchy code to obtain results for the late-time behaviour of scalar field perturbations in Kerr spacetime with initial data of the form $m = 0$, $l = 4$. There has been some debate in the literature recently over what form the late-time fall off should take. I have obtained the intuitive result, $t^{-3}$, which disagrees with the results of Krivan but agrees with others.

Finally, I have used the old Cauchy code to support the superradiance resonance cavity interpretation of Andersson and Glampedakis and obtained the surprising result that even for black holes of low angular momentum ($a = 0.6$) the late-time quasinormal modes appear in the evolutions for narrow initial data. I have shown that the time at which these modes appear depends upon the width of the initial pulse.

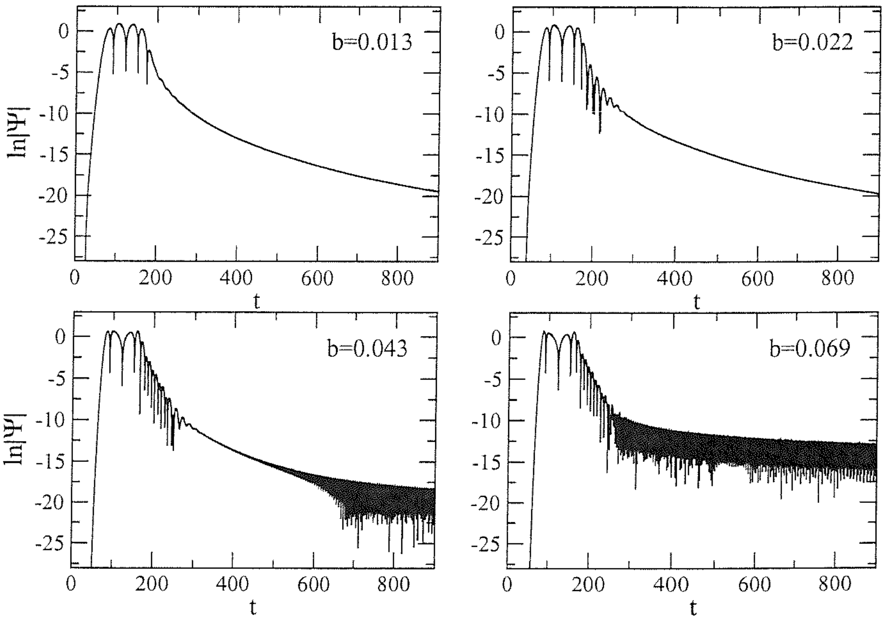

Figure 8.10: Long-lived quasinormal modes for $a = 0.999$ with varying width of initial pulse. The log of the real part of the solution is shown for the Cauchy evolution of a black hole with $a = 0.999$ and $m = 2$ initial data with an initial Gaussian pulse of varying width. As the width is decreased, modes begin to appear at earlier times until, for very narrow initial data the results of Andersson and Glampedakis are reproduced.

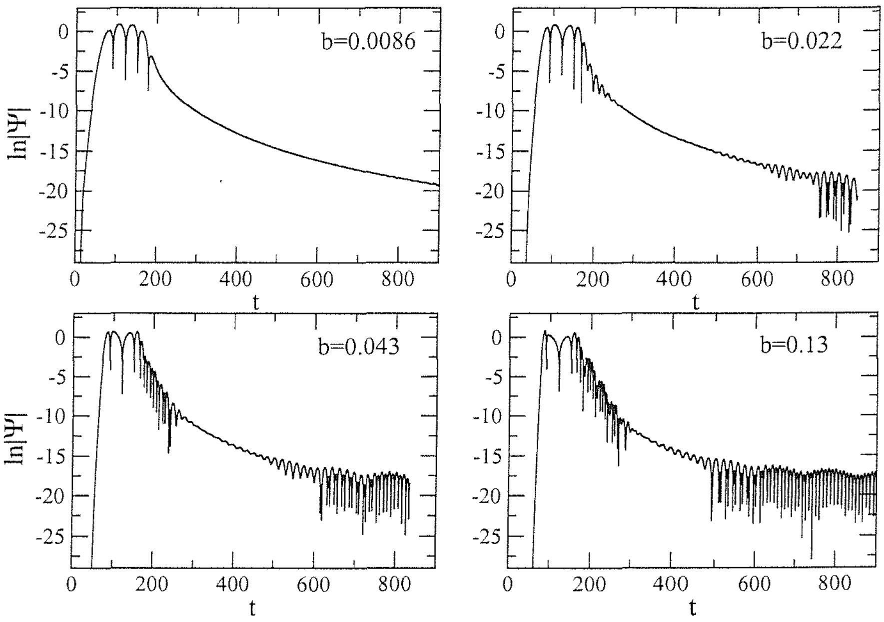

Figure 8.11: Long-lived quasinormal modes for $a = 0.6$ with varying width of initial pulse. The log of the real part of the solution in Cauchy evolution is shown for $m = 2$ initial data with Gaussian pulse of varying width. As the width is decreased, modes begin to appear at earlier times. This result is surprising for a black hole with such low angular momentum.

# Chapter 9

# Perturbed Kerr-de Sitter Black Holes

A rotating black hole in asymptotically de Sitter spacetime is given by the Kerr-de Sitter metric,

$$ds^2 = \frac{\rho}{\Delta_c} dr^2 + \frac{\rho}{L_c} d\theta^2 + \frac{L_c a^2 \sin^2\theta}{\chi^2 \rho} \left(dt - \frac{\sigma}{a} d\phi\right)^2 - \frac{\Delta_c}{\chi^2 \rho} \left(dt - a \sin^2\theta d\phi\right)^2 \quad (9.1)$$

where

$$\rho = r^2 + a^2 \cos^2\theta \quad (9.2)$$

$$\Delta_c = (r^2 + a^2)\left(1 - \frac{1}{3}\Lambda r^2\right) - 2Mr \quad (9.3)$$

$$\sigma = r^2 + a^2 \quad (9.4)$$

$$L_c = 1 + \frac{1}{3}\Lambda a^2 \cos^2\theta \quad (9.5)$$

$$\chi = 1 + \frac{1}{3}\Lambda a^2 \quad (9.6)$$

By including a positive cosmological constant we introduce an additional horizon, the cosmological horizon, at finite radius. The Kerr-de Sitter spacetime therefore possesses three horizons. Fig. 9.1 shows how the position of these horizons varies with $\Lambda$ for a black hole with $M = 1$ and $a = 0.99$. The results were generated by solving for the roots of $\Delta_c = 0$. The cosmological horizon and event horizons approach each other with increasing $\Lambda$ and meet at a maximum value of $\Lambda$. The two black hole horizons move away from each other with increasing $\Lambda$.

A positive cosmological constant also effects the Cauchy (innermost) horizon in another way. An observer falling into a black hole in asymptotically flat spacetime will be stopped by a singularity at the Cauchy horizon, but this may not be the case in the presence of a cosmological constant. In such a case it has been shown that the

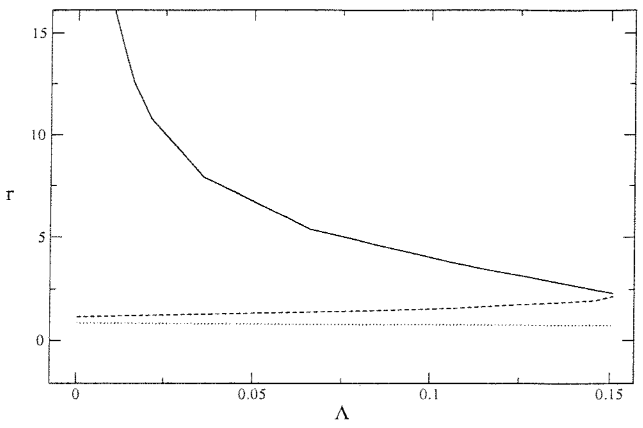

Figure 9.1: Dependence of the position of the three horizons on $\Lambda$. Full line: cosmological horizon, dashed line: event horizon, dotted line: Cauchy horizon. As $\Lambda$ increases, the cosmological and event horizons converge whereas the event and Cauchy horizons diverge.

Cauchy horizon may be stable over a finite range of parameters for non-rotating [102] and rotating [103] black holes. The necessary stability condition is that the surface gravity at the Cauchy horizon is less than the surface gravity at the cosmological horizon. It has been argued that this condition is *"narrowly allowed, even when the cosmological constant is very small, thus permitting an observer to pass through the hole, viewing the naked singularity along the way."* [103]. This is a violation of the strong cosmic censorship hypothesis. A quantum analysis has shown however that the Cauchy horizon, although classically stable, will be quantum mechanically unstable except in the case where the surface gravity at the Cauchy horizon is exactly equal to the surface gravity at the cosmological horizon [104]

A comprehensive review of the literature on this subject up to 1997 has been given by Chambers [105]. The evidence for the existence of a positive cosmological constant has been reviewed in 2000 by Sahni and Starobinsky [108].

The study of the interior of the black hole spacetime requires knowledge of the behaviour of the fields crossing the event horizon due to scattering in the exterior. The late time tails are used in constructing initial data for studies of the interior. Unfortunately an analytic study of the tails in black hole-de Sitter spacetimes is a very difficult task and therefore this problem was first addressed numerically. Brady *et al.* [71] evolved the massless minimally coupled scalar wave equation in both Schwarzschild-de Sitter and Reissner-Nordstrom-de Sitter spacetime. The wave equation is similar in form to the Regge Wheeler equation but with a modified potential. For this they have used both a Cauchy and double-null code. They obtain results for the behaviour of the field at (or near) the cosmological event horizon, the black hole event horizon and surfaces of constant $r$. They also carried out a non-linear analysis which agreed well with the linear results, showing the same late time behaviour of

$$\Psi \sim e^{l\kappa_1 t} \tag{9.7}$$

for $l > 0$, where $\kappa_1$ is the surface gravity at the cosmological horizon. For $l = 0$ the results show a slightly different behaviour

$$\Psi \sim \Psi_0 + \Psi_1 e^{-2\kappa_1 t} \tag{9.8}$$

approaching a constant at late times. Brady *et al* [71] suggest that this unusual late time behaviour for $l = 0$ is connected with a dip in the effective potential for that mode.

In this chapter I extend the numerical investigation of the late time behaviour of scalar field perturbations in the exterior of asymptotically de-Sitter black holes to include rotation. My results span a large range of values for $\Lambda$, from zero to almost extreme. One may argue that such high values of $\Lambda$ are not physically relevant. It is true that observations show our universe today to have a very small cosmological constant, but inflationary cosmology postulates that the early universe underwent a period of exponential expansion driven by the vacuum energy. The vacuum energy density of this period may be interpreted as a large cosmological constant [107]. This may effect the geometry of primordial black holes in the early universe.

Khanal [70] has shown that superradiance can occur in Kerr-de Sitter spacetime. In this chapter I present evidence of this superradiance but my results do not agree with his lower limit of the range of superradiant frequencies.

## 9.1 Perturbations in Kerr-de Sitter spacetime

The scalar wave equation in the Kerr-de Sitter metric is

$$\begin{aligned}-\chi^2(\sigma^2 L_c - \Delta_c a^2 \sin^2\theta)\partial_{tt}\Psi - 2\chi^2 a(\sigma L_c - \Delta_c)\partial_{t\phi}\Psi + \Delta_c^2 L_c \partial_{rr}\Psi + \Delta_c L_c \partial_r \Delta_c \partial_r \Psi \\ + \Delta L_c^2 \partial_{\theta\theta}\Psi - \frac{\cos\theta}{\sin\theta}(2\Lambda a^2 \sin^2\theta - L_c)\partial_\theta \Psi + \chi^2\left(L_c a^2 - \frac{\Delta_c}{\sin^2\theta}\right)\partial_{\phi\phi}\Psi = 0\end{aligned} \tag{9.9}$$

We transform to the new coordinates

$$dr_* = \left(1 + \frac{1}{3}\Lambda a^2\right)\frac{r^2 + a^2}{\Delta_c}dr \tag{9.10}$$

$$d\tilde{\phi} = d\phi + \left(1 + \frac{1}{3}\Lambda a^2\right)\frac{a}{\Delta_c}dr \tag{9.11}$$

where $r_*$ goes from $-\infty$ at the event horizon to $+\infty$ at the cosmological horizon. In terms of these coordinates, and assuming axisymmetry in the form $e^{im\bar{\phi}}$, the wave equation becomes

$$\begin{aligned}-\partial_{tt}\Psi - \frac{2ima\chi^2}{\Sigma R_c^2}(\sigma L_c - \Delta_c)\partial_t\Psi + \frac{L_c\chi^2\sigma^2}{\Sigma R_c^2}\partial_{r_*r_*}\Psi + \frac{2L_c\chi}{\Sigma R_c^2}(\Delta_c r + ima\sigma^2\chi)\partial_{r_*}\Psi \\ + \frac{\Delta L_c}{\Sigma R_c^2}\partial_{\theta\theta}\Psi - \frac{\cos\theta}{\sin\theta}\frac{\Delta_c L_c}{\Sigma R_c^2}(2\Lambda a^2\sin^2\theta - L_c)\partial_\theta\Psi - \frac{m^2\chi^2\Delta_c}{\Sigma R_c^2\sin^2\theta}\Psi = 0\end{aligned} \tag{9.12}$$

where

$$\Sigma R_c^2 = \chi^2(\sigma^2 L_c - \Delta_c a^2\sin^2\theta) \tag{9.13}$$

## 9.2 The Evolution Code

I have taken the old Cauchy code for Kerr spacetime [2], changed the integration for $r$, changed the coefficients of the wave equation, and added the parameter $\Lambda$. The code runs well and reproduces the results of the Kerr code when $\Lambda$ is set to zero.

### 9.2.1 *Setting up the grid*

We work on a grid of $(r_*, \theta)$ but the coefficients of the wave equation are known only in terms of $(r, \theta)$. Eq.(9.10) may be integrated to obtain an equation for $r_*$ given $r$

$$\begin{aligned}r_* &= \int\left(1+\frac{\Lambda a^2}{3}\right)\frac{r^2+a^2}{\Delta_c}dr \\ &= 3\left(1+\frac{\Lambda a^2}{3}\right)\left[\sum_{i=1}^{4}\left(-\frac{1}{2}\frac{(r^2+a^2)\ln(r-r_i)}{2r_i^3+(a^2\Lambda-3)r_i+3M}\right)\right]\end{aligned} \tag{9.14}$$

where $r_i$ are the roots of $\Delta_c = 0$ and $i$ runs from 1 to 4. There is an imaginary part to $r_*$ but we can ignore this as an integration constant.

It is not possible to invert eq. (9.14) to obtain a simple expression for $r$ in terms of $r_*$. Instead we integrate numerically for $r$ using a shooting method. As a starting value we can choose any value of $r$ (as long as it lies between the event horizon and the cosmological horizon) because we are free to choose any value for the integration constant.

### 9.2.2 *Results*

According to Brady *et al* [71] a perturbed scalar field with $l = 0$ in Schwarzschild-de Sitter spacetime will reach a constant value at late times. We expect similar results in Kerr-de Sitter spacetime with $m = l = 0$ initial data as the late time behaviour is generally considered to be connected with the asymptotic structure of the spacetime and is not dependent upon the angular momentum of the black hole. This expectation is confirmed in Fig. 9.2. Figures (a)-(c) show how the log of the real part of the field at one point varies with time. The solution reaches a constant value at late times. This effect can be explained by a dip in the effective potential for $l = 0$. In [109] the authors show that this behaviour is due to a single pole in the Green's function at $i\omega = 0$. The final constant seems to be dependent upon $\Lambda$. Abdalla et al. [106] have shown that the final constant value in Schwarzschild-de Sitter spacetime is also dependent on the initial velocity of the perturbation. Fig. 9.2(d) shows the final constant value obtained as a function of $\Lambda$. This shows a similar behaviour to that observed by Brady *et al* up to $\Lambda \approx 0.00037$. This behaviour is confirmed in [109] by analytic approximation for small $\Lambda$. Our numerical results suggest that this may no longer be valid for larger $\Lambda$, or that a small angular momentum makes a big difference to the late time behaviour. A simpler explanation however is the effect due to the way I have set up the grid by choosing an initial value for the radial coordinate $r$ at a given $r_*$. Fig. 9.3 shows how the final constant value varies for different initial choices for $r$ at a given $r_*$.

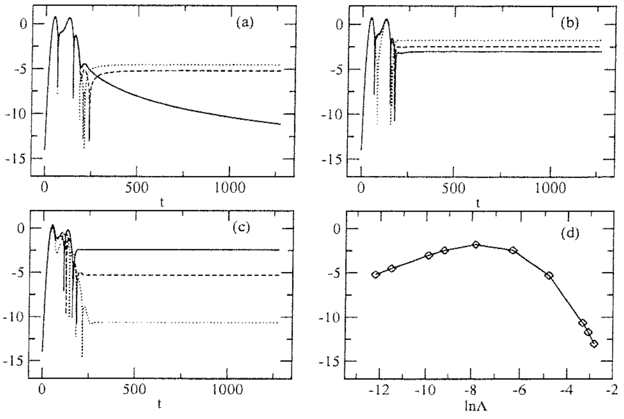

Figure 9.2: Log of the solution at one gridpoint for for $m = l = 0$ initial data and a=0.999 for varying values of $\Lambda$. Similarly to the corresponding problem in Schwarzschild-de Sitter spacetime we see that the solution reaches a constant value at late times.

Figs. 9.4-9.7 show the results for $m = 1$ and $m = 2$ initial data. Here we observe a new effect at large values of the cosmological constant. The late time behaviour for large $\Lambda$ consists of apparently undamped or very slowly damped oscillations. This phenomenon could also be due to some feature, such as a dip, in the potential. The oscillations could be due to radiation becoming trapped within such a dip. My

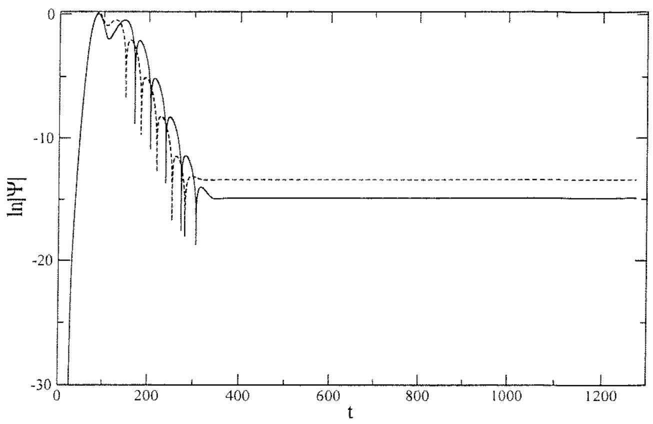

Figure 9.3: Log of output at one gridpoint for a=0.999 for different values for the integration constant in calculating $r$ from $r_*$. A difference is seen in the final constant value reached by the solution. This could help to explain the difference between my results and those of Abdalla *et al* for the dependence of this constant value upon $\Lambda$.

results call for further investigation along these lines, especially to investigate the form of the potential. The amplitude and frequency of the oscillations vary with $\Lambda$.

## 9.3 Superradiance

A well known feature of rotating black holes is *superradiance*, in which incident monochromatic waves with frequency in a specific range are scattered with an increased amplitude, i.e. the reflection coefficient has a magnitude greater than unity. Superradiance has been demonstrated in time-evolution of the scalar wave equation in Kerr spacetime [110] and this method was used to confirm the range of superradiant frequencies:

$$0 < \omega < \frac{ma}{2Mr_+} \tag{9.15}$$

where $r_+$ is the radius of the event horizon.

Khanal [70] has shown that superradiance also occurs in Kerr-de Sitter spacetime. He derives the superradiant frequency range

$$\frac{ma}{r_c^2 + a^2} < \omega < \frac{ma}{r_h^2 + a^2} \tag{9.16}$$

where $r_C$ is the radius of the cosmological horizon and $r_H$ is the radius of the event horizon. Tachizawa and Maeda [72] have numerically calculated the amplification for several values of the cosmological constant for $a = M$ and $l = m = 1$. They show that the maximal amplification increases with increasing $\Lambda$. For Kerr-de Sitter

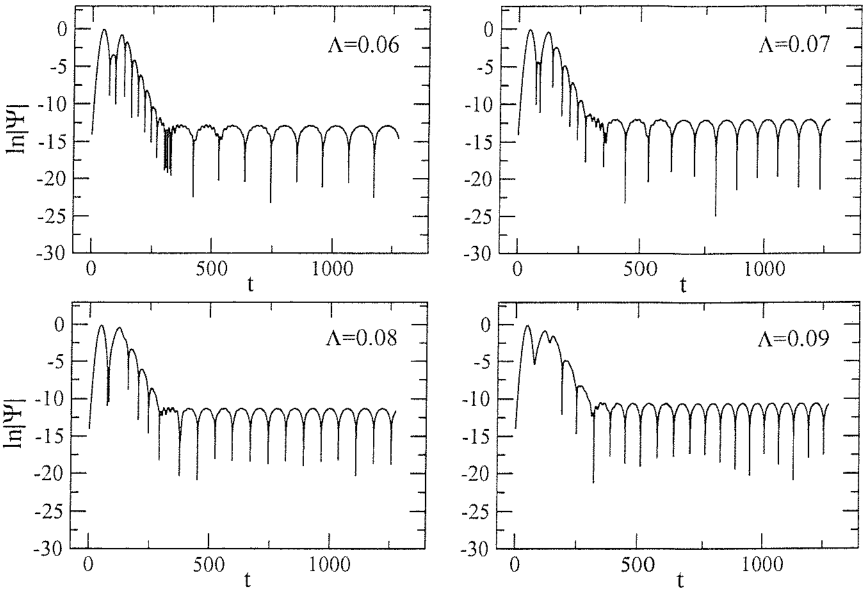

Figure 9.4: Log of the solution at one gridpoint for for $m = l = 1$ initial data and a=0.99 for varying values of $\Lambda$. At late times we see apparently undamped or very slowly damped oscillations. This is a new phenomenon which calls for further investigation. The amplitude and frequency of these oscillations appears to depend upon the value of $\Lambda$.

black holes there is a maximum value for $\Lambda$ for the existence of both the event and cosmological horizons. For the near extreme value of $\Lambda = 0.14$ (with $a = M$ and $l = m = 1$) they obtain a maximal amplification of about double the value for Kerr for scalar field perturbations. While the amplification increases with $\Lambda$, the range of superradiant frequencies decreases however. The combination of these two effects means that we should not expect much more energy from Kerr-de Sitter black holes than from Kerr black holes.

### *9.3.1 Calculating the energy flux*

The direct way to measure superradiance in our time-evolution is to compute the energy flux into and out of the black hole. Following the example in [110] for Kerr spacetime we construct a conserved energy flux for scalar fields in Kerr-de Sitter spacetime.

For a spacetime with a Killing vector $t^a$ and a perturbation with a well defined stress-energy tensor $T_{ab}$, we can define a conserved energy flux vector $T^a_b t^b$. The

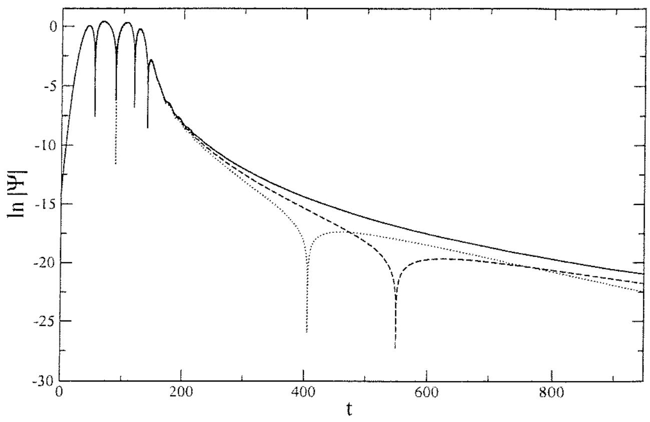

Figure 9.5: Log of the solution at one gridpoint for for $m = l = 2$ initial data and a=0.99 for small values of $\Lambda$. Full line: 0.0, dashed line: 0.00005, dotted line: 0.0001. As $\Lambda$ is increased, the usual tail of Kerr spacetime changes and passes through zero.

flux of energy accross a suface of constant $r$ is then given by

$$dE = T_{ab} t^a r^b dS \tag{9.17}$$

where $dS$ is the three surface element of the hypersurface given by

$$dS = \sqrt{-g^{(3)}}\, d\theta d\phi dt \tag{9.18}$$

and, for a massless scalar field,

$$T_{ab} = \frac{1}{2}\left(\nabla_a \bar{\Psi} \nabla_b \Psi + \nabla_a \Psi \nabla_b \bar{\Psi}\right) - \frac{1}{2} g_{ab} \nabla_c \Psi \nabla^c \bar{\Psi} \tag{9.19}$$

where over-bars denote complex conjugation. Assuming that $r^a r_a = 1$ we find $r^a = \pm(0, \frac{\sqrt{\Delta_c}}{\rho}, 0, 0)$. The time Killing vector is $(1, 0, 0, 0)$. In Kerr-de Sitter spacetime we find $g^{(3)} = \frac{-\sin^2\theta \Delta_c}{\chi^4}$. We therefore obtain the result, integrated over $\Phi$,

$$dE = \pm\pi \left(\partial_r \bar{\Psi} \partial_t \Psi + \partial_r \Psi \partial_t \bar{\Psi}\right) \frac{\sqrt{\Delta_c}}{\rho} \sin\theta \frac{\sqrt{\Delta_c}}{\chi^2} \rho \; d\theta dt \tag{9.20}$$

$$= \pm\pi \left(\partial_r \bar{\Psi} \partial_t \Psi + \partial_r \Psi \partial_t \bar{\Psi}\right) \frac{\Delta_c}{\chi^2} \sin\theta d\theta dt \tag{9.21}$$

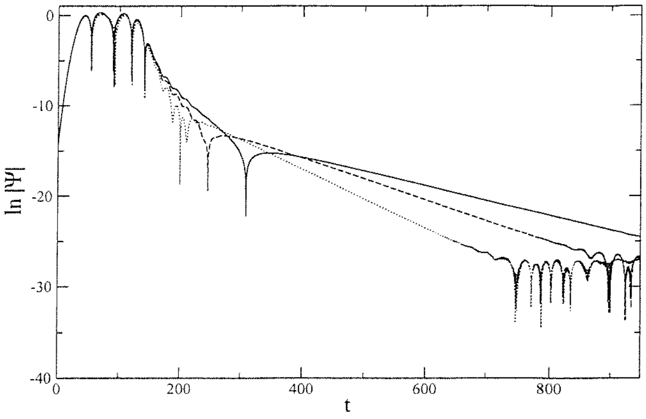

Figure 9.6: Log of the solution at one gridpoint for for $m = l = 2$ initial data and a=0.99 for increasing values of $\Lambda$. Full line: 0.0002, dashed line: 0.0004, dotted line: 0.0008. The irregular oscillations at late time are of very low amplitude compared to the initial data and are probably due to noise. The tail falls off faster with increasing $\Lambda$.

Transforming to the $\tilde{\phi}$ coordinate we find

$$\begin{aligned} dE &= \pm\pi(\partial_r\bar{\Psi}\partial_t\Psi + \partial_r\Psi\partial_t\bar{\Psi} + \chi\frac{a}{\Delta_c}(\partial_{\tilde{\phi}}\bar{\Psi}\partial_t\Psi + \partial_{\tilde{\phi}}\Psi\partial_t\bar{\Psi}))\frac{\Delta_c}{\chi^2}\sin\theta d\theta dt \qquad (9.22)\\ &= \pm\pi(\partial_r\bar{\Psi}\partial_t\Psi + \partial_r\Psi\partial_t\bar{\Psi} + \chi\frac{a}{\Delta_c}(-im\bar{\Psi}\partial_t\Psi + im\Psi\partial_t\bar{\Psi}))\frac{\Delta_c}{\chi^2}\sin\theta d\theta dt \qquad (9.23)\end{aligned}$$

Transforming to the $r_*$ coordinate we find

$$dE = \pm\pi\left(\chi\frac{\sigma}{\Delta_c}\partial_{r_*}\bar{\Psi}\partial_t\Psi + \chi\frac{\sigma}{\Delta_c}\partial_{r_*}\Psi\partial_t\bar{\Psi} + \chi\frac{a}{\Delta_c}(-im\bar{\Psi}\partial_t\Psi + im\Psi\partial_t\bar{\Psi})\right)\frac{\Delta_c}{\chi^2}\sin\theta d\theta dt \qquad (9.24)$$

which can be written in terms of the real and imaginary parts of the solution for use in our numerical evolution.

$$\begin{aligned} dE =& \pm 2\pi\left(\sigma(\partial_{r_*}\Psi_{(re)}\partial_t\Psi_{(re)} + \partial_{r_*}\Psi_{(im)}\partial_t\Psi_{(im)}) - ma(\Psi_{(im)}\partial_t\Psi_{(re)} - \Psi_{(re)}\partial_t\Psi_{(im)})\right)\\ &\times \frac{1}{\chi^2}\sin\theta d\theta dt \qquad (9.25)\end{aligned}$$

### *9.3.2 Setting up Superradiant Initial Data*

In order to trigger superradiance we must set up the initial data in such a way that the frequency of the pulse is within the superradiant range. In order to do this I

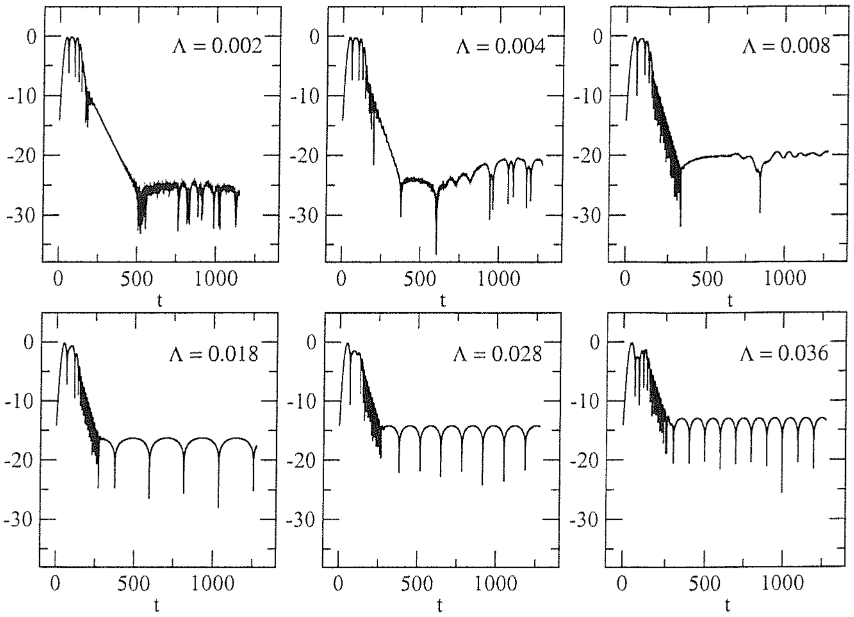

Figure 9.7: Log of the solution at one gridpoint for for $m = l = 2$ initial data and a=0.99 for higher values of $\Lambda$. As $\Lambda$ increases the tail falls off faster and we also see a greater number of quasinormal modes. When the amplitude becomes very low the evolution becomes noisy, but when $\Lambda$ is increased further we can see regular oscillations which are apparently undamped or at least very slowly damped. The amplitude and oscillation of these modes varies with $\Lambda$.

have followed [110] again and use a modulated Gaussian of the form

$$\Psi = e^{-b(r_* - r_0 + t)^2 - i\omega(r_* - r_0 + t)} \tag{9.26}$$

In order to ensure that there is not too much overlap into the non-superradiant range, the width of the pulse is carefully tuned to

$$b = \frac{2\sqrt{\ln(1/\epsilon)}}{\min(m\omega_h - \omega, m\omega_c - \omega)} \tag{9.27}$$

where $\omega_h$ and $\omega_c$ are the angular velocities of the event and cosmological horizons respectively, given by

$$\omega_h = \frac{a}{r_h^2 + a^2} \tag{9.28}$$

$$\omega_c = \frac{a}{r_c^2 + a^2} \tag{9.29}$$

and $\epsilon$ is a small number.

### *9.3.3 Results*

Fig. 9.8 shows the energy flux near the horizon for a Kerr-de Sitter black hole with $a = 1$ and $\Lambda = 0.1$ using $m = 1$ initial data of various frequencies. The suprerrandiant frequency range derived by Khanal is approximately $0.0595 \leq \omega \leq 0.3117$. We see clearly that the flux is outgoing within the superradiant frequency range. Above the upper frequency limit we do not see evidence of superradiance, as expected, but below the lower limit superradiance still occurs in the numerical evolution. Further investigation is required to clarify this problem.

In the case of a zero cosmological constant I found that the ingoing flux at positive $r_*$ balanced quite well with the outgoing flux at negative $r_*$. For higher values of $\Lambda$ however, the ingoing flux at positive $r_*$ did not return to zero and become negative, indicating that the evolution may be losing energy between these two points. The situation seems to improve with resolution but is still a problem.

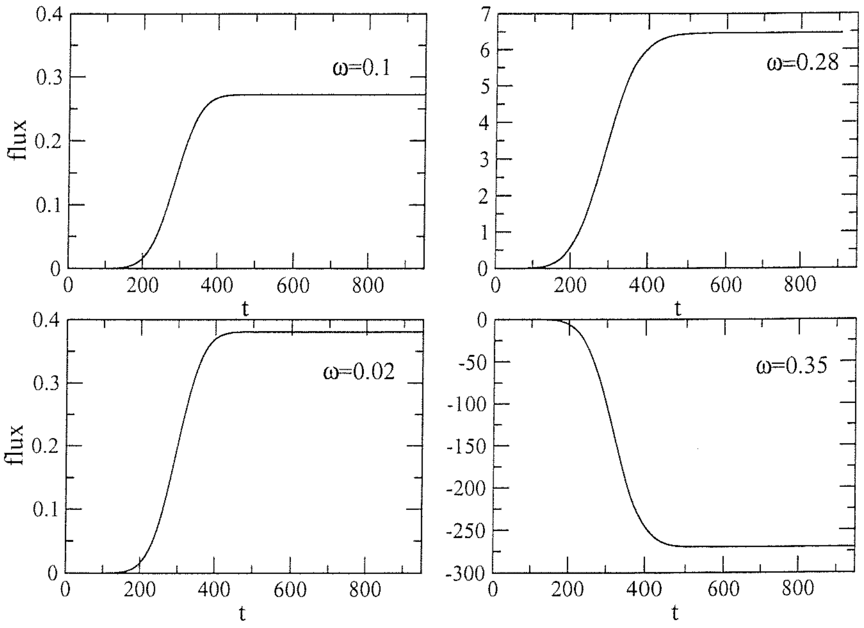

Figure 9.8: Energy flux at $r_* = -30$ for $a = 0.999$ and $\Lambda = 0.1$ for initial data of various frequencies. A negative flux means that the ingoing radiation dominates whereas a positive flux represents superradiance, where the outgoing radiation is greater than the ingoing radiation. The final graph, for $\omega = 0.35$ does not show superradiance because the initial data is outside the superradiant frequency range. Although $\omega = 0.02$ is also outside (below) the predicted frequency range, the results indicate that superradiance is still effective.

## 9.4 Chapter Summary

In this chapter I have adapted the Cauchy code for scalar perturbations in Kerr spacetime to include the effect of a positive cosmological constant. The results confirm those of previous studies [71] for the late time behaviour in Schwarzschild-de Sitter spacetime, but also introduce a new phenomenon for Kerr-de Sitter spacetime. At late times we see regular oscillations of apparently constant amplitude. The amplitude and frequency of these modes varies with A.

I have calculated the energy flux near the horizon using the Kerr-de Sitter code and in this way I have been able to detect superradiance. I have investigated the superradiant frequency range and find that the results agree with the upper limit calculated by Khanal [70] but do not agree with the lower limit.

By developing this code to evolve scalar perturbations in Kerr-de Sitter spacetime, I have been able to make a brief investigation into the behaviour of such perturbations. My results show that this is in an interesting direction for future research.

# Chapter 10

# Toroidal Modes in Differentially Rotating Shells

Oscillating neutron stars are likely to be a good source of gravitational waves for forthcoming detectors. We would like to model such systems in order to interpret the signals we may receive. One factor which is likely to play an important role in a realistic neutron star model is differential rotation. Studies of rotational core collapse indicate that the remnant will be differentially rotating [111],[112]. This differential rotation may be further driven by accretion of supernova remnant material [113] or material from a companion [114]. Studies of r-mode oscillations in neutron stars suggest that non-linear effects can drive a uniformly rotating star into differential rotation [115],[116],[117]. A differentially rotating neutron star may also be generated by binary neutron star merger.

One complication which arises in differentially rotating stars is that the dynamical equations become formally singular at *corotation points* where the pattern speed of a particular mode matches the local angular velocity. This leads to a continuous spectrum and perhaps also corotating solutions. Neutron star oscillations can also be subject to dynamical instability or secular instability to the emission of gravitational waves [118]. These instabilities are of particular interest in the search for gravitational waves. It has been pointed out [119],[120] that differential rotation may introduce new instabilities. Little is currently understood about the effect of differential rotation on stellar oscillations and the related instabilities, and there are many technical challenges involved.

Here we will consider a simple system in differential rotation - a spherical, axisymmetric, thin shell of incompressible ideal fluid. In this way we can understand some of the effects of differential rotation that may be applicable to more complex, three dimensional systems such as neutron stars. In this section I describe work done by Watts, Andersson, Beyer and Schutz [4] and time evolutions I have carried out in collaboration with Watts and Andersson [3]. I present some results from our investigations of three different rotation laws.

## 10.1 The Perturbation Equations

The conservation of mass for an ideal fluid is expressed by the continuity equation

$$\partial_t \rho + \nabla \cdot (\rho \mathbf{v}) = 0 \tag{10.1}$$

The Euler equations (the equations of motion) for an inviscid fluid are

$$\frac{d\mathbf{v}}{dt} = -\frac{1}{\rho}\nabla P - \nabla\Phi \tag{10.2}$$

where $d/dt = \partial_t + \mathbf{v}\cdot\nabla$ is the total time derivative, $P$ is the pressure, $\rho$ the density, $\Phi$ the gravitational potential and $\mathbf{v}$ is the fluid velocity. The gravitational potential is determined by Poisson's equation.

$$\nabla^2\Phi = 4\pi G\rho \tag{10.3}$$

A change in one of the variables at a particular point in space is called an Eulerian perturbation, denoted $\delta$

$$\delta Q \equiv Q(\mathbf{x},t) - Q_0(\mathbf{x},t) \tag{10.4}$$

where $Q$ is some property of the perturbed flow and $Q_0$ is its corresponding equilibrium (background) quantity.

A change in a variable for a particular fluid element moving in the flow is called a Lagrangian perturbation, denoted $\Delta$.

$$\Delta Q \equiv Q(\mathbf{x} + \xi(\mathbf{x},t), t) - Q_0(\mathbf{x},t) \tag{10.5}$$

The two different types of perturbations are related by the equation

$$\Delta = \delta + \xi\cdot\nabla \tag{10.6}$$

where $\xi$ is the displacement of the fluid element.

The perturbed continuity and Euler equations in the inertial frame are

$$\partial_t\delta\rho + (\delta\mathbf{v}\cdot\nabla)\rho + (\mathbf{v}\cdot\nabla)\delta\rho + \delta\rho(\nabla\cdot\mathbf{v}) + \rho(\nabla\cdot\delta\mathbf{v}) = 0 \tag{10.7}$$

and

$$\partial_t \delta \mathbf{v} + (\delta \mathbf{v} \cdot \nabla)\mathbf{v} + (\mathbf{v} \cdot \nabla)\delta \mathbf{v} = \delta \left[ -\frac{1}{\rho} \nabla P - \nabla \Phi \right] \tag{10.8}$$

Working in spherical polar coordinates, with a background velocity of $\mathbf{v} = \Omega r \sin\theta \hat{\mathbf{e}}_\phi$, eqs. (10.7) and (10.8) become

$$\partial_t \delta\rho + \delta v_r \partial_r \rho + \frac{\delta v_\theta}{r} \partial_\theta \rho + \Omega \partial_\phi \delta\rho + \frac{\rho}{r} \left[ r\partial_r \delta v_r + 2\delta v_r + \partial_\theta \delta v_\theta + \cot\theta \delta v_\theta + \frac{1}{\sin\theta} \partial_\phi \delta v_\phi \right] = 0 \tag{10.9}$$

$$(\partial_t + \Omega\ \partial_\phi) \begin{bmatrix} \delta v_r \\ \delta v_\theta \\ \delta v_\phi \end{bmatrix} + \begin{bmatrix} -2\Omega \delta v_\phi \sin\theta \\ -2\Omega \delta v_\phi \cos\theta \\ \delta v_r \sin\theta (r\partial_r \Omega + 2\Omega) + \delta v_\theta (2\Omega \cos\theta + \partial_\theta \Omega \sin\theta) \end{bmatrix} = \tfrac{\delta\rho}{\rho^2} \nabla P - \tfrac{1}{\rho} \nabla \delta P - \nabla \delta\Phi \tag{10.10}$$

If the unperturbed background is axisymmetric then we can make a Fourier decomposition in $\phi$ and look for modes with dependence $e^{im\phi}$. To solve for normal modes we look for time dependence $e^{-i\sigma t}$. In this framework a perturbation will be unstable (growing) if $\mathrm{Im}(\sigma) > 0$. Eqs. (10.9) and (10.10) become

$$i(m\Omega - \sigma)\delta\rho + \delta v_r \partial_r \rho + \frac{\delta v_\theta}{r} \partial_\theta \rho + \frac{\rho}{r} \left[ r\partial_r \delta v_r + 2\delta v_r + \partial_\theta \delta v_\theta + \cot\theta \delta v_\theta + \frac{im\delta v_\phi}{\sin\theta} \right] = 0 \tag{10.11}$$

$$\begin{bmatrix} i(m\Omega - \sigma) & 0 & -2\Omega \sin\theta \\ 0 & i(m\Omega - \sigma) & -2\Omega \cos\theta \\ \sin\theta (r\partial_r \Omega + 2\Omega) & (2\Omega \cos\theta + \partial_\theta \Omega \sin\theta) & i(m\Omega - \sigma) \end{bmatrix} \begin{bmatrix} \delta v_r \\ \delta v_\theta \\ \delta v_\phi \end{bmatrix} = \frac{\delta\rho}{\rho^2} \nabla P - \frac{1}{\rho} \nabla \delta P - \nabla \delta\Phi \tag{10.12}$$

The gravitational potential obeys the perturbed Poisson equation

$$\nabla^2 \delta\Phi = 4\pi G \delta\rho \tag{10.13}$$

Eqs. (10.11), (10.12) and (10.13), together with an equation of state (relating $P$ and $\rho$) and appropriate boundary conditions, describe the perturbations completely. Solving this set of equations in uniform rotation is relatively straightforward. If the rotation is differential, however, problems may arise at points where $\sigma = m\Omega$. At these *corotation points* eq. (10.12) is singular. Note, however, that although this may affect solution of the normal mode problem, the corresponding time dependent equation, eq. (10.10), is not singular so it should not cause a problem for the time evolutions.

Consider a differentially rotating spherical shell of incompressible fluid. The continuity equation in this case is

$$\partial_\theta(\delta v_\theta \sin\theta) + \partial_\phi \delta v_\phi = 0 \tag{10.14}$$

The Euler equations are

$$\partial_t \delta v_\theta + \Omega \partial_\phi \delta v_\theta - 2\Omega \cos\theta \delta v_\phi + \frac{1}{\rho R}\partial_\theta \delta P = 0 \tag{10.15}$$

$$\partial_t \delta v_\phi + \Omega \partial_\phi \delta v_\phi + \Omega^* \delta v_\theta + \frac{1}{\rho R \sin\theta}\partial_\phi \delta P = 0 \tag{10.16}$$

where we have taken the shell radius to be $R$ and we have set $\delta v_r = 0$ and $\delta\rho = 0$

$$\Omega^* = 2\Omega\cos\theta + \partial_\theta \Omega \sin\theta \tag{10.17}$$

is the equilibrium vorticity. Combining the two Euler equations leads to the vorticity equation

$$\begin{aligned}
&\partial_\phi \left[\partial_t \delta v_\theta + \Omega \partial_\phi \delta v_\theta - 2\Omega\cos\theta \delta v_\phi + \frac{c^2}{\rho R}\partial_\theta \delta p\right] \\
&\quad - \partial_\theta \left(\sin\theta \left[\partial_t \delta v_\phi + \Omega \partial_\phi \delta v_\phi + \Omega^* \delta v_\theta + \frac{c^2}{\rho R \sin\theta}\partial_\phi \delta p\right]\right) = 0
\end{aligned} \tag{10.18}$$

and introducing the standard toroidal stream function,$U$, defined by the equations

$$\delta v_\theta = -\frac{1}{R\sin\theta}\partial_\phi U \tag{10.19}$$

$$\delta v_\phi = \frac{1}{R}\partial_\theta U \tag{10.20}$$

$$\tag{10.21}$$

the vorticity equation becomes

$$\partial_t \nabla_{\theta\theta} U + \partial_\phi \nabla_{\theta\theta} U + \frac{\partial_\phi \partial_\theta \Omega^*}{\sin\theta} U = 0 \tag{10.22}$$

where

$$\nabla_{\theta\theta} = \partial_{\theta\theta} + \frac{\cos\theta}{\sin\theta}\partial_\theta + \frac{1}{\sin^2\theta}\partial_{\phi\phi} \tag{10.23}$$

is the Laplacian on the unit sphere. Assuming a $\phi$ dependence of $e^{im\phi}$, eq. (10.22) can be written

$$(i\partial_t - m\Omega)\nabla_{\theta\theta}U + \frac{m\partial_\theta\Omega^*}{\sin\theta}U = 0 \tag{10.24}$$

## 10.2 Modes in Uniform Rotation

In uniform rotation we have

$$\partial_\theta\Omega^* = -2\Omega\sin\theta \tag{10.25}$$

Looking for a mode solution with time dependence $e^{-i\sigma t}$ we substitute into eq. (10.22) to find

$$(\sigma - m\Omega)\nabla_{\theta\theta}U - 2m\Omega U = 0 \tag{10.26}$$

If $\sigma \neq m\Omega$ then

$$\nabla_{\theta\theta}U = \frac{2m\Omega}{\sigma - m\Omega}U \tag{10.27}$$

By expanding $U$ in spherical harmonics and making use of Legendre's equation, we find

$$-\sum_l l(l+1)C_l^m Y_l^m = \frac{2m\Omega}{\sigma - m\Omega}\sum_l C_l^m Y_l^m \tag{10.28}$$

i.e.

$$\sum_l C_l^m \left[\sigma - m\Omega + \frac{2m\Omega}{l(l+1)}\right] Y_l^m = 0 \tag{10.29}$$

Then, considering the orthogonality of the spherical harmonics, the *r-mode* solution is found by noting that only a single $C_l^m$ is non-vanishing and the corresponding frequency is

$$\sigma = m\Omega - \frac{2m\Omega}{l(l+1)} \tag{10.30}$$

Another possible solution is the geostrophic solution, with $\sigma = m\Omega$. From eq. (10.26) we see that this correspond to the trivial solution, $U = 0$, with zero velocity perturbation. Note, however, that in the uniformly rotating case, when $\sigma = m\Omega$ a zero velocity perturbation can be compatible with a non-zero displacement, $\xi$,

$$\delta v_\theta = i(m\Omega - \sigma)\xi_\theta \tag{10.31}$$

$$\delta v_\phi = i(m\Omega - \sigma)\xi_\phi \tag{10.32}$$

Although the geostrophic solution is trivial in uniform rotation, it will play an important role when we consider differential rotation.

## 10.3 Modes in Differential Rotation

The differentially rotating case is described by eq. (10.24). Assuming a time dependence $e^{-i\sigma t}$ and transforming to the new angular variable $x = \cos\theta$, this becomes [4]

$$(\sigma - m\Omega)\nabla_{xx}U - m\partial_x\Omega^* U = 0 \tag{10.33}$$

where

$$\nabla_{xx} = (1 - x^2)\partial_{xx} - 2x\partial_x - \frac{1}{1 - x^2}m^2 \tag{10.34}$$

When $\sigma \neq m\Omega$ for all points on the shell this is a regular eigenvalue problem. But if $\sigma = m\Omega$ at any point on the shell, $x_c$, then eq. (10.33) is formally singular. $x_c$ is called a corotation point (although this terminology is misleading because $x_c$ represents a particular line of latitude on the shell and not only a point). At a corotation point, the pattern speed, $\sigma_p = \sigma/m$ is equal to the local angular velocity, $\Omega(x_c)$.

Solutions to eq. (10.33) may be of three types:

- Discrete real-frequency modes
- Discrete complex frequency modes
- Corotating solutions (solutions with a corotation point)

Watts et al [4] investigate corotating solutions. They show, using the Frobenius method, that a general solution to eq. (10.33) can be written as

$$U = U_{reg} + U_{sing} \tag{10.35}$$

where

$$U_{reg} = (1 - x^2)^{m/2} \sum_{n=0}^{\infty} a_n (x - x_c)^{n+1} \tag{10.36}$$

and

$$U_{sing} = \begin{cases} (1-x^2)^{m/2}\sum_{n=0}^{\infty}\left[a_n(x-x_c)^{n+1}\ln(x-x_c)+c_n(x-x_c)^n\right] & x > x_c \\ (1-x^2)^{m/2}\sum_{n=0}^{\infty}\left[b_n(x_c/x-1)^{n+1}\ln(x_c/x-1)+d_n(x_c/x-1)^n\right] & x < x_c \end{cases} \tag{10.37}$$

In general $U$ is singular at $x = x_c$ but a purely regular solution is possible for rotation laws with $\partial_x\Omega^* = 0$ somewhere on the shell. Another type of regular solution is possible if, for a particular frequency, the zero of $m\Omega - \sigma$ coincides with that of $\partial_x\Omega^*$. In this case the governing equation is non-singular.

Finding a general (singular) solution is complicated by the logarithmic term in eq. (10.37). Watts *et al* deal with this by finding solutions for $x > x_c$ and $x < x_c$ and matching at the corotation point by demanding that $U$ be continuous there. The derivatives of $U$ however are singular at $x = x_c$ and generally have both a logarithmic singularity and a step discontiuity . The size of the step in the derivative varies across the continuous spectrum range and for certain frequencies it can be zero. These *zero-step solutions* are more regular than the other singular solutions. For such solutions the Wronskian of the solutions to the left and right of $x_c$ vanishes at $x_c$.

Solutions that are singular at the corotation point may seem unphysical but the true physical time-dependent solution is obtained by integrating over the entire frequency range for given initial data. This integral solution will not be singular and the continuous spectrum can have physical relevance. In [4] the authors find zero-step solutions at specific frequencies within the corotation region. They also discover a new instability and show that a necessary (although not sufficient) condition for instability is that $\partial_\theta\Omega^* = 0$ at some point on the shell. The dynamically unstable modes that they find all occur when modes cross the corotation boundary (i.e. develop corotation points as the differential rotation is increased) above a certain threshold. One test of these results is to perform a time evolution of initial data and to see if these modes and instabilities appear. In the next section I present evidence that the zero-step solutions can indeed be identified in a numerical time evolution and I confirm the predicted frequency growth time for an instability which arises in a particular case.

## 10.4 Numerical Evolution

We have developed a numerical time evolution code for eq. (10.24). We separate the real and imaginary parts of $U$.

$$U = C\cos(m\phi) - S\sin(m\phi) \tag{10.38}$$

and substitute into the vorticity equation, eq. (10.22). By first substituting $\phi = 0$, i.e. $U = C$, then $\phi = \pi/2m$, i.e. $U = S$, we get two partial differential equations for $S$ and $C$.

$$\partial_t \left( -\partial_{\theta\theta} C - \frac{\cos\theta}{\sin\theta}\partial_\theta C + \frac{m^2}{\sin^2\theta} C \right) + m\Omega \left( \partial_{\theta\theta} S + \frac{\cos\theta}{\sin\theta}\partial_\theta S - \frac{m^2}{\sin^2\theta} S \right) - \partial_\theta \Omega^* m S = 0 \tag{10.39}$$

$$\partial_t \left( \partial_{\theta\theta} S + \frac{\cos\theta}{\sin\theta}\partial_\theta S - \frac{m^2}{\sin^2\theta} S \right) + m\Omega \left( \partial_{\theta\theta} C + \frac{\cos\theta}{\sin\theta}\partial_\theta C - \frac{m^2}{\sin^2\theta} C \right) - \partial_\theta \Omega^* m C = 0 \tag{10.40}$$

These equations contain triple derivatives but, for simplicity, we prefer to work with a first order system of equations in our numerical implementation. Therefore, we introduce the new variables

$$A = \sin\theta \partial_{\theta\theta} C + \cos\theta \partial_\theta C - \frac{m^2}{\sin\theta} C \tag{10.41}$$

$$B = \sin\theta \partial_{\theta\theta} S + \cos\theta \partial_\theta S - \frac{m^2}{\sin\theta} S \tag{10.42}$$

and substitute into the vorticity equation to find

$$-\partial_t A + \Omega m B - (\partial_\theta \Omega^*) m S = 0 \tag{10.43}$$

$$\partial_t B + \Omega m A - (\partial_\theta \Omega^*) m C = 0 \tag{10.44}$$

Then introducing two more new variables

$$Z = \partial_\theta C \tag{10.45}$$

$$X = \partial_\theta S \tag{10.46}$$

eqs. (10.41) and (10.42) become

$$\sin\theta A - \sin^2\theta \partial_\theta Z - \sin\theta\cos\theta Z + m^2 C = 0 \tag{10.47}$$

$$\sin\theta B - \sin^2\theta \partial_\theta X - \sin\theta\cos\theta X + m^2 S = 0 \tag{10.48}$$

$$\tag{10.49}$$

Eqs. (10.43)-(10.48) are 6 first order equations for six unknown variables. The boundary conditions at the poles are (10.47),(10.48)

$$C = 0 \tag{10.50}$$

$$S = 0 \tag{10.51}$$

We use the following second-order finite difference scheme for the six equations

$$\frac{1}{\Delta t}(A_k^{n+1} - A_k^n) - \Omega\frac{m}{2}(B_k^{n+1} + B_k^n) + \partial_\theta\Omega^*\frac{m}{2}(S_k^{n+1} + S_k^n) = 0 \tag{10.52}$$

$$\frac{1}{\Delta t}(B_k^{n+1} - B_k^n) + \Omega\frac{m}{2}(A_k^{n+1} + A_k^n) - \partial_\theta\Omega^*\frac{m}{2}(C_k^{n+1} + C_k^n) = 0 \tag{10.53}$$

$$\frac{1}{2}(Z_k^{n+1} + Z_{k-1}^{n+1}) - \frac{1}{\Delta\theta}(C_k^{n+1} - C_{k-1}^{n+1}) = 0 \tag{10.54}$$

$$\frac{1}{2}(X_k^{n+1} + X_{k-1}^{n+1}) - \frac{1}{\Delta\theta}(S_k^{n+1} - S_{k-1}^{n+1}) = 0 \tag{10.55}$$

$$\frac{\sin^2\theta}{\Delta\theta}(Z_k^{n+1} - Z_{k-1}^{n+1}) - \frac{\sin\theta}{2}(A_k^{n+1} + A_{k-1}^{n+1}) + \frac{\sin\theta\cos\theta}{2}(Z_k^{n+1} + Z_{k-1}^{n+1}) - \frac{m^2}{2}(C_k^{n+1} + C_{k-1}^{n+1}) = 0 \tag{10.56}$$

$$\frac{\sin^2\theta}{\Delta\theta}(X_k^{n+1} - X_{k-1}^{n+1}) - \frac{\sin\theta}{2}(B_k^{n+1} + B_{k-1}^{n+1}) + \frac{\sin\theta\cos\theta}{2}(X_k^{n+1} + X_{k-1}^{n+1}) - \frac{m^2}{2}(S_k^{n+1} + S_{k-1}^{n+1}) = 0 \tag{10.57}$$

If we have $M$ gridpoints then eqs. (10.52)-(10.57) provide $6(M-1)$ equations for the $6M$ unknowns. Boundary conditions provide the remaining 6 equations. We impose four boundary conditions on the inner boundary ($C = 0$, $S = 0$, and eqs. (10.52),(10.53) with $k = 1$) and two conditions on the outer boundary ($C = 0$, $S = 0$).

We solve these equations by the implicit method described in section (4.3). In order to use the relaxation routines, we require the Jacobian for our equations. Call this matrix $S_{e,\beta}$ where $e$ labels the 6 equations and $\beta$ labels the variables. Let $\beta = 1..6$ label the variables $S$, $C$, $A$, $B$, $Z$, $X$ respectively at grid point $k-1$, and let $\beta = 7..12$ label the same variables respectively at grid point $k$. Then we find that $S_{e,\beta}$ is given by

$$\begin{pmatrix} 0 & 0 & 0 & 0 & 0 & 0 & \partial_\theta\Omega^*\frac{m}{2} & 0 & \frac{1}{\Delta t} & -\Omega\frac{m}{2} & 0 & 0 \\ 0 & 0 & 0 & 0 & 0 & 0 & 0 & -\partial_\theta\Omega^*\frac{m}{2} & \Omega\frac{m}{2} & \frac{1}{\Delta t} & 0 & 0 \\ 0 & \frac{1}{\Delta\theta} & 0 & 0 & \frac{1}{2} & 0 & 0 & -\frac{1}{\Delta\theta} & 0 & 0 & \frac{1}{2} & 0 \\ \frac{1}{\Delta\theta} & 0 & 0 & 0 & 0 & \frac{1}{2} & -\frac{1}{\Delta\theta} & 0 & 0 & 0 & 0 & \frac{1}{2} \\ 0 & -\frac{m^2}{2} & -\frac{\sin\theta}{2} & 0 & \epsilon & 0 & 0 & -\frac{m^2}{2} & -\frac{\sin\theta}{2} & 0 & \gamma & 0 \\ -\frac{m^2}{2} & 0 & 0 & -\frac{\sin\theta}{2} & 0 & \epsilon & -\frac{m^2}{2} & 0 & 0 & -\frac{\sin\theta}{2} & 0 & \gamma \end{pmatrix} \tag{10.58}$$

where $\gamma = \frac{\sin^2\theta}{\Delta\theta} + \frac{\sin\theta\cos\theta}{2}$ and $\epsilon = -\frac{\sin^2\theta}{\Delta\theta} + \frac{\sin\theta\cos\theta}{2}$.

## 10.5 Rotation Laws and Results

We consider three different rotation laws and confirm the results derived by Watts using the semi-analytic methods of [4]. By taking a fast Fourier transform (FFT) of the solution at a point on the shell as a function of time we observe specific peaks in the frequency spectrum. Peaks can be seen both outside and inside the corotation region. The peaks outside corotation match the frequencies of the well known modes which become the r-modes in the limit of uniform rotation. The peaks inside corotation match the predicted frequencies for the zero-step solutions. We also observe instabilities where they have been predicted. The results have been verified for $m = 1, 2, 3$, $l = 1, 2, .., 5$ and for varying degrees of differential rotation.

### *10.5.1 Wolff Law*

The Wolff rotation law has its basis in observations of differential rotation in the outer layers of the Sun.

$$\Omega = (454.8 - 60.4\beta\cos^2\theta - 71.4\beta\cos^4\theta) \tag{10.59}$$

$$\frac{d\Omega}{d\theta} = (120.8\beta\cos\theta\sin\theta + 285.6\beta\cos^3\theta\sin\theta) \tag{10.60}$$

$$\frac{d^2\Omega}{d\theta^2} = 0.8\beta(-151 - 769\cos^2\theta + 1428\cos^4\theta) \tag{10.61}$$

$$\frac{d\Omega^*}{d\theta} = 3\cos\theta\frac{d\Omega}{d\theta} - 2\Omega\sin\theta + \sin\theta\frac{d^2\Omega}{d\theta^2} \tag{10.62}$$

The parameter $\beta$, $0 \leq \beta \leq 1$, is a measure of the differential rotation. Uniform rotation corresponds to $\beta = 0$. The angular velocity is greatest at the equator.

Watts et al [4] find zero-step solutions within the continuous spectrum. These are illustrated as dotted lines in Fig. 10.1 for $m = 1$ and $m = 2$. The FFTs of the

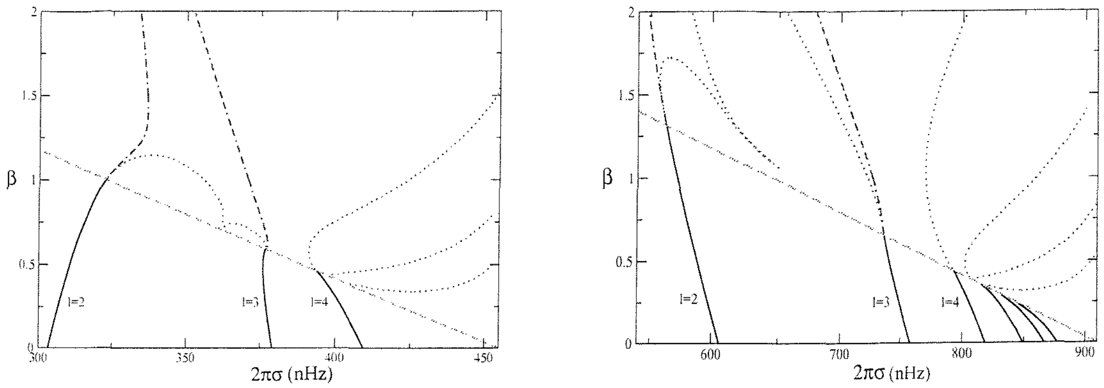

Figure 10.1: Mode results for Wolff rotation law, taken from Watts *et al* [4]. The plot on the left shows $m = 1$, that on the right $m = 2$. Solid lines: real-frequency modes outside corotation. Dashed line: The lower boundary of the corotation region - solutions to the right of this line are corotating. Dash-dot lines: Real part of frequency for dynamically unstable modes. Dotted lines: real-frequency solutions with zero step in the first derivative at the corotation point. The values of $l$ given refer to the uniform rotation limit $\beta = 0$, in which there is one r-mode solution for each value of $l$.

solution at one point, taken from the time evolutions, for initial data of $l = 2..5$ are shown in Fig. 10.2 for $\beta = 0.4$ and Fig. 10.3 for $\beta = 0.5$. The frequencies match those predicted using the methods of [4], including the zero step solutions within the corotation region. Fig. 10.4 shows how the form of the frequency spectrum within the corotation region depends strongly upon the position at which data is sampled on the shell. More understanding of these features is gained by the study of a simple rotation law which is described in section 10.5.3.

Using the necessary condition for instability, $\frac{d\Omega*}{d\theta} = 0$, we look for unstable modes for $\beta \geq 0.4815$. In [4], the authors find instabilities for modes which cross the corotation boundary above this threshold value of $\beta$. These results have been verified by the time evolutions. One particularly interesting result was the behaviour of the $m = l = 3$ mode which has a growth time that increases with $\beta$ up to a maximum and then decreases, i.e. the mode restabilizes for higher values of $\beta$. The results of the time evolutions reproduce the predicted behaviour of the growth time in this case.

### *10.5.2 J-Constant Law*

The j-constant law was chosen because it has been used extensively in the literature (e.g. Hachisu [121]). This law is not physically motivated but was introduced due to its simplicity. It is an example of a law which has greatest angular velocity at the pole.

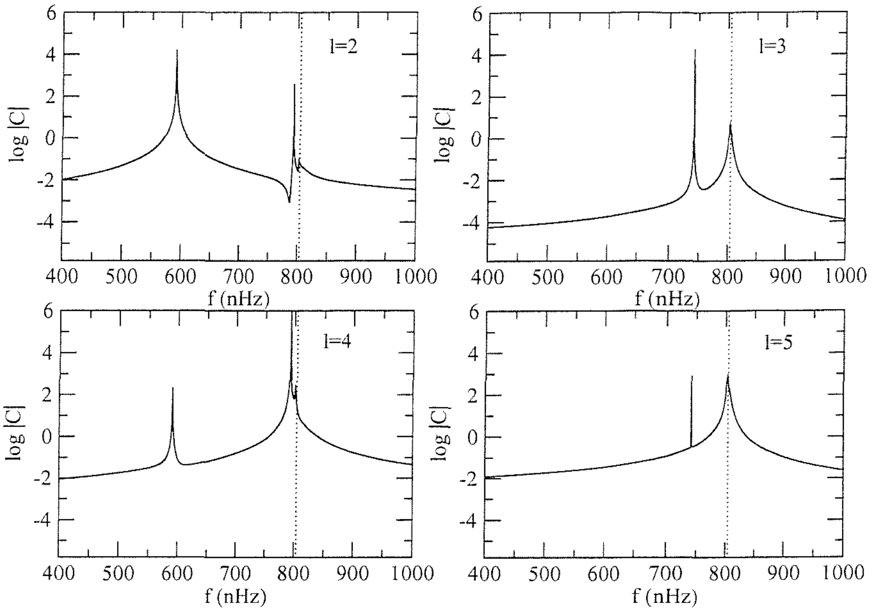

Figure 10.2: Power spectrum for the Wolff rotation law with $m = 2$ and $\beta = 0.4$ with initial data $l = 2 - 5$. The dashed line marks the lower edge of the corotation band, at 804.6. The $l = 2$, 3, and 4 modes are outside the corotation band, at frequencies 592.1, 744.3 and 796.0 respectively. Peaks at these frequencies are clearly visible. For $l = 5$ initial data we see a peak at frequency 806.35 which is just inside the corotation band as predicted by the mode calculations.

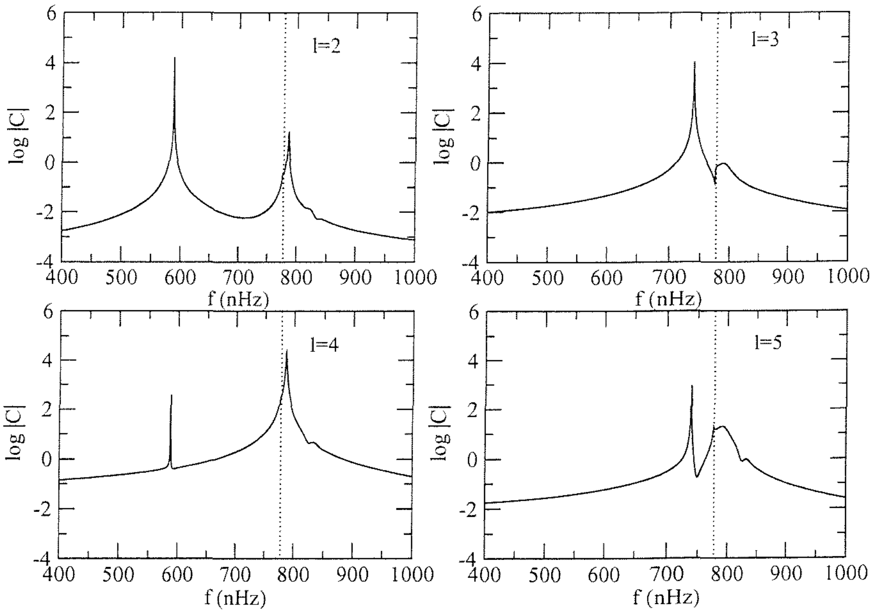

Figure 10.3: Power spectrum for the Wolff rotation law with $m = 2$ and $\beta = 0.5$ with initial data $l = 2 - 5$. The dashed line marks the lower edge of the corotation band, at 777.8. The $l = 2$ and 3 modes are outside the corotation band, at frequencies 588.66 and 741.08 respectively. Peaks at these frequencies are clearly visible. The $l = 4$ mode is now inside the corotation band, at frequency 788.34. This is visible, in addition to a zero-step solution excited by $l = 5$ initial data at 802.50.

$$\alpha = 1 + \frac{\sin^2\theta}{A^2} \tag{10.63}$$

$$\Omega = \frac{\Omega_c}{\alpha} \tag{10.64}$$

$$\frac{d\Omega}{d\theta} = -\frac{2\Omega_c}{A^2\alpha^2}\cos\theta\sin\theta \tag{10.65}$$

$$\frac{d\Omega}{d\theta^2} = \frac{2\Omega_c}{A^2\alpha^2}(\alpha\cos\theta^2\sin\theta^2 - 2\cos^2\theta + 1) \tag{10.66}$$

$$\frac{d\Omega^*}{d\theta} = 3\cos\theta\frac{d\Omega}{d\theta} - 2\Omega\sin\theta + \sin\theta\frac{d\Omega}{d\theta^2} \tag{10.67}$$

Some FFT results are shown in Figs. 10.5 and 10.6 for varying values of $A$ and different kinds of initial data. Fig. 10.7 shows how the solution across the whole grid, $C$, evolves with time. One interesting phenomenon we see here is oscillating sharp peaks appearing near the poles. The results of the time evolutions match the predictions made by Watts, including the zero step solutions within the corotation region. No instabilities were predicted for this rotation law and none were found in our time evolutions.

### *10.5.3 A Simple Law*

We have chosen to study the simple law

$$\Omega = \nu\frac{1}{1+|\cos\theta|} \tag{10.68}$$

$$\frac{d\Omega}{d\theta} = sign(1,\cos\theta)\nu\frac{\sin\theta}{(1+|\cos^2\theta|)} \tag{10.69}$$

$$\frac{d\Omega}{d\theta^2} = sign(1,\cos\theta)\nu\frac{\cos\theta}{(1+|\cos\theta|)^2} + \nu\frac{2\sin^2\theta}{(1+|\cos\theta|)^3} \tag{10.70}$$

$$\frac{d\Omega^*}{d\theta} = 3\cos\theta\frac{d\Omega}{d\theta} - 2\Omega\sin\theta + \sin\theta\frac{d\Omega}{d\theta^2} = 0 \tag{10.71}$$

This law is a useful test because it can be solved analytically as an initial value problem, and the fact that $\frac{d\Omega^*}{d\theta} = 0$ means that the only solution to the normal mode problem is a continuous spectrum. In [3] the solution for initial data $U_0(y) = P_l^m$ in the case $l = m$ (even initial data) is given by

$$\begin{aligned} U(x,t) &= \frac{i(-1)^{m+1}}{4\pi m}\left(\frac{1-x}{1+x}\right)^{\frac{m}{2}}\int_0^x \left[(1+y)^m + (1-y)^m\right]e^{-im\Omega(y)t}dy \\ &+\frac{i(-1)^{m+1}}{4\pi m}\left[\left(\frac{1+x}{1-x}\right)^{\frac{m}{2}} + \left(\frac{1-x}{1+x}\right)^{\frac{m}{2}}\right]\int_x^1 (1-y)^m e^{-im\Omega(y)t}dy \end{aligned} \tag{10.72}$$

The initial value integrals can be solved numerically or analytically for given initial data. The behaviour of the solution $U$ is oscillatory, with the maximum amplitude decaying as $1/t$ at late times for $l = m$ initial data and as $1/t^2$ at late times for $l = m+1$ initial data. Results for $l = m = 1$ and $l = 2, m = 1$ initial data are shown in Fig. 10.8.

The late-time fall off of $U$ can be understood by examining the integrals. Watts has solved the integrals analytically for $m = l = 1$ initial data and finds three different frequencies of oscillation, $\Omega_c$, $\Omega_c/2$ and $\Omega_c/(1+x)$, which interact to produce the beating at early times (seen in Fig. 10.8). The most persistent term has an amplitude that decays as $1/t$, which explains the observed behaviour at late times. The beating is particularly pronounced if $x$ is chosen such that $\Omega_c/(1+x)$ is very close to either of the other two frequencies. Solving the integrals for $l = 2, m = 1$ initial data, Watts obtains the same frequencies as for the $l = m = 1$ case, but the most persistent terms decay as $1/t^2$.

FFT results for particular initial data are shown in Fig. 10.9. For $l = m$ and $l = m + 1$ initial data the analytical solution of the initial value problem shows that we expect contributions from three different frequencies: $\sigma/\Omega_c = m, m/2$ and $m/(1 + |x|)$. Fig. 10.9, for which $x = 0.1$, shows that there are indeed peaks at these three frequencies.

The fact that there are more than one frequency of the solutions in the continuous spectrum in this example and that the frequencies can depend upon the position on the shell could help explain the fact that we see differences in the shape and position of peaks inside the corotation region in the FFT results of the Wolff law for different sampling positions as in Fig. 10.4.

## 10.6 Stability and Convergence

The stability and convergence of our numerical code was tested by Watts and the results are given in her PhD thesis [122]. The numerical scheme shows good stability and second order convergence for the stepsize we have used to obtain the results in this chapter.

## 10.7 Chapter Summary

In this chapter I have developed a numerical code to evolve the equation governing perturbations in a differentially rotating spherically symmetric thin shell. Calculations in the frequency domain were carried out by Watts *et al* [4] [3] and I have confirmed those calculations in the time domain. I have shown that the zero step solutions exist in the time domain at the predicted frequencies within the corotation region, and that there exist instabilities (with the predicted growth times) for certain rotation laws. Using a simple rotation law we have shown that the frequencies of the solutions within the corotation region will in general depend upon the position on the shell at which we sample the data. These new features may carry over into the more difficult problem of differentially rotating Neutron stars.

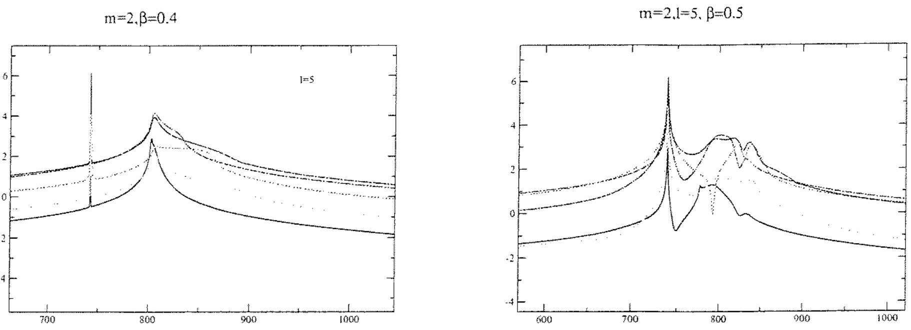

Figure 10.4: Power spectrum for $m = 2$, $l = 5$ initial data with $\beta = 0.4$ (left) and $\beta = 0.5$ (right) for various sampling positions on the shell. We can see that the form of the power spectrum is strongly dependent upon the sampling position. This feature can be understood when we study the simple rotation law of section 10.5.3

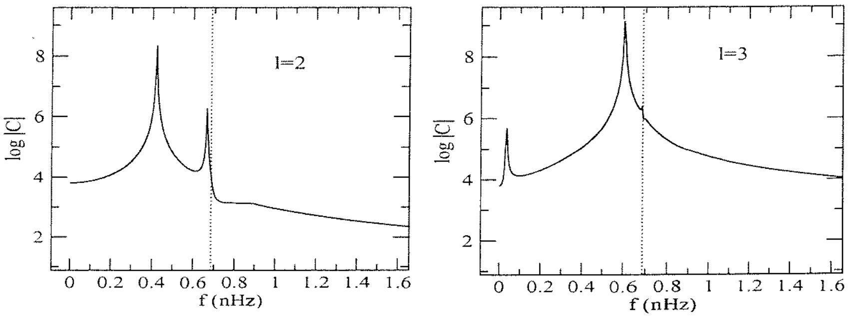

Figure 10.5: Power spectrum results of time evolution for j-constant law for $m = 1$ and $A = 1.5$ with initial data of spherical harmonic form with $l = 2$ (left) and $l = 3$ (right). Modes outside corotation are at frequencies of 0.44 and 0.613 respectively. We can also see a peak appearing at frequency 0.67 which corresponds to $l = 4$ modes. The peak within the corotation region at 0.69 appears as predicted by Watts.

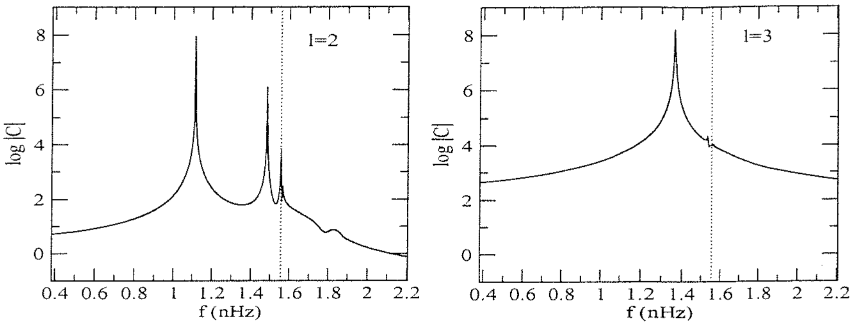

Figure 10.6: Power spectrum results of time evolution for j-constant law for $m = 2$ and $A = 1.9$ with initial data of spherical harmonic form with $l = 2$ (left) and $l = 3$ (right). Modes outside corotation are at frequencies of 1.12 and 1.37 respectively. We can also see a peak appearing at frequency 1.49 which corresponds to $l = 4$ modes. The peak within the corotation region at 1.57 appears as predicted by Watts.

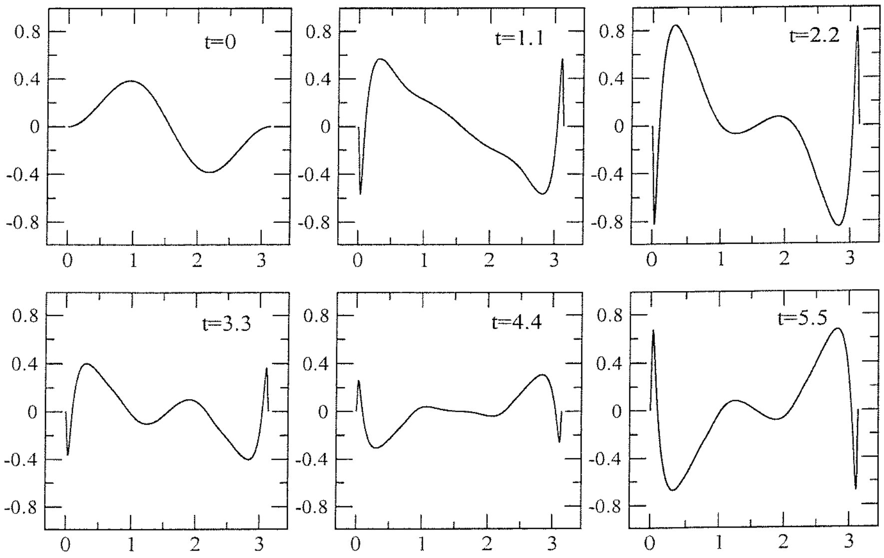

Figure 10.7: Output of $C$ on constant timeslices for j-constant rotation law with $m = 2, l = 3$ initial data and $A = 0.01$. We can see some sharp oscillating peaks appearing near the poles.

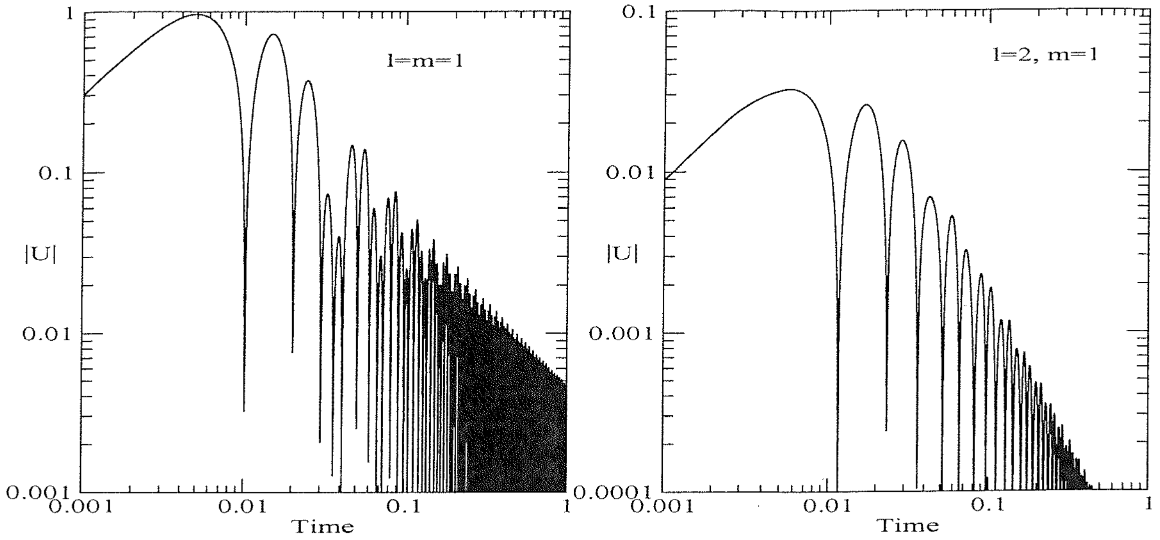

Figure 10.8: Time evolution of $|U|$ for $l = m = 1$ and $l = 2, m = 1$ initial data. At late times, $|U|$ falls off as $1/t$ for the $l = m = 1$ data and as $1/t^2$ for the $l = 2, m = 1$ data.

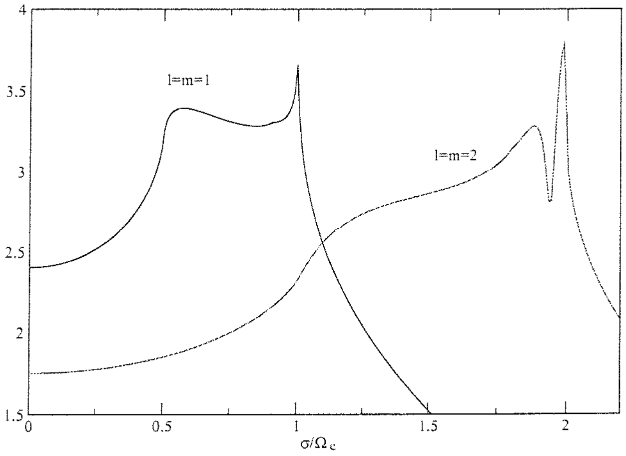

Figure 10.9: Fast Fourier Transform results for the rotation law $\Omega = 1/(1 + |x|)$ for $l = m = 1$ and $l = m = 2$ initial data, sampled at the point $x = 0.1$. For $m = 1$ initial data we expect peaks at scaled frequencies $\sigma/\Omega_c = 0.5$, 0.91 and 1.0. For $m = 2$ initial data we expect peaks at scaled frequencies $\sigma/\Omega_c = 1.0$, 1.82 and 2.0.

# Chapter 11

# Conclusions and Discussion

This thesis represents four years of research work in the study of perturbed compact objects. The main focus has been on developing a characteristic evolution code for the Teukolsky equation governing scalar perturbations in Kerr spacetime, but I have also considered some other interesting problems along the way, such as the effect of a positive cosmological constant on perturbations in Kerr-de Sitter spacetime, and the effect of differential rotation on the oscillation modes of a rotating spherical shell.

In the first four chapters I have introduced the subject of my research and the relevant major developments that have taken place in history. I have also introduced the mathematical and computational techniques which are used in the later chapters of the thesis. In chapters 5,6 and 7 I have considered some examples with known solutions, i.e. the one-dimensional wave equation, the Regge-Wheeler equation and the axisymmetric wave equation, as toy problems. I have evolved these equations numerically as both Cauchy and characteristic initial value problems. This has enabled me to test and further develop the techniques which carry over to the more complicated problems of chapters 8,9 and 10 in which I have presented the main results of my research.

In chapter 8 I have shown how to write the Teukolsky equation for scalar field perturbations in Kerr spacetime as a characteristic initial value problem. This was not immediately obvious as there has been some confusion caused by the use of terms such as 'retarded Kerr coordinate' or 'ingoing Kerr coordinate' in the literature. When we try to write the scalar Teukolsky equation using these null coordinates we do not obtain a characteristic initial value problem. Such coordinates do indeed form a null threading of Kerr spacetime but not a null foliation. This was pointed out by Pretorius and Israel [90] who have introduced *quasi-spherical light-like hypersurfaces* of Kerr geometry for which the retarded and advanced null coordinates are functions of both radial and angular coordiantes , $r_*(r,\theta)$ and $\theta_*(r,\theta)$, to write the retarded characteristic Teukolsky equation and I have gone further by developing a numerical code to evolve this equation. Previously, the Teukolsky equation had only been evolved as a Cauchy problem [2] but there have been some late-time problems with the Cauchy code and, as with all Cauchy grids, it suffers with artificially imposed boundary conditions. By evolving on characteristic hypersurfaces I have been able to compactify the radial coordinate, $r_*$, and avoid boundary problems altogether by evolving all the way out to future null infinity.

I encountered many difficulties while developing the characteristic Teukolsky code. The grid was set up using the coordinates $x(r_*)$ and $\theta_*$ but the coefficients in the equation are written in terms of $r$ and $\theta$. It was not a simple task to calculate the coefficients at a given gridpoint and I found it necessary to calculate the relevant quantities by numerical integration, and some by numerical differentiation. Having set up the grid and being able to calculate the coefficients at all gridpoints I tested this grid by evolving the Teukolsky equation in the time domain with coordinates $(t, r_*, \theta_*)$ and found that the results compared well with those of the old Caucy code.

The characteristic code uses the *criss-cross* finite difference scheme described by Lehner [79], which was successful in evolving the axisymmetric wave equation and which is claimed to be equivalent to the marching algorithm used in characteristic numerical relativity [63]. The angular discretization has been problematic however as it appears to be the cause of numerical instability. This numerical instability can be pushed to very late times by increasing the radial grid resolution and the solution is second order convergent up to the point of instability. The code may therefore still be useful given sufficient computational resources. With further investigation it may be possible to adjust the differencing scheme to obtain a stable numerical evolution, but even if not, the code as it stands may prove to be very useful if it is pushed to later times by increasing the resolution. We have seen that doubling the radial resolution leads to significantly longer evolution times.

The next step in code development would be to match a compactified ingoing evolution reaching the horizon to a compactified outgoing evolution reaching future null infinity as I have done for the Regge-Wheeler equation in chapter 6 with good results. In section 8.4.10 I have written the Teukolsky equation as a double null initial value problem but a stable numerical evolution is still required for this equation. It may be possible to avoid the instability which appears near $r_* = 0$ by evolving a section of the grid around $r_* = 0$ on Cauchy slices and matching the inner boundary to a compactified ingoing characteristic evolution and the outer boundary to a compactified outgoing characteristic evolution. This task should be fairly straightforward following the matching scheme I have used in section 6.4.5, but since there is some doubt about the reliability of the Cauchy code, the same problems may appear in a combined Cauchy-characteristic code.

By evolving the characteristic evolution to later times, this code could be used as a good test of some anomalous results by Krivan [92] for the late-time tail arising from initial data of spherical harmonic form $m = 0, l = 4$. Whereas Hod [97] predicts a fall-off of $t^{-5}$ and Barrack and Ori [96] predict $t^{-3}$, Krivan used the scalar field Cauchy code [2] and found $t^{-5.5}$. Although I have not yet used the characteristic code for this test, I did use the old Cauchy code. I expected to reproduce the results of Krivan but instead I found a late time fall-off close to $t^{-3}$ for both ingoing and outgoing initial data, using both $(r_s, \theta)$ and $(r_*, \theta_*)$ coordinate grids.

In section 8.6 I have presented some results which support the *superradiance resonance cavity* interpretation of Andersson and Glampedakis [51] for explaining the long-lived quasinormal modes of Kerr spacetime. I obtained these results using the original scalar field Cauchy code for the Teukolsky equation. For sufficiently narrow initial data I observed long-lived quasinormal modes appearing even for black holes which were far from extreme. This was an unexpected result as Andersson and Glampedakis had previously only reported this phenomenon for extreme and near-extreme Kerr black holes. By examining the behaviour of the solution near the horizon I observed amplification occurring for oscillations of particular frequency depending on the value of the parameter $a$. These long-lived quasinormal modes appear at earlier times for narrower initial data.

Perturbations in Kerr spacetime have been studied for the past 80 years but my studies have shown that there is yet more work to be done in this field. A stable characteristic evolution is highly desirable and would be of great value in predicting gravitational waveforms for use as templates in the search for gravitational waves. Such a code may be useful in a programme such as LAZARUS [44] to model the ringdown phase following black hole merger using the close-limit [43] approximation. Although the characteristic Kerr code I have described in this thesis is not ultimately stable, it can be pushed to late times by increasing the grid resolution and may therefore prove to be very useful as it stands.

I have shown that there is still some uncertainty about the late-time behaviour of a perturbed scalar field in Kerr spacetime. This uncertainty concerns the decay rate as well as the nature and excitation of the long-lived quasinormal modes. My studies involved investigations of scalar field perturbations but it is expected that the results will carry over to gravitational perturbations which are of more interest in the quest to detect gravitational waves.

In chapter 9 I have extended the original Kerr Cauchy code to include the presence of a positive cosmological constant. The cosmological constant plays an important role in cosmology and particle physics. The effect on black hole spacetimes is to change the asymptotic structure from flat, Minkowski spacetime to de

Sitter spacetime. This introduces an additional horizon, the cosmological horizon. I have shown in chapter 9 that the late-time behaviour of scalar field perturbations in Kerr-de Sitter spacetime can be strongly effected by the presence of a positive cosmological constant. Brady *et al.* [71] previously studied perturbations in Schwarzschild-de Sitter spacetime and found that for $l = 0$ initial data the field reduced to a constant value at late times. I have reproduced this result using my code for Kerr-de Sitter spacetime, and for initial data of higher order, ie. $m = 1, 2$, I have observed a new phenomenon in which the late time field consists of apparently undamped oscillations. The amplitude and frequency of these modes depend upon the value of the cosmological constant. Brady *et al.* argued that the late time constant behaviour for $l = 0$ initial data in Schwarzschild-de Sitter spacetime is due to the presence of a dip in the potential for positive $r_*$. The late time oscillations in Kerr-de Sitter spacetime that I have observed may be due to a similar feature and therefore calls for further investigation of the form of the Kerr-de Sitter (frequency dependent) potential.

I have also observed the effects of superradiance in my numerical evolution of perturbations of Kerr-de Sitter spacetime. The frequency range for superradiance was derived by Khanal and my results seem to agree with his upper frequency limit but I observe superradiance below his lower frequency limit. It may be possible to use the techniques of chapter 8 to evolve the perturbations in Kerr-de Sitter spacetime as a characteristic initial value problem. This would be a good way to test the results I have derived in chapter 9.

In chapter 10 I have moved from the study of black holes to neutron stars and from linearized relativity to the Newtonian limit. Neutron star spacetimes are complicated by the presence of matter, therefore a feasible numerical model will involve many simplifying approximations. Watts *et al.* [4] have considered a spherical, axisymmetric, thin shell of incompressible ideal fluid in differential rotation. In collaboration with them [3] I have developed a numerical code to confirm their predictions for special modes corresponding to *zero-step* solutions which appear within the corotation region of the frequency spectrum. I have also confirmed predictions of new instabilities which occur for some differential rotation laws. Using an implicit numerical evolution I have obtained results for the frequencies of the new modes which compare well with the predictions for three different rotation laws, the j-constant and Wolff laws, and a simple rotation law for which the analytic solution may be calculated and which we have used as a test problem. The frequency peaks within the corotation region in the FFTs were shown to depend on the position on the the shell at which the data was sampled. For the simple rotation law, for which all frequencies are in corotation, Watts was able to predict three frequencies that should show up as peaks in the FFTs, one of which is dependent upon the position of sampling. My results confirm this prediction well. Although we have used a very simplified toy model for our studies of differential rotation, we expect that at least some of the effects we have observed will carry over into more complex, relativistic scenarios such as spinning neutron stars.

# Bibliography

[1] L.P.Grishchuk, V.M.Lipunov, K.A.Postnov, M.E.Prokhorov and B.S.Sathyaprakash, Phys.Usp. **44** 1 (2001) ; Usp.Fiz.Nauk **171** 3 (2001)

[2] W. Krivan, P. Laguna and P. Papadopoulos, Phys. Rev. D **54** 4728 (1996)

[3] A.L.Watts, N. Andersson, and R.L. Williams, M.N.R.A.S **350** 927 (2004)

[4] A.L.Watts, N. Andersson, H. Beyer, B.F.Schutz, M.N.R.A.S. **342** 1156 (2003)

[5] D. Kennefick , preprint gr-qc/9704002

[6] A. Einstein, Press. Akad. Wiss. Berlin, Sitzungsb. 778 (1915); Press. Akad. Wiss. Berlin, Sitzungsb. 799 (1915); Press. Akad. Wiss. Berlin, Sitzungsb. 844 (1915)

[7] K. Schwarzschild, Preuss. Akad. Wiss. Berlin, Sitzungsb., K1.Math. -Phys. -Tech., 189 (1916). Preuss. Akad. Wiss. Berlin Sitzungsb. (Math. Phys. ) 189 (1916)

[8] S. Chandrasekhar, Astrophys. J. **74** 81 (1931)

[9] W. Baade and F. Zwicky, Physical Review **45** 138 (1934)
W. Baade and F. Zwicky, Proc. of the Nat. Acad. of Sci. **20** 254 (1934)

[10] J. R. Oppenheimer and G. Volkoff. Phys. Rev. **55** 374 (1939)

[11] J. R. Oppenheimer and H. Snyder, Phys. Rev. **56** 455 (1939)

[12] S.A. Colgate & R.H. White, Astrophys. J. **143** 626 (1966);
M.M. May and R.H. White, Phys. Rev. D **141** 1232 (1966); Methods Comput. Phys. **7** 219 (1967)

[13] D. Finkelstein Phys. Rev. **112** 965 (1958)

[14] K. Thorne, *Black Holes and Time Warps: Einstein's Outrageous Legacy*, (W.W. Norton & co, reprint, 1995)

[15] T. Regge and J.A. Wheeler, Phys. Rev. **108** 1063 (1957)

[16] C.V. Vishveshwara, Nature **227** 936 (1970)

[17] H. Reissner, Ann. der Physik **50** 106 (1916);
G. Nordstrom, Proc. Kon. Ned. Akad. Wet. **20** 1238 (1918).

[18] J. C. Graves and D. R. Brill, Phys. Rev. **120** 1507 (1960) .

[19] R.P. Kerr, Phys. Rev. Lett. **11** 237 (1963)

[20] B. Carter, Phys. Rev. **174** 1559 (1968)

[21] S.A. Teukolsky, Ap. J. **185** 635 (1972)

[22] J.E. Pringle and M.J. Rees, Astr. Ap. **21** 1 (1972)

[23] R.D. Blandford and R.L. Znajek M.N.R.A.S. **179** 433 (1977)

[24] S. W. Hawking and R. Penrose, Proc. Roy. Soc. Lond. A **314** 529 (1970).

[25] Ya B. Zel'dovich, JETP Letters **14** 180 (1971)

[26] S. W. Hawking, Nature **248** 30 (1974); Commun. Math. Phys. 43 199 (1975)

[27] Ya. B. Zeldovich and I. D. Novikov, Sov. Phys. Dokl. **9** 195 (1964)

[28] R. Giacconi, S. Murray, H. Gursky, E. Kellogg, E. Schreier and H. Tananbaum, Astrophys. J. **178** 281 (1972).

[29] J. Kormendy and L.C. Ho, astro-ph/0003268

[30] Giacconi *et al*, Phys. Rev. Lett. **9** 439 (1962)

[31] J.L. Greenstein and M. Schmidt, Astrophys. J. **140** 1 (1964)

[32] H. Bondi, *Lectures on General Relativity*, eds. S. Deser and K.W. Ford, 1, (Prentice-Hall, New Jersey, 1964);
M. A. Markov, Phys. Lett. **10** 122 (1964)

[33] W. Becker and G.G. Pavlov, in *The Century of Space Science*, eds. J. Bleeker, J. Geiss, and M. Huber, 721, (Kluwer Academic Publishers, 2001)

[34] Hewish et al, Nature **217** 709 (1968)

[35] T. Gold, Nature **218** 731 (1968)

[36] M.I. Large, A.E. Vaughan, and B.Y. Mills, Nature **220** 340 (1968) ;
D.H. Staelin and E.C. Reifenstein, Science **162** 1481 (1968)

[37] R. Giacconi, H. Gursky, E. Kellog, R. Levinson, R. Schreier, and H. Tananbaum, Astrophys. J. **167** 267 (1971)

[38] J.E. Pringle and M.J. Rees, Asron. + Astrophys. **21** 1 (1972);
F.K. Lamb, C.J. Pethick, and D. Pines, Astrophys. J. **184** 271 (1973)

[39] R. Hulse and J. Taylor, Astrophys. J. Letters **195** L51 (1974)

[40] J.H. Taylor, A. Wolszczan, T. Damour, and J.M. Weisberg, Nature **355** 132 (1992)

[41] S. L. Shapiro and S. A. Teukolsky, *Black Holes, White Dwarfs and Neutron Stars*, (John Wiley & sons, 1983)

[42] L. Lehner Class Quant Grav **18** 1225 (2001)

[43] R.H. Price and J. Pullin, Phys. Rev. Lett. **72** 3297 (1994)

[44] J. Baker, M. Campanelli, and C. Lousto, Phys. Rev. D **65** 044001(2002), arXiv: gr-qc/0104063 (2001)

[45] M. Davis, R. Ruffini, W.H. Press, and R.H. Price, Phys. Rev. Lett. **27** 1466 (1971)

[46] C.T. Cunningham, R.H. Price, and V. Moncrief, Ap. J. **224** 643 (1978)

[47] R.H. Price, Phys. Rev. D **5** 2419 (1972)

[48] E.W. Leaver, Phys. Rev. D **34** 384 (1986)

[49] N. Andersson, Phys. Rev. D **51** 353 (1995)

[50] L.M.Burko, G. Khanna, Phys.Rev. D **67** 081502 (2003); E. Poisson, Phys.Rev. D **66** 044008 (2002); M.A. Scheel, A.L. Erickcek, L.M. Burko, L.E. Kidder, H.P. Pfeiffer, and S.A. Teukolsky. preprint gr-qc/0305027

[51] N. Andersson and K. Glampedakis, Phys. Rev. Lett. **84** 4537 (2000)

[52] K. Glampedakis and N. Andersson, Phys Rev D **64** 104021 (2001)

[53] K.D. Kokkotas and B.G. Schmidt, *Quasi-normal modes of stars and black holes*, Living Reviews in Relativity, Volume 2, www.livingreviews.org/Articles/Volume2/1992-2kokkotas. (1999)

[54] http://www.sissa.it/ap/RelAstro/modes.html

[55] T.G. Cowling, M.N.R.A.S. **101** 367 (1941);
J.A. Font, H. Dimmelmeier, A. Gupta & N. Stergioulas, M.N.R.A.S. **325** 1463 (2001).

[56] E. Newman and R. Penrose, J. Math. Phys. **3** 566 (1962)

[57] E.W. Leaver, Phys. Rev. D **34**, 384 (1986)

[58] C.W. Misner, Phys. Rev. Lett. **28** 994 (1972)

[59] W.H. Press and S.A. Teukolsky, Nature **238** 211 (1972); Astrophys. J. **185** 649 (1973)

[60] S.A. Teukolsky and W.H. Press, Astrophys. J. **193** 443 (1974)

[61] N. Andersson, P. Laguna, and P. Papadopoulos, Phys. Rev. D **58** 087503 (1998)

[62] C. Gundlach, R.H. Price, and J. Pullin, Phys. Rev. D **49** 883 (1994)

[63] J. Winicour, *Characteristic Evolution and Matching*, Living Reviews (2001), www.livingreviews.org/lrr-2001-3;
R. Gomez, R.A. Isaacson, J.S. Welling, and J. Winicour, in *Dynamical Spacetimes and Numerical Relativity, Philadelphia, 1985*, ed. J.M. Centrella (Cambridge University Press, Cambridge, 1986), p. 236;
R. Gomez, P. Papadopoulos, and J. Winicour, J. Math. Phys. **35** 4184 (1994);
Gomez et al (Binary Black Hole Grand Challenge), Phys. Rev. Lett **80** 3915 (1998);

[64] C.J.S. Clarke, R.A. d'Inverno, and J.A. Vickers, Phys. Rev. D **52** 6863 (1995);
R.Gomez et al, Phys. Rev. D **54** 4719 (1996);
P. Papadopoulos and P. Laguna, Phys. Rev. D **55** 2038 (1997);
N.T. Bishop et al, Phys. Rev. Lett. **76** 4303 (1996);

[65] M.E. Rupright, A.M. Abrahams and L. Rezzolla, Phys. Rev. D **58**, 044005 (1998)

[66] A. Einstein, Sitz. Ber. Preuss Akad. Wiss. **142** 235 (1931)

[67] E.P. Hubble, Proc. Nat. Acad. Sci. U.S.A. **15** 168 (1929)

[68] S. Perlmutter et al. (Supernova Cosmology Project Collaboration), Astrophys. J. **517** 565 (1999);

B. P. Schmidt *et al* (Hi-Z Supernova Team Collaboration), Astrophys. J. **507** 46 (1998);

A.G. Riess *et al* (Hi-Z Supernova Team Collaboration), Astron. J. **116** 1009 (1998)

[69] U. Khanal, Phys. Rev. D **28** 1291 (1983)

[70] U. Khanal, Phys. Rev. D **32** 879 (1985)

[71] P.R. Brady, C.M. Chambers, W. Krivan, and P. Laguna, Phys. Rev. D **55** 7538 (1997)

[72] T. Tachizawa and K. Maeda, Phys. Lett. A **172** 325 (1993)

[73] N. Stergioulas, *Rotating Stars in Relativity,* (June, 1998), Living Reviews in Relativity, http://www.livingreviews.org/Articles/Volume1/1998-8stergio.

[74] S. Chandrasekhar, Phys. Rev. Lett. **24** 611 (1970);
J.L. Friedman and B.F. Schutz, Astrophys. J. **222** 281 (1978)

[75] N. Andersson, Astrophys. J. **502** 708 (1998).

[76] R. d'Inverno, in *Relativistic Gravitation and Gravitational Radiation*, ed. J.A.Marck and J.P.Lasota, (Cambridge University Press, 1997)

[77] Numerical Recipies.

[78] R. Gomez, J. Winicour and R. Isaacson, J. Comp. Phys. **98** 11 (1992)

[79] L. Lehner, J. Comp. Phys. **149** 59 (1999).

[80] S. Chandrasekhar,*The Mathematical Theory of Black Holes*, (Oxford University Press, 1983)

[81] N. Andersson, Phys. Rev. D **55** 468 (1997)

[82] P.M. Morse and H. Feshbach, *Methods of Theoretical Physics, vol. 2*, (McGrawHill Book Co., New York, 1953)

[83] R.H. Price , Phys. Rev. D **5** 2419 (1972); Phys. Rev. D, 5, 2439 (1972).

[84] L. Lehner, Int. J. Mod. Phys. D **9** 459 (2000)

[85] B.P. Jensen, Ann. de Physique **14** 117 (1989)

[86] G.B. Arfken & H.J. Weber, *Mathematical Methods for Physicists*, (Harcourt Academic Press, 5th Edition, 2000)

[87] K. Thorne, Astrophys. J. **191** 507 (1974)

[88] J. Kristian and R.K. Sachs, Astrophys. J. **143** 379 (1965)

[89] R. Penrose and W. Rindler, *Spinors and Spacetime*, (Cambridge University Press, 1986)

[90] F. Pretorius and W. Israel, Class. Quantum Grav. **15** 2289 (1998)

[91] J. Ockendon, S. Howison, A. Lacey, and A. Movchan, *Applied Partial Differential Equations*, (Oxford University Press, 1999).

[92] W. Krivan, Phys. Rev. D **60** 101501 (1999)

[93] R.A. d'Inverno and J.A. Vickers, Phys. Rev. D **54** 4919

[94] M.R. Dubal, R.A. d'Inverno, and J.A. Vickers Phys. Rev. D **58** 4019 (1998)

[95] C.J.S. Clarke, R.A. d'Inverno, and J.A. Vickers, Phys. Rev. D **52** 6863 (1995); M. Dubal, R.A. d'Inverno, and C. Clarke, Phys. Rev. D **52** 6868 (1995)

[96] L. Barack and A. Ori, Phys. Rev. Lett. **82** 4388 (1999)

[97] S. Hod, Phys. Rev. D **58** 104022 (1998)

[98] E. Poisson Phys.Rev. D66 044008 (2002)

[99] L.B. Burko and G. Khanna, Phys.Rev. D **67** 081502 (2003)

[100] M.A. Scheel *et al*, Phys. Rev. D **69** 104006 (2004)

[101] V. Ferrari and B. Mashoon, Phys. Rev. **30** 295 (1984)

[102] P.R. Brady, D. Nunez, and S. Sinha, Phys. Rev. D **47** 4239 (1993)

[103] C.M. Chambers and I.G. Moss Class. Quant. Grav **11** 1035 (1994)

[104] D. Markovic and E. Poisson, Phys. Rev. Lett. **74** 1280 (1995)

[105] C.M. Chambers, Annals of the Israel Physical Society, vol 13, Proceedings of the workshop held at Tachnion, June 29-July 3, eds. L.M. Burko and A. Ori (1997)

[106] E. Abdalla, C. Molina, and A. Saa, Phys. Rev. D **69** 104013 (2004)

[107] S.M. Carroll, W.H. Press, and E.L. Turner, Ann. Rev. Astron. Astrophys. **30** 499 (1992)

[108] V. Sahni and A. Starobinsky, Int. J. Mod. Phys. D **9** 373 (2000)

[109] P.R. Brady, C.M Chambers, W. Krivan, and P. Laguna, Phys.Rev. D **55** 7538 (1997)

[110] N. Andersson, P. Laguna, and P. Papadopoulos, Phys Rev. D **58** 087503 (1998)

[111] T. Zwerger and E. Müller, Astron. Astrophys. **320** 209 (1997)

[112] H. Dimmelmeier, J.A. Font, and E. Müller, Astron.Astrophys. **388** 917 (2002)

[113] A.L. Watts and N. Andersson, M.N.R.A.S. **333** 943 (2002)

[114] M.Y. Fujimoto, Astrophys. J. **419** 768 (1993)

[115] L. Rezzolla, F.L. Lamb, D. Marković, and S.L. Shapiro, Astrophys. J. **531** L139 (2000)

[116] Y. Levin and G. Ushomirsky, M.N.R.A.S. **322** 515 (2001)

[117] L. Lindblom, J.E. Tohline, and M. Vallisneri, Phys. Rev. Lett. **86** 1152 (2001)

[118] J.L. Friedman, and B.F. Schutz, Astrophys. J. **221** 937 (1978)

[119] E. Balbinski, M.N.R.A.S. **216** 897 (1985)

[120] P.J. Luyten, M.N.R.A.S. **242** 447 (1990)

[121] I. Hachisu, Astrophys. J. S.S., **61** 479 (1986)

[122] A.L. Watts, PhD thesis, University of Southampton (2003)